RARE CELL SEPARATION USING RESETTABLE CELL TRAPS

by

William Beattie

B.Sc.E., Queen's University, 2010

A THESIS SUBMITTED IN PARTIAL FULFILLMENT OF
THE REQUIREMENTS FOR THE DEGREE OF

MASTER OF APPLIED SCIENCE
in
THE FACULTY OF GRADUATE STUDIES
(Mechanical Engineering)

THE UNIVERSITY OF BRITISH COLUMBIA
(Vancouver)

August 2013

Abstract

Techniques for the separation of cells from heterogeneous samples that do not rely on biological labels are important in applications where specific labels are unknown or unavailable. However, limitations of existing label-free separation techniques have prevented their widespread adoption. Those techniques that separate based on cell size typically offer high throughput but lack specificity. Those that separate based on a combination of cell size and deformability have superior selectivity, but are slow and prone to clogging.

This work reports a microfluidic device that employs novel resettable cell traps to separate cells based on size and deformability. The resettable cell trap is a microchannel with controllable cross-section, featuring recesses to temporarily store captured cells. Larger and less deformable cells flowing through a cell trap with constricted cross-section will be selectively captured due to size restriction, and can be released back into the flow for collection by enlarging the channel cross-section. Smaller and more deformable cells will simply pass through the constricted channel. The ability to enlarge the trap and purge it of captured cells enables long term operation without clogging. The cell separation device presented is able to separate UM-UC13 cancer cells from human leukocytes with high enrichment (~100x), retention (~90%) and throughput (450,000 cells/hour). Serial separation using this mechanism provides extremely high enrichment (~2500x) without sacrificing retention. The mechanism is also shown to resolve size differences of 1 μm between polystyrene microspheres. The resettable cell trap is an improvement upon existing technology, providing greater enrichment than possible through size-based techniques while improving throughput and eliminating problems caused by clogging that are typical of filtration based techniques.

Preface

This dissertation is the original, independent work of the author, with the exception of the materials described below.

The mechanism described in Chapter 2.2 was originally developed by research group member Thomas Gerhardt. The method for data acquisition described in Chapter 3.4 was developed in collaboration with research group members Sarah McFaul and Bill Lin. Measurements of cell size and deformability in Chapter 4.5 were performed by research group members Lin Wang and Quan Guo. Some of the microfluidic devices used for the cell separation experiments described in Chapter 6 were fabricated by research group member Xi Qin. Measurements of cell viability described in Chapter 6.6 were performed by Xi Qin.

A paper based on the device described in Chapter 2 and the results presented in Chapters 6 and 7 has been submitted for publication, entitled:

> "High throughput label-free cell separation using resettable cell traps," W. Beattie, X. Qin, L. Wang, and H. Ma. Submitted to *Lab on a Chip*, 2013.

Table of Contents

List of Tables

List of Figures

List of Symbols, Abbreviations or Other

BSA	Bovine serum albumin
CD	Cluster of differentiation
CTC	Circulating tumor cells
CTP	Critical trapping pressure
DLD	Deterministic lateral displacement
EMT	Epithelial-mesenchymal transition
EpCAM	Epithelial cell adhesion molecule
FACS	Fluorescence activated cell sorting
PBS	Phosphate buffered saline
PDMS	Polydimethylsiloxane

Glossary

Background cell	The cell type to be depleted from a heterogeneous sample. For the experiments described in this document, background cells include leukocytes and erythrocytes.
Constricted trap	A conformation of the resettable cell trap in which the elastomeric diaphragm is raised into contact with the flow channel's center fin. This decreases the channels height sufficiently to trap incident target cells, while background cells flow through.
Critical trapping pressure	The trapping pressure required to capture 95% of incident target cells on a given microfluidic device.
Enrichment	The ratio of the relative concentration of target cells in a sample before and after separation.
Relaxed trap	A conformation of the resettable cell trap mechanism in which the elastomeric diaphragm is lowered into the control channel. The flow channel height in a relaxed trap is sufficient to allow the free flow of both target and background cells.
Retention	The percentage of incident target cells captured by a separation mechanism.
Sieve valve critical pressure	The pressure required to inflate a sieve valve into contact with the ceiling of the channel above it.
Target cell	The cell type to be extracted or enriched from a heterogeneous sample. Target cells in separation experiments were UM-UC-13 bladder cancer cells or mouse lymphoma cells
Trapping curve	The functional relationship between the trapping pressure applied to the resettable cell trap and the fraction of cells captured.
Trapping pressure	The net pressure across the elastomeric diaphragm in the resettable cell trap. A positive trapping pressure pushes the diaphragm up into the flow channel. A negative trapping pressure pushes the diaphragm down into the control channel.

Acknowledgements

This project would not have been possible without the support of my friends and coworkers. In particular, I owe a debt of gratitude

To Dr. Hong Ma, for his patience and support in guiding me through the research process, for teaching me how to think like a scientist and an engineer, and for opening doors both within and beyond the lab.

To Dr. Karen Cheung and Dr. Linfen Yu, for establishing and managing the BioMEMS laboratory, and for their willingness to share space and expertise.

To Sarah, Bill, GQ, Xi, and the rest of the members of the Multiscale Design Lab, for their camaraderie and their invaluable support in the lab.

To Greg and Peter, for working through the grad school process alongside me.

To my parents and sisters, whose inexhaustible patience and love saw me through this pursuit.

Thank you.

Chapter 1 - Introduction

1.1 Motivation

The separation of cells based on their physical properties is important in many biological and biomedical applications where specific biochemical markers are unavailable. For example, circulating tumor cells (CTCs) are thought to be distinguishable from peripheral blood cells based on physical characteristics [**1**] [**2**], and the biochemical cell surface markers currently used to isolate CTCs are thought to be unreliable or of low yield [**3**] [**4**]. Furthermore, these cells have been observed to arrest in the microvasculature because of their larger size and limited deformability [**5**], which suggests that separation based on physical properties may be an appropriate method for capturing these cells.

Existing techniques for cell separation vary widely, but they all begin from the same premise: given a sample that contains one or more phenotypes to be extracted (**target cells**) and one or more phenotypes to be discarded (**background cells**), devise a way to separate the target cells from background cells based off of one or more discriminating characteristics. In this thesis, we detail the design and performance of a cell separation technique that uses physical filtration to discriminate phenotypes based off of their size and deformability. Our cell separation device employs microfluidic technology to provide consistency and control in the filtration process, allowing the separation of rare cells with high yield and enrichment.

In this chapter we will introduce the field of microfluidics, discuss the applications of cell separation and their functional requirements, and compare conventional cell separation techniques against various microfluidic approaches.

1.2 Fundamentals of microfluidics

Microfluidics refers to the field of study of fluids systems with sub-millimeter length scales, and to the field of engineering that employs these small-scale fluidic systems. Microfabricated fluidic channels have been used in science and engineering research for over 40 years [**6**], with the most significant early application being the development of the ink jet nozzle for printing systems [**7**]. Early development in microfluidics was slow, in part due to the high cost of materials and manufacturing processes required to produce microfluidic

devices. The explosion of interest in microfluidics starting in the late 1990s was triggered by the development of two enabling technologies: soft lithography, and microfluidic valves.

Soft lithography is a fabrication technique used to produce replica microfluidic devices from a single master mold [**8**]. Shown in Figure 1-1, this process involves casting a liquid material over a solid master, curing the liquid, then peeling off the resulting negative replica. Critically, soft lithography can be used to produce many copies of a design without requiring the expensive equipment and materials required for photolithography more than once. The most commonly used material for soft lithography is polydimethylsiloxane (PDMS), a liquid polymer that becomes an elastomeric solid when cured in a mixture with a cross-linking agent. PDMS has become the material of choice for most microfluidic applications because of its low cost, optical transparency, permeability to gasses, and elasticity [**9**].

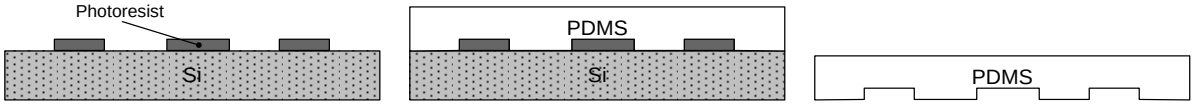

Figure 1-1 Soft lithography. A master wafer is first fabricated using photolithography so that it can be used to make many negatives though soft lithography. A liquid polymer is poured onto the master, cured, and then peeled off.

Shortly after the popularization of soft lithography, Unger et al. devised a simple and cost effective way to fabricate on-chip microvalves for precisely controlling fluid flow [**10**]. The structure of these mechanisms is comprised of two vertically stacked channels separated by a thin PDMS diaphragm. By applying pressure difference across the two channels, the diaphragm is deflected into contact with the ceiling of the lower pressure channel (Figure 1-2), either forming a complete seal if the flow channel ceiling is round (regular valve) or a partial seal if the channel ceiling is rectangular (sieve valve). Regular valves are used to arrest the flow of both fluid and suspended particles, while sieve valves are used to allow fluid but not solids to pass through, so that suspended particles accumulate upstream.

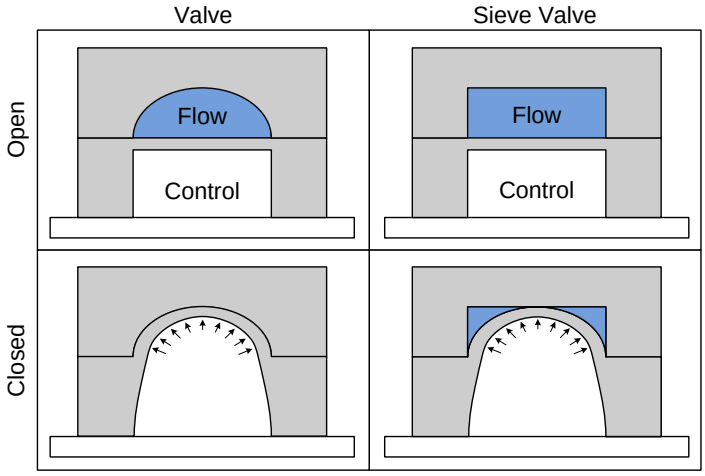

Figure 1-2 Schematic of microfluidic valves. Regular valves feature a rounded flow channel that allows the diaphragm to form a complete seal when the control channel is pressurized. Sieve valves feature rectangular flow channels so small gaps in the top channel remain open in the when the control channel is pressurized.

The development of microfluidic valves gave tremendous flexibility to the design of microfluidic devices. Fluidic routing could now be achieved without the need for expensive and large displacement off-chip solenoid valves. This development essentially decoupled the cost and complexity of microfluidic devices, allowing for the economic fabrication of very high density devices (Figure 1-3) [**11**].

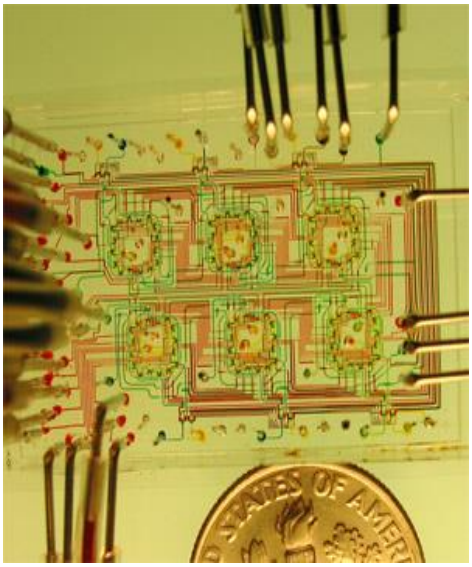

Figure 1-3 A complex microfluidic device. Valves, pumps, and mixers are all featured in this device used to study the growth of microbial populations. Image taken from [12**].**

Microfluidic devices have a number of advantages over their macroscopic brethren; some are obvious and others are more subtle. The simple fact that microfluidic devices are small

means material costs are low, devices occupy little valuable lab space, and reagent consumption is low. Furthermore, the 1-100 micron length scale typical of microfluidic devices is particularly conducive to biological applications. Features can be patterned at the single cell size, and the scaling of certain physical laws allows access to physical phenomena atypical of the macroscopic domain. The unusual physics accessible by microfluidic devices originate from the low Reynolds number environment to which microfluidics almost always belong, in which viscous effects dominate fluid inertia. The reader unfamiliar with microfluidics is encouraged to refer to Appendix A for a more complete discussion of microfluidics and low Reynolds number flows.

1.3 Cell separation

1.3.1 Circulating tumor cells

Circulating tumor cells (CTCs) are the vehicles of blood-borne cancer metastasis. Metastasis occurs when cells escape from a primary tumor into the circulatory system, flow to another part of the body, arrest in a new organ and extravasate to form micrometastases which then grow into macroscopic tumors (Figure 1-4). The prognostic consequences of metastasis are dire – more than 90% of all cancer related deaths are caused by metastases [**5**]. The concentration of circulating tumor cells in peripheral blood is thought to be an indicator of the rate of metastasis, and has been correlated to shorter median progression-free survival and shorter overall survival in breast cancer [**13**], castration-resistant prostate cancer [**14**], lung, colon, and pancreatic cancers [**15**].

The key challenge in identifying and separating CTCs from whole blood is their extreme rarity. The presence of as few as 5 CTCs in 7.5 mL of whole blood (six orders of magnitude rarer than leukocytes, nine orders of magnitude rarer than erythrocytes) has been established as a prognostic marker in breast, prostate, lung, and ovarian cancer [**13**]. The rarity of CTCs is a major impediment to further understanding the metastatic process. Producing a viable sample of CTCs for study would be an important step in individualizing patient treatment, evaluating potential drugs, and to understanding the underlying mechanisms of metastasis.

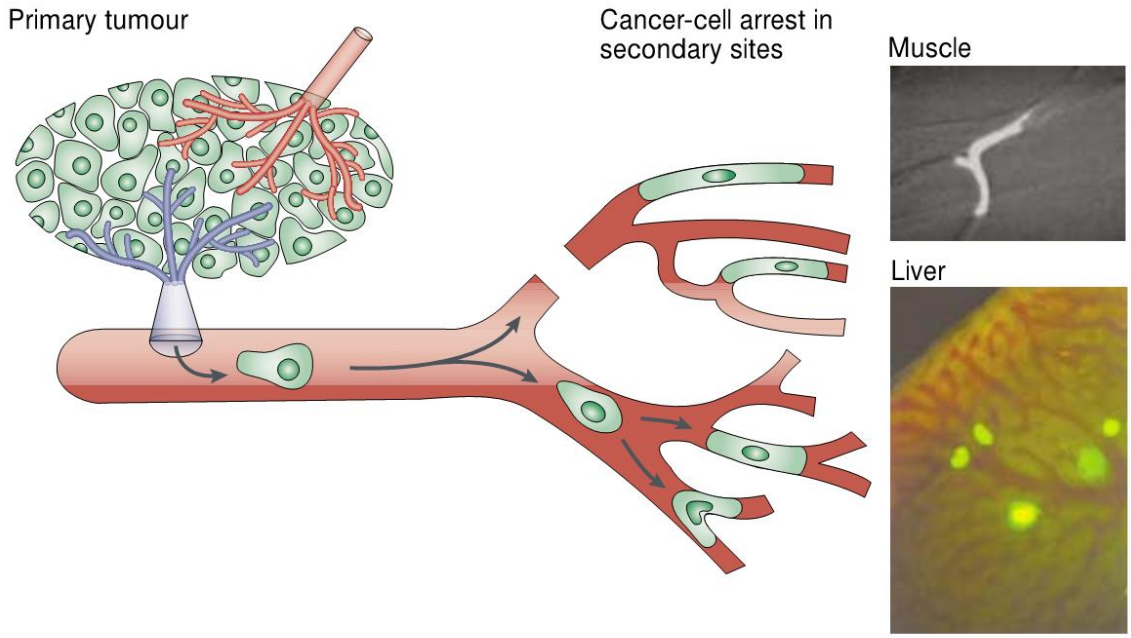

Figure 1-4 The metastatic process. Cancer cells from a primary tumor escape into the circulatory system and become circulating tumor cells. These cells may arrest in secondary sites, often in the microvasculature due to size restriction. Arrested cells may then extravasate, proliferate and form secondary tumors. Examples of cells arrested in capillaries of muscle and liver are shown on the right. Image taken from [5].

Despite more than a decade of research and development, there exists no satisfactory solution for isolating and enumerating circulating tumor cells in blood. A recent review [**16**] states: '[a]lthough the potential applications of CTC analyses appear extraordinarily promising, the development of appropriate, high throughput, and reliable technological platforms for rare tumor cell detection within blood specimens remains the critical impediment.'

Proposed methods for separating CTCs from hematological cells include biochemical and biophysical approaches. Physical differences between CTCs and blood cells are suggested by the observation of CTCs arresting in the microvasculature, indicating that CTCs are larger, or more rigid than the blood cells around them. Biological differences exploited in cell separation devices concern the cell surface molecules, often referred to as labels, of leukocytes, erythrocytes, and CTCs. Specifically, CTCs are thought to express proteins characteristic of epithelial cells such as cytokeratin and epithelial cell adhesion molecule (EpCAM), while blood cells do not [**17**]. Additionally, CTCs are not thought to express CD45, a cell surface molecule expressed by leukocytes. Size, deformability, and the

presence or absence of specific biological labels may all be used to discriminate CTCs from blood cells.

1.3.2 Other separation applications

Cell separation tools are currently being developed for a variety of applications beyond the capture of CTCs. In [**18**], fetal epithelial cells are separated from the peripheral blood of pregnant women based on their size. These fetal cells can be used in early genetic analyses, providing information valuable for obstetrical care. In [**19**], recent improvements in the separation and handling of blood for standard medical analyses are detailed, specifically with respect to miniaturization. In [**20**] [**21**], mesenchymal stem cells are separated from bone marrow, umbilical cord blood, or adipose tissue, a promising development in supporting cellular therapy. While these other applications are valuable, the intended application of the cell separation device developed in this thesis is CTC separation, and the design of the device reflects that goal.

1.3.3 Performance metrics for cell separation processes

In order to compare the efficacy of various cell separation techniques, a common set of metrics are used. The quality of a separation is measured by two metrics: target cell retention and enrichment ratio.

- **Retention:** The percentage of target cells sorted that enter the collection outlet

$$Retention = \frac{Target\ cells\ collected}{Target\ cells\ sorted}$$

- **Enrichment Ratio:** The change in the relative concentration of target cells from before separation to after separation.

$$Enrichment\ Ratio = \frac{\frac{Target\ cells\ collected}{Background\ cells\ collected}}{\frac{Target\ cells\ sorted}{Background\ cells\ sorted}}$$

Cell separation devices are often further characterized by two secondary metrics: throughput and resolution. These secondary metrics are useful in determining the range of applications for which a separation mechanism offers a practical solution.

- **Throughput:** The total number of cells processed per unit time
- **Resolution:** The difference in some physical property of the cell (typically diameter) between target and background cells required such that the device can distinguish and effectively eliminate more than 90% of background cells [**22**]**.**

Target cell retention and enrichment ratio are the most important metrics, describing how specific the separation mechanism is. Throughput determines how long it will take to process a sample of a given size. Resolution determines the smallest difference between the characteristics of target and background cells that permits an effective separation.

The field of cell separation does not yet have consistent standards for comparing and testing devices. The target and background cell types used in experiment vary between publications. Devices designed for the separation of CTCs from whole blood have used a variety of model cancer cells including neuroblastoma cells [**23**]; HeLa cervical carcinoma cells [**24**]; LNCaP prostate carcinoma cells [**25**]; MCF7 breast carcinoma cells [**24**]; mouse lymphoma cells [**26**]; and the UC13 bladder cancer cells used in this document. These phenotypes have different intrinsic size and deformability distributions. As such, directly comparing the retention and enrichment ratio reported in competing publications may be of limited meaning [**22**].

1.4 Conventional cell separation techniques

1.4.1 Differential centrifugation

Particles in suspension settle under buoyant forces. The speed at which the particles sink or float is a function of their diameter and density relative to the medium. Heterogeneous mixtures can be separated based on size and density by simply leaving them to settle undisturbed, but the process is typically too slow for most applications. To expedite the process, the sample can be loaded into a centrifuge that produces centripetal accelerations several hundred times greater than gravity.

If the densities of both the target cells and background cells exceed that of the fluid, differential centrifugation is a time sensitive process – all cells will eventually form a pellet at the bottom of the container, but the rate at which they settle may differ. To produce a stable separation, the sample can be layered on top of an inert liquid with a density between

that of the target and background cells. After a sufficiently long centrifugation, the denser cells will form a pellet at the bottom of the container and the less dense cells will form a cloud on top of the inert liquid. Centrifugation has been used as an initial step for rare cell enrichment [**27**], but even optimized methods offer low enrichment and require additional processing to isolate target cells.

1.4.2 Flow cytometry

Flow cytometry describes a family of laser-based analytical techniques capable of measuring and separation cells with extraordinary throughput. In a typical flow cytometry setup, cells flow in a thin stream, one at a time, through a laser beam where one or many properties of the cell are measured. At this observation point, sensors can measure size, granularity, birefringence, and other physical properties of the cell based on the way they scatter the laser light [**28**]. Flow cytometers are typically used to measure the properties of a population of cells, but more sophisticated cytometers can be made to sort cells. In a process called droplet sorting, cells flow past the observation point and the fluid stream is broken into droplets by a vibrating nozzle, with each droplet containing a single cell. The electric charge of the nozzle is actively controlled to impart a net charge on droplets containing target cells. Beyond the nozzle, the stream of droplets flows past a charged plate. The charged droplets containing target cells are deflected in the electric field created by the plate, while the uncharged droplets containing background cells flow straight downward. Such setups are capable of processing up to 100,000 cells each second. A schematic of a droplet sorting apparatus is shown in Figure 1-5 below.

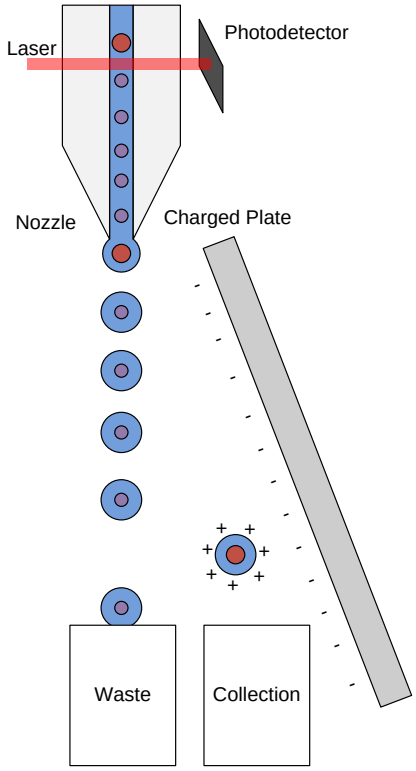

Figure 1-5 Schematic of a droplet sorting apparatus. A stream of cells flows through a narrow channel past an observation point. Cells flow through a nozzle that splits the stream into droplets with controllable electric charge. The cells fall downward, and charged cells are passively sorted through attraction to a charged plate.

The set of properties measureable through flow cytometry can be greatly broadened through the use of fluorescent labels, a process known as fluorescence activated cell sorting (FACS). Fluorescent stains have been developed for a wide array of biological properties of interest, and employing a photodetector sensitive to this fluorescence allows the cytometer to detect them. Using labels, droplet sorters can be made to sort cells based on protein content, gene expression, surface antigens, membrane integrity, and a variety of other parameters [**28**].

Flow cytometry is an exceptionally high throughput and flexible process, but lacks the sensitivity to be an appropriate technique for the isolation of rare cells. The sensitivity limit of cytometry for separating human cancer cells from whole blood via flow cytometry has been investigated: an optimized multi-parametric cytometry separation of MDA-MB-468 cancer cells from whole mouse blood had a reported sensitivity floor of 0.01% [**29**]. Background events began to overwhelm identified cancer cells below a ratio of one cancer cell per 10,000 mouse leukocytes. In contrast, the concentration of CTCs in whole blood is

estimated to be one CTC per 10^5-10^7 leukocytes [**16**]. For this reason, researchers have turned towards more sensitive techniques to separate rare cell populations.

1.4.3 Immunomagnetic cell separation

Immunomagnetic cell separation involves selectively binding a labeling particle to target cells in the mixture, similar to FACS. However, the label in immunomagnetic cell separation is not conjugated to a fluorescent molecule but instead to a ferromagnetic microparticle. Once the magnetic particles have bound to the target cells, the analyte is placed in a magnetic field, separating the labeled cells from the unlabeled (Figure 1-6).

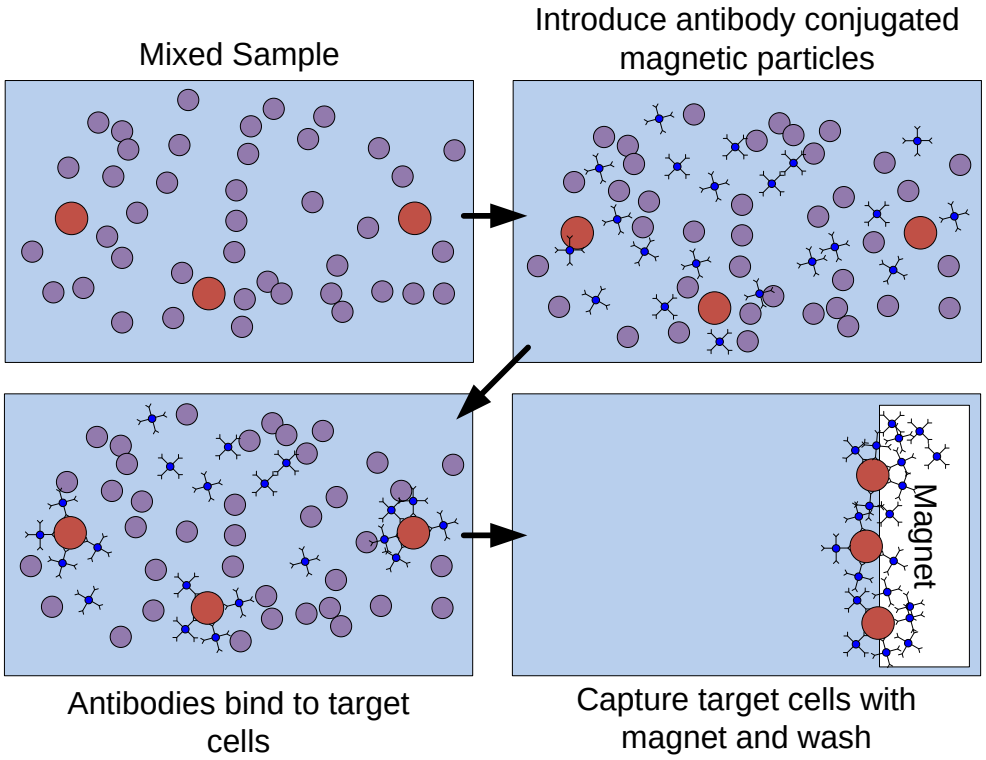

Figure 1-6 Immunomagnetic cell separation. Ferromagnetic nanoparticles are conjugated with antibodies that selectively bind to target cells. The tagged cells are then captured using a magnetic field. Additional steps to remove unbound nanoparticles and to isolate the captured cells are optional.

Immunomagnetic cell separation is one of the most successful approaches to the separation of rare cells developed in the recent literature [**30**,**31**]. Currently, the only FDA approved tool to isolate CTCs (Veridex CellSearch®) is an immunomagnetic cell separation device. The CellSearch® device uses magnetic nanoparticles functionalized with an anti-body for the epithelial cell adhesion molecule (anti-EpCAM). The device works on the premise that

unlike normal blood cells, CTCs will express EpCAM, and indeed at least some do – the device produces up to 1000 EpCAM positive cells per mL of blood, and the concentration of these cells correlates strongly with patient survival in breast [**13**], colorectal [**32**], and prostate cancers [**33**].

Like all label-based separation techniques, this approach relies on knowledge of the biological properties of target and background cells in order to select an appropriate antibody. In the case of the CellSearch® system, it is uncertain if all CTCs express EpCAM, as cells shed by a primary tumor may lose EpCAM expression as they undergo the epithelial to mesenchymal transition (EMT) necessary for them to enter circulation. From a recent review on the topic [**4**]:

> 'EpCAM downregulation has been associated with EMT, and in mice with colon carcinoma, small metastases were EpCAM negative but large metastases in the same mouse displayed an equal level of expression as the primary, possibly reflecting the re-expression at the metastatic site. In line with these findings, one log reduction in EpCAM expression on circulating tumor cells was found compared with various primary tumors and their metastases.'

Western blots performed on a bulk CTC sample shows decreased EpCAM expression [**3**], but the variability in expression levels between individual cells cannot be assessed without single cell proteomics. In conclusion, while EpCAM based immunomagnetic cell separation is currently the most powerful CTC detection tool available, it is possible that this technique fails to capture a subpopulation of CTCs that do not express EpCAM in sufficient levels. To remedy this shortcoming, techniques that differentiate based on other labels or on intrinsic biomarkers such as size and deformability should be used.

1.5 Microfluidic cell separation techniques

Recently, a new class of cell separation techniques has been developed, aiming to improve on conventional techniques using the advantages of microfluidic technology [**34**]. Microfluidic devices have several attractive properties, including small sample consumption, high speed processing, low cost, and potentially increased sensitivity and resolution.

1.5.1 Microfluidic affinity capture

Affinity capture is a microfluidic cell separation approach that isolates target cells by binding them to a surface or particle functionalized with specific label molecules, typically proteins or antibodies. The analyte flows through the microfluidic device and cells that are not bound within the device simply flow through to a waste outlet. This approach is similar to immunomagnetic cell separation as described in 1.4.3, but flexible design and high surface area to volume ratio typical of microfluidics greatly enhances the probability that a target cell comes into contact with the functionalized surface [**35**,**36**]. Figure 1-7 below shows an array of functionalized microposts, arranged to optimize cell contact, used to separate model CTCs doped into whole blood [**15**].

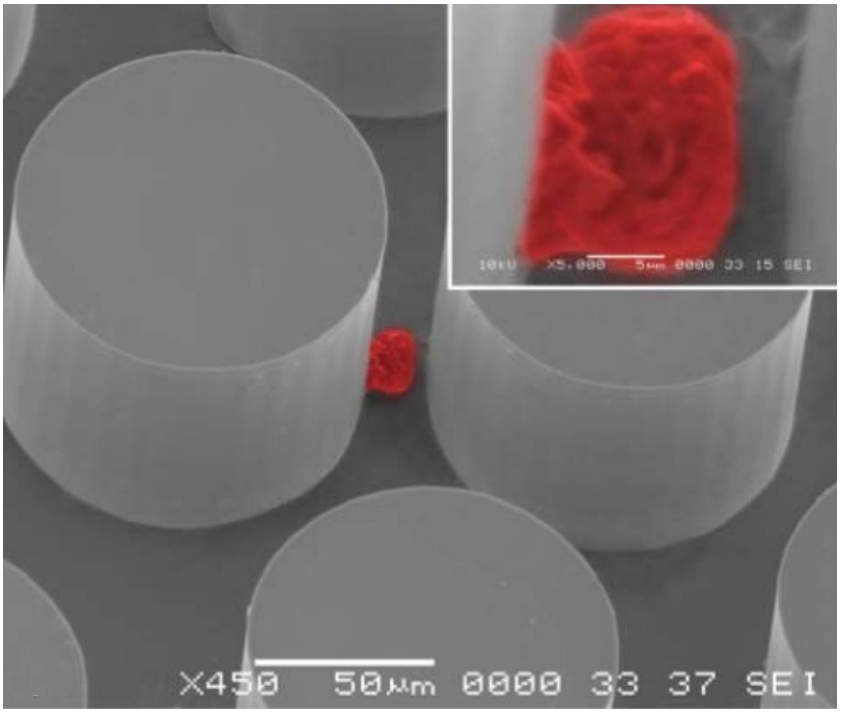

Figure 1-7 A cell captured in a functionalized micropost array. This scanning electron microscope image shows a NCI-H1650 lunch cancer cell that had been spiked into whole blood, then bound to a micropost coated with anti-EpCAM. Image taken from [15**].**

The limitations of microfluidic cell separation devices that use biochemical labels are the same as their macroscopic kin – they require intimate knowledge of the properties of target and background cells. For positive selection, the user must select a label that is expressed by all target cells and no background cells. For negative selection, the opposite is true.

However, given an appropriate label, affinity capture can be a high throughput, highly selective separation technique.

1.5.2 Label-free cell separation techniques

The last decade has seen substantial development in cell separation techniques that do not rely on biochemical labels [**22**]. Label-free techniques use intrinsic biomarkers such as size and deformability to discriminate between cells, and may be useful in applications where decreased cost is advantageous or where specific labels are unknown. We will not attempt an exhaustive review of the relevant publications, but instead highlight the operating principles of the most popular separation mechanisms and discuss their general merits and limitations. A quantitative comparison between the cell separation capabilities of these devices and our own is featured in Section 7.3.

1.5.2.1 Pinched-flow fractionation

Pinched-flow fractionation refers to a family of cell separation techniques that exploit the finite size effects of flowing suspensions to discriminate between cells based on size. Particles flowing at low Stokes number tend to follow the streamline that passes through the particle's center, unless the particle is brought into contact with a solid structure. When contact between a suspended particle and solid structure occurs, the particle will bump over to an adjacent streamline, typically moving one particle radius away from the structure to provide sufficient clearance from the structure. As a result, when particles flow into contact with a solid, the streamline that they are bumped into depends on their size. This size dependent spacing can be amplified if the channel is designed so that streamlines diverge downstream of the contact point.

In one implementation [**37**], an inlet flow carrying the cell suspension is pinched against the channel wall by a buffer fluid (Figure 1-8). The centers of the cells are separated from the wall by one cell radius, producing a small lateral separation of large and small cells. The channel then suddenly expands, amplifying the spatial distribution of streamlines that were closely packed in the pinch-region. Large cells that occupied one streamline in the pinch region enter an exit channel closer to the channel centerline, while small cells that were pinched closer to the wall follow a different streamline to a different outlet.

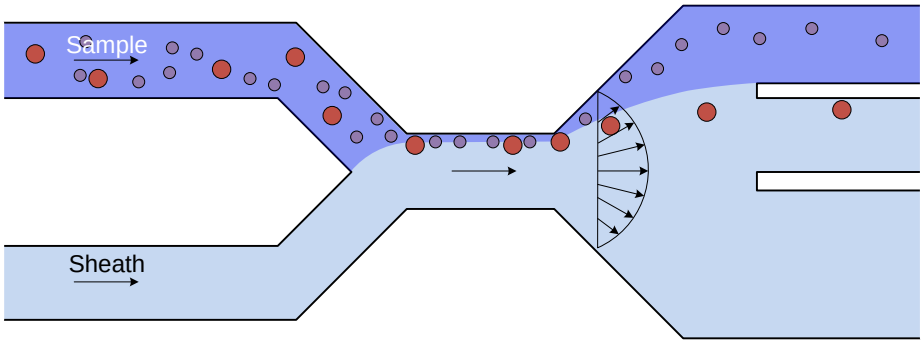

Figure 1-8 Pinched flow fractionation. The incident cell sample is pushed against a channel wall by a sheath flow. Large cells are displaced farther from their original streamlines than small cells. A rapid expansion in the channel causes streamlines to diverge, amplifying the lateral separation and forcing the cell types into separate outlets.

1.5.2.2 Deterministic lateral displacement

Deterministic lateral displacement (DLD) is a size-based separation technique with the same operating principle as pinched flow fractionation, mentioned specifically here for its popularity in the literature. DLD involves flowing a cell sample through a staggered micropost array [**38**] (Figure 1-9). Sufficiently small cells will flow straight through the array in the direction of the carrying fluid, but cells beyond a threshold size will bump into the microposts and shift streamlines, producing a net motion perpendicular to the direction of the flow. This produces a lateral separation between large and small cells.

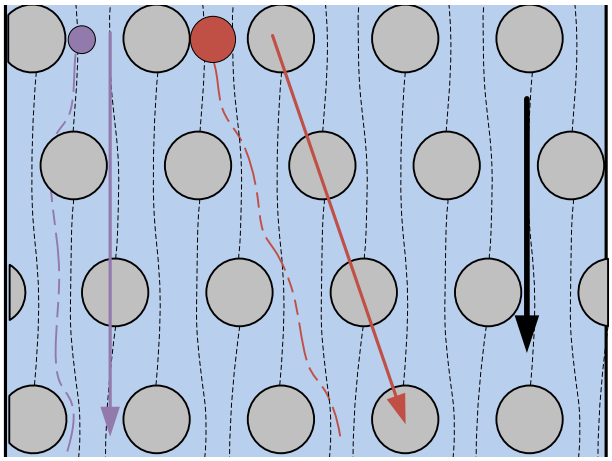

Figure 1-9 Deterministic lateral displacement. Cells are flowed through a staggered micropost array, with streamlines shown as dotted lines. Small cells are able to weave in between posts, following the direction of the fluid. Large cells bump into posts and are forced laterally across streamlines.

The array discriminates between cells above and below a critical size, determined solely by the gap size between posts and the stagger between post rows [**39**]. The precision of the critical size is limited only by the precision of photolithographic fabrication, allowing high resolution separations. DLD arrays have separated microparticles with 10 nm resolution [**40**], the finest resolution of any label-free separation technique by a considerable margin. A single DLD array can be designed to resolve a wider range of particle sizes by varying the spacing between pillars as a function of the distance down the pillar array. Such an array would produce a spatial distribution at the outlet, ranging from the smallest cells which were never bumped, to intermediate cells that were bumped in the sections of the array with sufficiently small pillar spacing, to the largest cells that were bumped from the beginning of the array to the end.

DLD arrays have been used to separate the constituent phenotypes of whole blood [**38**], nucleated red cells from peripheral blood [**41**], and model cancer cells from blood [**42**], but the broader applicability of the technique is limited by its purely size based discrimination.

1.5.2.3 Dean flow in spiral microchannels

A promising class of cell separation devices discriminates between cells based on their interactions not with solid structures, but with the flowing fluid itself. This class of mechanism takes its name from the branch of fluid mechanics that studies the behavior of low but non-negligible Reynolds number flows (Re>1): inertial microfluidics [**43**].

Suspended particles experience different forces in inertial flows than Stokes flows, and some of these effects can be exploited for the purposes of cell separation.

The first example of cell separation using inertial microfluidics involves secondary Dean flows in spiral microchannels [**44**] [**45**] [**46**]. In these devices, cells flow through a spiral channel at Re>1, and migrate to a lateral position in the channel that depends on their size (Figure 1-10). This lateral migration is driven by two competing inertial forces: the inertial lift force and the Dean drag force. The inertial lift force is driven by the shear gradient created within the channel [**47**], and the Dean drag force is driven by secondary currents perpendicular to the direction of flow caused by centrifugal forces in the spiral microchannel [**48**]. Inertial lift forces push cells towards the channel walls, and Dean drag forces draw cells towards the channel center with a force that is dependent on cell size. Provided the spiral channel is sufficiently long to allow particles to migrate to their equilibrium position, they will be spatially separated based on diameter when they arrive at the outlet.

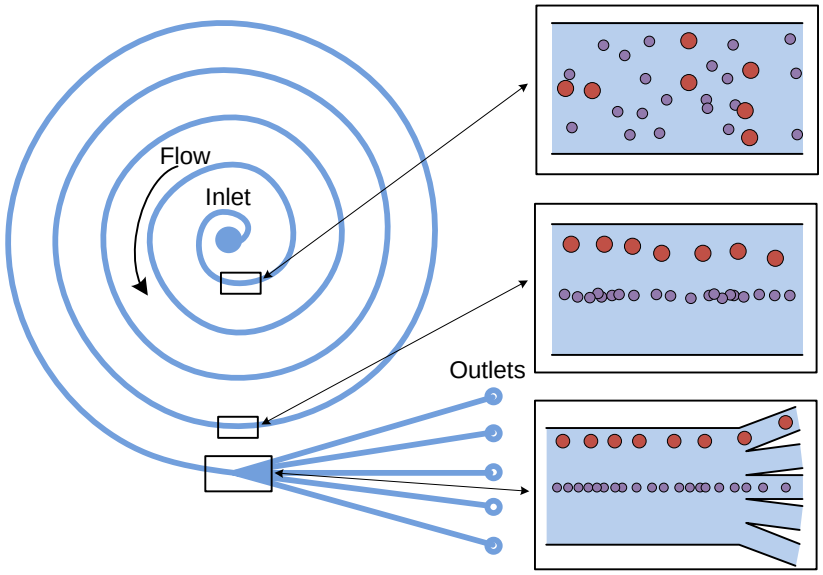

Figure 1-10 Cell separation using spiral microchannels. Cells injected at the sample inlet will migrate to their size-dependent equilibrium position under a combination of inertial lift forces and Dean drag forces. A split channel towards the outlet delivers the separate streams to different reservoirs.

This technique offers tremendous throughput (~1 million cells/min [**44**]), but the mechanism is entirely sized-based, and the only cells that have been separated using this technique so far are neuroblastoma and glioma cells with relatively poor enrichment.

1.5.2.4 Microvortex cell capture

Another inertial cell separation technique involves the selective capture of large cells in microvorticies [**24**] [**49**] [**50**]. In this approach, the cell suspension is flowed at Re>1 through a long thin channel with sudden expansions and contractions (Figure 1-11). In the long and thin section, cells are aligned near the channel walls by inertial lift forces driven by the shear gradient within the fluid field [**51**]. At the channel expansion, the inertia of the primary flow causes it to detach from the channel wall, producing a microvortex in the expansion. Cells continue to experience the inertial lift force at the expansion, and drift laterally towards the expansion at a speed proportional to the square of the cell diameter. Since large cells drift faster than small cells, the length of the expansion can be designed such that cells beyond a critical size laterally drift into the microvortex while smaller cells stay inside the main stream. Cells that enter microvorticies are trapped, and will circulate indefinitely. Trapped cells can be released and collected by lowering the flow rate through the device – this will lower the Reynolds number of the flow and eliminate the flow separation that produced the vortices.

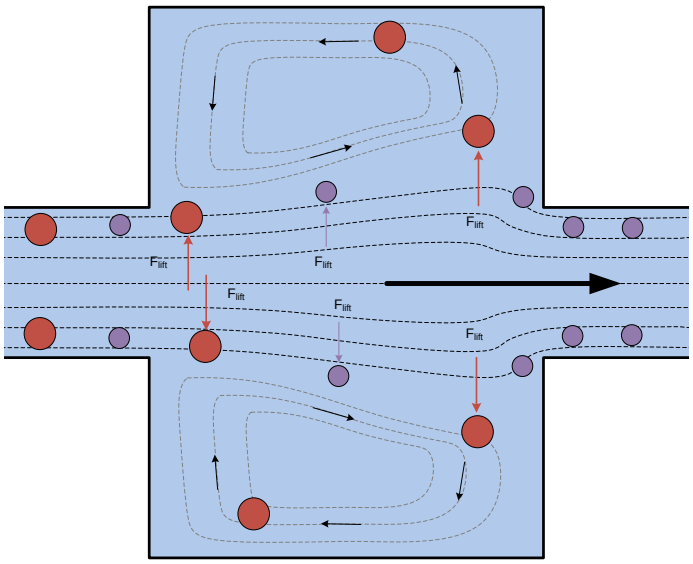

Figure 1-11 Microvorticies for cell separation. Incident cells are aligned along the channel walls due to inertial lift forces. The rapid expansion of the channel causes the main flow to detach and forms microvorticies in the expansions. Cells migrate towards the microvorticies at a rate dependent on their diameter under inertial lift forces.

This mechanism is simple to fabricate, involves no complicated controls, and the high speed required to produce microvorticies guarantees very high throughput. Once again, the separation mechanism is purely size based, limiting the range of suitable applications.

1.5.2.5 Free-flow acoustophoresis

Suspensions placed in a standing acoustic field will arrange themselves such that the densest materials will migrate towards the acoustic nodes in a process known as acoustophoresis. The speed at which a particle migrates depends on its density, size, and compressibility. This phenomenon can be exploited for microfluidic cell separation [**52**]. In one implementation [**53**], cells are initially positioned along a channel wall, and then flowed past an ultrasonic transducer that produces an acoustic node in the channel center (Figure 1-12). The transducer is not long enough for all cells to reach the node, so their ultimate lateral position is determined by their rate of migration.

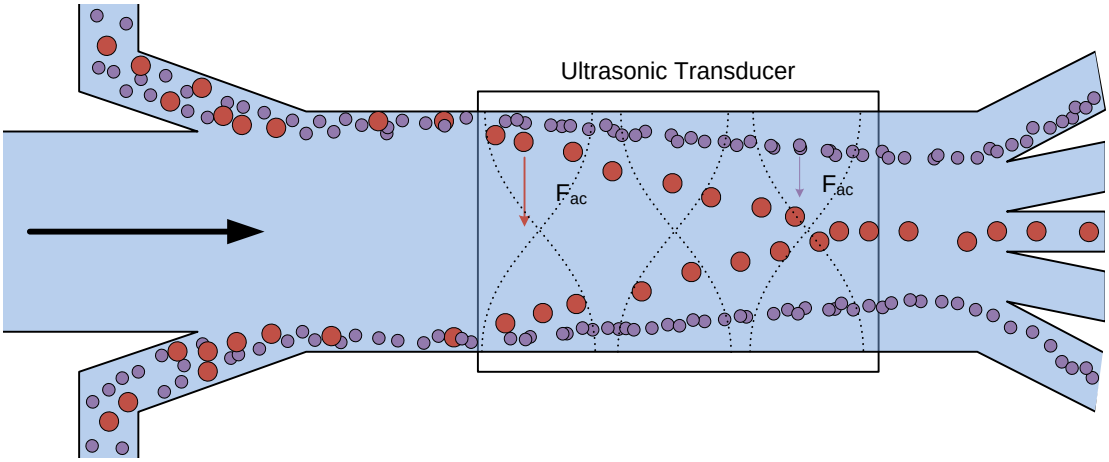

Figure 1-12 Acoustophoresis. Cells placed in a standing acoustic field will migrate towards or away from the nodes of the field depending on their density. The rate of migration is dependent on the cell diameter. The lateral separation produced across the acoustic field is used to divide cells downstream.

Free-flow acoustophoresis has been used to separate polystyrene microparticles [**53**], constituents of whole blood [**53**], and spiked tumor cells from leukocytes [**54**]. Since acoustophoresis discriminates between cells based on variables beyond size alone, it may prove useful for separation applications where size-based separation is insufficient.

1.5.2.6 Micropore Filtration

We conclude our review with the mechanism most similar to the one presented in this thesis: micropore filtration. Micropore filtration involves passing the analyte through a filter array (Figure 1-13). Cells that are smaller than the filter pore size simply pass through the filter, while cells larger than the pore size will either deform through the pore or become stuck. This simple method separates cells based on a combination of size and deformability. A filter with one pore size can be used to produce a binary separation [**1**] [**25**] [**55**] [**56**] [**57**].

Using multiple filter rows with progressively decreasing pore size produces a gradient separation, from the largest and most rigid to the smallest and most deformable [**23**] [**26**] [**58**]. Once the entire sample is processed, the user can manually remove the filter and count the captured cells [**55**] or apply a lateral flow to sweep the cells sideways into an outlet depending on how far through the micropore array the cell traveled.

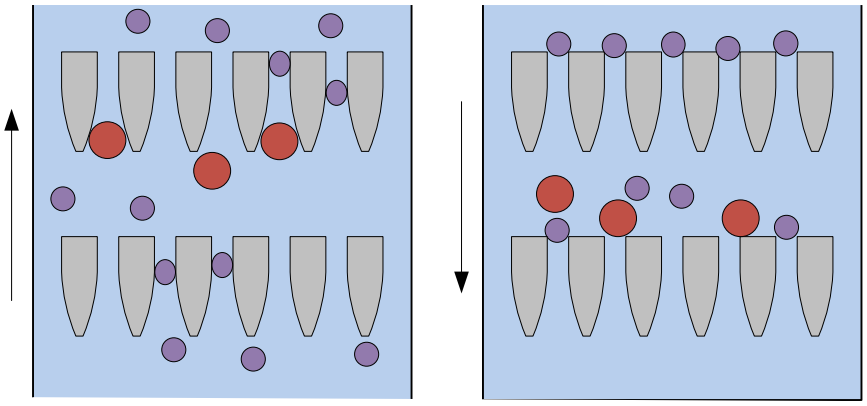

Figure 1-13 Micropore filtration. The cell suspension is passed through arrays of tapered funnels. Small and deformable cells pass through the constrictions while large and rigid cells do not. Temporarily reversing the direction of flow can unclog the channel without reversing the separation.

The main advantage of micropore filtration over alternative techniques is the increased specificity possible when separating based on size and deformability as opposed to size alone. However, the technique is limited by its low throughput (required to avoid physically damaging cells in the constrictions) and failure due to clogging.

Chapter 2 - Device Principles

2.1 The resettable cell trap

The engine of our cell separation device is the resettable cell trap, a microchannel with controllable cross-section.

The resettable cell trap (Figure 2-1) is a 2-layer PDMS structure that forms a sample-carrying flow channel lying above a dead-end control channel. Similar to conventional micro-valves [**10**], the flow and control channels are separated by a thin PDMS diaphragm that can be deflected up or down by an applied pressure difference. To prevent the flow channel from completely sealing when the control channel is inflated, a center fin protruding from the flow channel ceiling acts as a mechanical stop. The ability of a cell to transit through this microstructure is controlled by the cross-sectional opening of the channel, which is in turn controlled by the position of the diaphragm. Given sufficient pressure in the control layer, the diaphragm will deflect upward into contact with the center fin of the flow channel, effectively bisecting the flow channel along its length. The change in stiffness of the diaphragm can be coarsely approximated using the slender beam equation, under which halving the diaphragm width increases the beam stiffness by a factor of 16 [**59**]. This sudden increase in stiffness allows the precise control of the inflation of the diaphragm without precise control of the pressure applied.

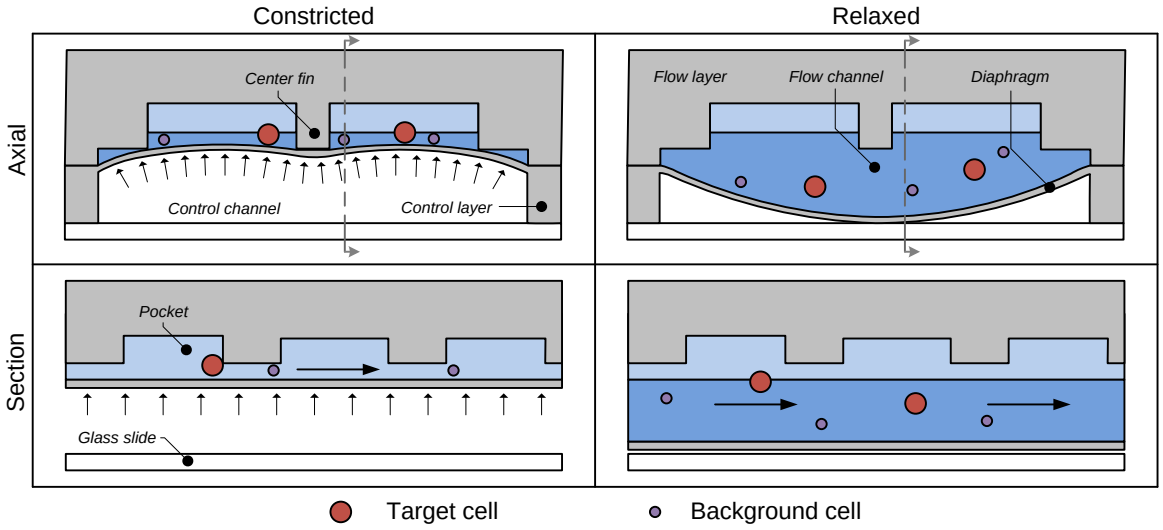

Figure 2-1 The resettable cell trap. Axial and section views are shown for both the constricted and relaxed trap states. The axial view shows the deflection of the diaphragm floor under positive and negative trapping pressures. Section views show the effective flow channel height in both states. The constricted channel only allows the transit of background cells, while the relaxed channel allows the transit of all cells.

While the diaphragm can be deflected continuously, there are two particular positions useful for cell separation. If the pressure difference across the diaphragm, herein known as the **trapping pressure**, is positive, the diaphragm will be deflected upwards into contact with the center fin. The cross-sectional opening of the flow channel is decreased, configuring the trap in the **constricted state**. If the trapping pressure is negative, the diaphragm is deflected downwards, configuring the trap in the **relaxed state**. The cell trap dimensions may be designed such that the constricted state allows the transit of background cells but is sufficiently small to arrest target cells, while the relaxed state is large enough to allow the free flow of all cells. To prevent captured cells from clogging the flow channel, the resettable cell trap features a series of recesses along either side of the center fin that serve as storage compartments for captured cells. The dimensions of the mechanism employed in our prototype cell separation device (Figure 2-2) are designed specifically for the separation of UM-UC13 bladder cancer cells (13-18 μm in diameter) from human leukocytes (8-11 μm in diameter).

The critical difference that distinguishes the resettable cell trap from other micropore filtration mechanisms is the ability to purge the filter on-demand, resetting the trap to its initial empty state. Filter mechanisms with static pores function well when empty, but once a

pore is occupied by a captured cell the pore remains clogged for the remainder of the filtration process. This decreases throughput and can alter the hydrodynamic properties of the filter in an unpredictable way. Our mechanism can circumvent these problems because the resettable cell trap can be relaxed to purge the channel of cells, and then constricted to filter more analyte.

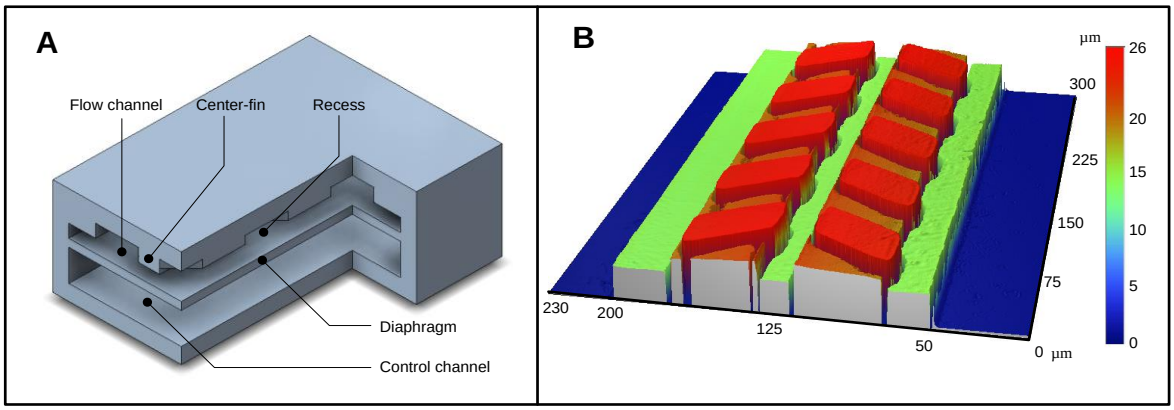

Figure 2-2 Scale model of the resettable cell trap mechanism. A) Isometric cut-away view of the resettable cell trap. The cell suspension flows through the upper channel. Fluid in the lower channel may be pressurized to inflate the diaphragm separating the two layers. B) Profile of the mold for the flow channel as measured by a non-contact profilometer.

2.2 Relationship to previous work

This thesis presents the continuation of a project of a previous student, Tom Gerhardt. The cell separation device described here borrows heavily upon design elements and ideas presented in Gerhardt's work [**60**] [**61**]. In fact, the geometry and layout of the cell trap introduced in Section 2.1 is almost entirely unaltered from his final design. This section will briefly review the previous device development, to serve as both an introduction to the device layout and to clearly distinguish between original contributions of the author and previous work.

Previously, the separation mechanism described in Section 2.1 was used to produce chromatographic separation between target and background cells. In Gerhardt's prototype device, cells flowed through a long cell trap that was periodically constricted and relaxed. The operating principle of the device was that 'by oscillating the flexible membrane between an open [relaxed] position and a semi-closed [constricted] position, size and rigidity dependent flow rates [could be achieved].' The different flow rates across the device could enable chromatographic separation.

Below is a list of the major contributions of Gerhardt's work.

- Designed, fabricated and characterized the resettable cell trap mechanism
- Developed an operating mode to produce chromatographic separation between target and background cells
- Demonstrated a difference in chromatographic behavior of 30 μm and 20 μm microparticles when passed through the mechanism
- Demonstrated a difference in chromatographic behavior between mouse lymphoma cells and erythrocytes when passed through the mechanism

The main limitation of Gerhardt's previous work was the implementation of the resettable cell trap as a tool for chromatography. The cell trap requires several seconds to switch from the relaxed to constricted state and vice versa. In Gerhardt's implementation, the trap must oscillate many times as each cell passes through the trap area in order to impart an average flow rate onto the target and background cells. The need to oscillate the trap puts a limit on the transit speed of cells - individual cells in Gerhardt's experiments required up to 45 seconds to transit the trap. As a result, even a highly parallelized device would suffer from extremely low throughput.

In the broadest sense, the goal of this project is to develop a device that employs the resettable cell trap in a useful way. To achieve this goal, several features and concepts were developed and characterized. The original contributions presented in this document are described below; with the thesis section detailing each contribution is listed in parentheses.

- Developed a new operating cycle for the resettable cell trap, appropriate for separating a bulk cell sample (2.3.1)
- Implemented the resettable cell trap mechanism in a full microfluidic device capable of separating a bulk cell sample (2.3.2)
- Implemented flow focusers for improved target cell retention (4.3)
- Implemented a high-pressure purge to prevent fouling of the mechanism (4.4)
- Calibrated the resettable cell trap mechanism (4.6)
- Characterizing the resolution of the separation mechanism (6.2)

- Characterized the optimal operating conditions of the mechanism through a set of parametric cell separation experiments (6.3)
- Characterized the efficacy of the device by separating two nucleated phenotypes: leukocytes and UC13 cancer cells (6.4)
- Explored the possibility of serial enrichment through sample recycling (6.5)

2.3 Cell separation device design

2.3.1 Filtration vs. chromatography

To separate cells at an adequate throughput, we employ the resettable cell trap mechanism as a physical filter instead of a tool for chromatography. Gerhardt's work has shown that a constricted trap can, under certain conditions, arrest target cells while allowing background cells to flow freely. To use the mechanism as a physical filter we simply hold the captured cells in the trap instead of releasing and re-trapping them repeatedly. This approach removes the need to constrict and relax the channel many times as a cell passes through it, allowing us to flow sample through at much higher speeds. Captured cells will eventually accumulate and threaten to clog the mechanism, so they cannot be held indefinitely. We must periodically relax the trap to release the captured cells, clearing the trap so that it may filter more analyte. If target cells are rare relative to background cells, the period of this catch-and-release cycle will be long, allowing near continuous processing of sample.

Implementing this filtration based approach requires a repeating three-step process, comprising filtration, purging, and collection (Figure 2-3). In the filtration step, the analyte is flowed through a constricted cell trap and the effluent is directed into the waste reservoir. Target cells accumulate at the constricted trap while background cells flow through the trap and into the waste reservoir. Eventually the trap's recesses will fill with target cells and flow through the channel will be obstructed. In experiments we observed a dramatic decrease in the ability of leukocytes to transit through a trap once it held more than two target cells. Accordingly, the duration of the filtration step was limited such that a volume of analyte containing no more than two target cells per trap before purging. In the purging step, the trap remains constricted while buffer fluid flows through the trap towards the waste outlet to remove background cells from trap area. This step typically requires 5-10 seconds. Finally, in the collection step, the cell trap is opened and the released target cells flow into the collection

reservoir. The release flow is sourced from a separate buffer inlet with a higher pressure to create increased flow rate, and therefore, greater shear forces to remove cells that may have adhered to the walls of the cell traps [**62**].

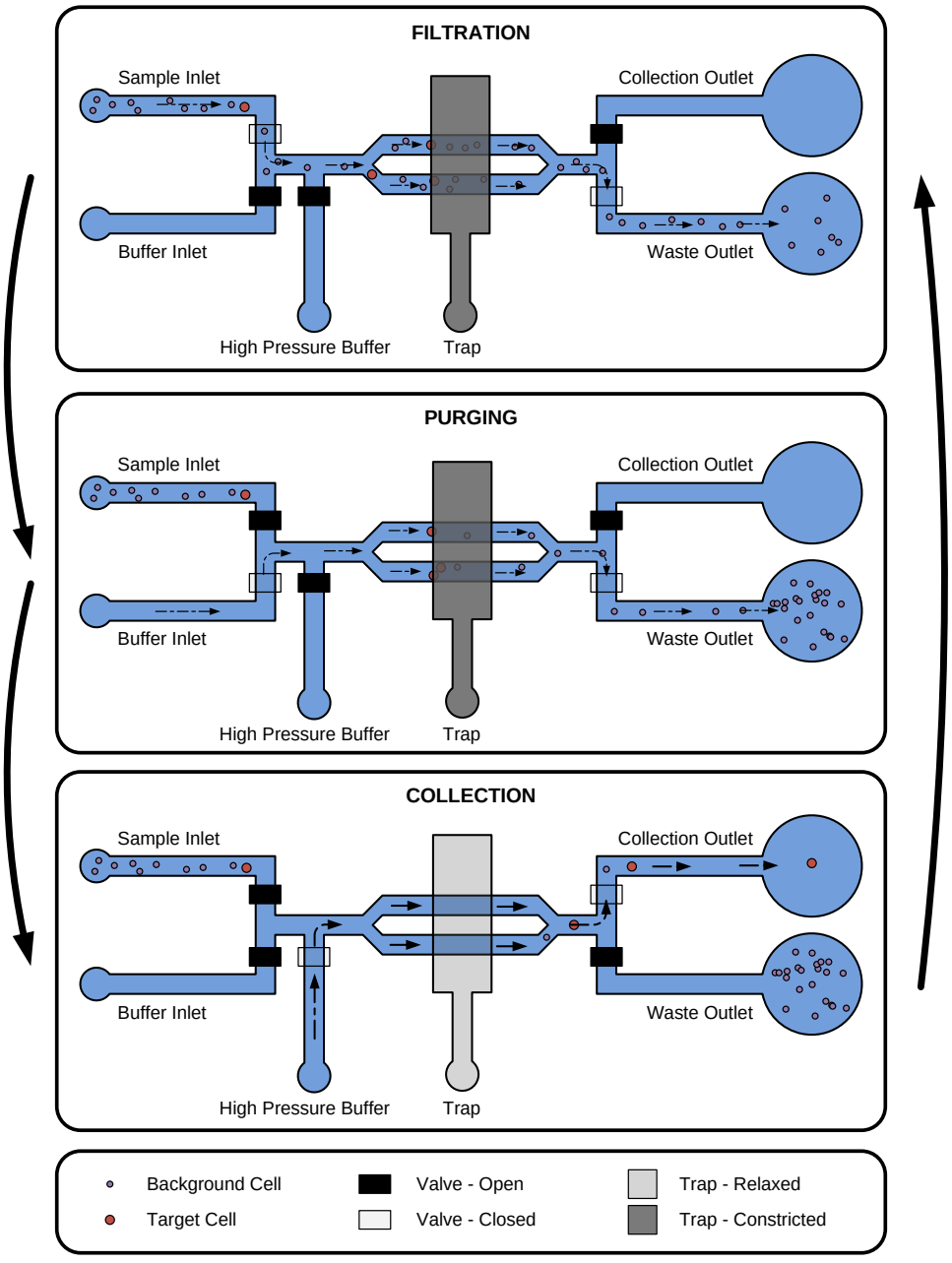

Figure 2-3 Operational cycle for cell separation device. Filtration - mixed sample is flowed from the inlet past the constricted trap. Target cells are retained at the head of the trap and background cells pass through to the waste outlet. Purging - the sample inlet is closed and buffer is flowed past the still constricted trap to purge the area in between valves of background cells. Collection - the trap is relaxed and high pressure buffer pushes the released cells into the collection outlet. Any background cells that were trapped or adhered to the channel walls may also be collected.

2.3.2 Device layout

We designed and fabricated a microfluidic device to implement filtration based cycle described in the previous section. Figure 2-4 below shows a photograph of the microfluidic device. The nomenclature introduced in the figure will be used throughout this document.

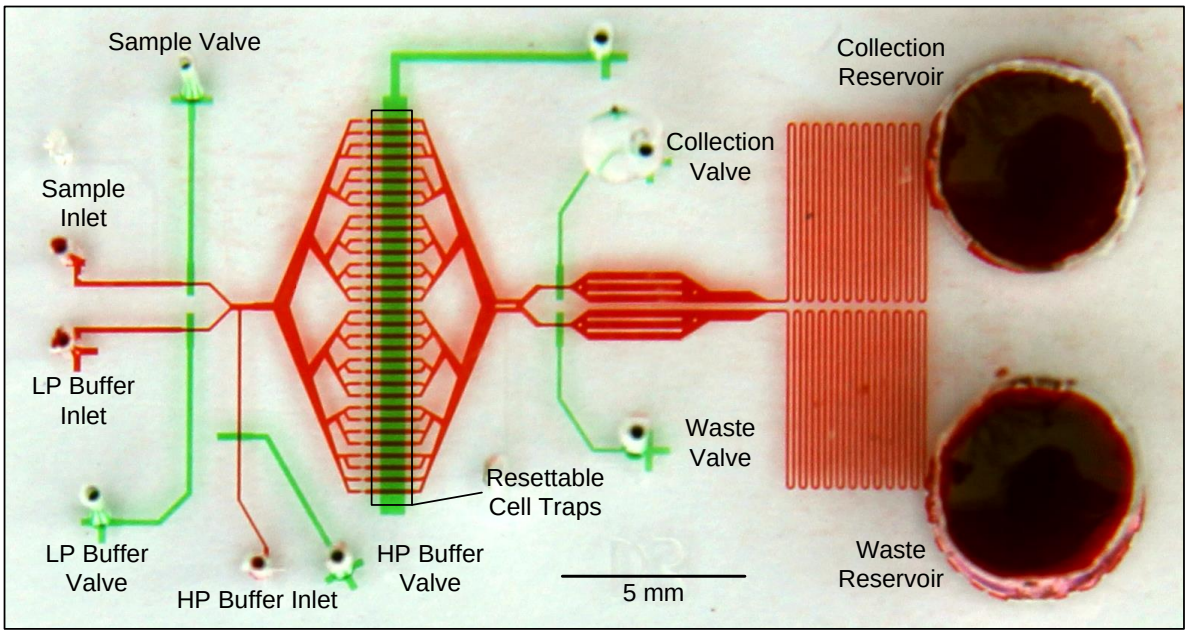

Figure 2-4 Top view photograph of the cell separation prototype. Flow moves from left to right. Flow channels and control channels are filled with red and green food coloring, respectively. Valves are formed in areas where flow and control channels overlap. The resettable cell traps are formed at the intersection of the wide control channel and parallelized flow channels.

The prototype microfluidic device features 32 parallel cell traps to facilitate rapid processing of bulk sample while keeping the full footprint of the chip small enough for normal fabrication procedures. Separated cells are directed to one of two 200-400 µL on-chip reservoirs, where the cells can be counted and collected for post-processing. Other features of the device are detailed in Chapter 4.

2.3.3 Experimental parameters and predicted performance

The design and operational parameters of the device can generally be broken into two fields: those affecting the device throughput, and those affecting the trapping rate of target and background cells. The throughput is determined by the hydraulic resistance and operational cycle of the device, and as such can be quantitatively estimated. The trapping rate of cells is a multiphysics problem – determined by coupled fluid dynamics, solid dynamics, and biomechanical properties of cells which themselves are variable. We will not attempt to

produce a model for the trapping rate of cells, but instead we will conjecture on the dependence of trapping rate on the free operational parameters.

Throughput is the product of volumetric flow rate and concentration, given by:

$$\dot{N} = n_{ch} \cdot C \cdot Q_{ch} \tag{2.6}$$

$$\dot{N} = n_{ch} \cdot C \cdot u_{ch} \cdot A \tag{2.7}$$

Where $\dot{N}$ is the number throughput of the whole device in cells / unit time
n_{ch} is the number of parallel resettable cell traps in the device
C is the concentration of the analyte in cells / unit volume
Q_{ch} is the volumetric throughput of a single resettable cell trap
u_{ch} is the average fluid speed through a resettable cell trap
A is the cross sectional area of a constricted resettable cell trap

While high throughput is desirable and concentration and flow rate are free parameters, it is reasonable to assume that there is a maximum sample concentration and flow rate practical for cell separation beyond which the device either performs poorly or fails entirely. Experiments to characterize these limits are described in Section 6.3, but we can produce an early estimate based on parameters from other cell separation devices presented in the literature. In devices that separate nucleated cell phenotypes, the total sample concentration is typically between 10^6 and 10^7 cells/mL [**55**] [**23**]. The linear flow speed of cells through micropore filtration devices is between 100 and 1000 μm/s [**25**] [**23**]. The cross sectional area of the constricted trap is approximately 600 μm^2, and our device features 32 parallel channels. An estimate throughput range based on these values is 10^4 to 10^6 cells/hour. While the estimate is coarse, it suggests that the device will be fast enough to allow statistically significant measurements of enrichment and retention.

Chapter 3 - Methods

3.1 Experimental apparatus

The experimental apparatus consists of the microfluidic device for separating cells, a system for controlling the various fluidic connections to the microfluidic device, and a microscopy apparatus for data acquisition. A schematic of the apparatus is shown in Figure 3-1 below.

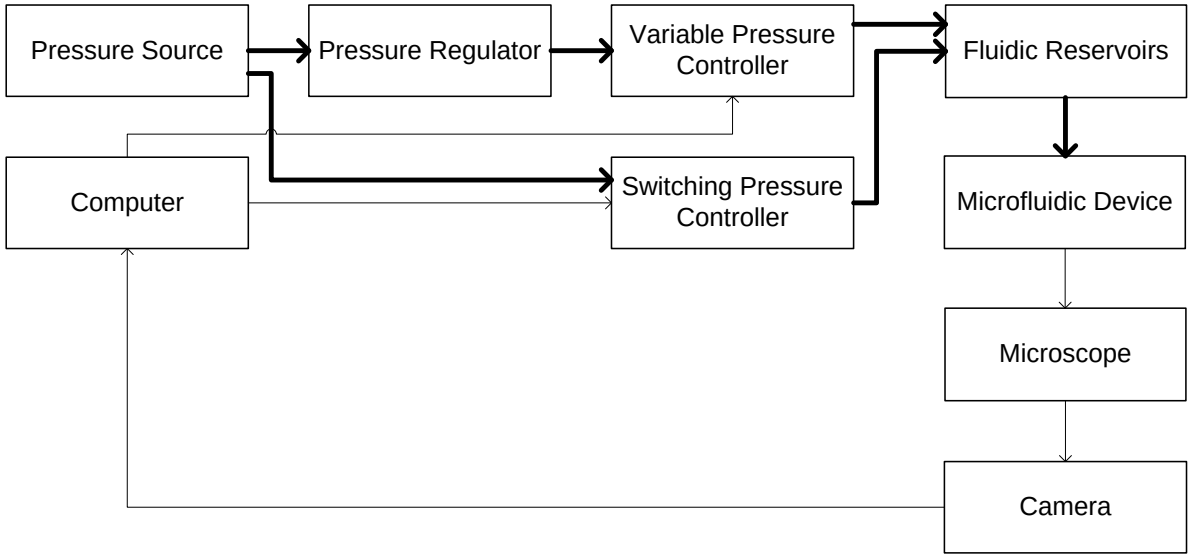

Figure 3-1 Block diagram of the experimental apparatus. Bold lines denote physical connections; thin lines denote electrical/optical connections. Software running on the computer both controls the pressure delivered to various fluidic reservoirs and collects video and/or image data from the camera microscope.

The layout of the equipment will be described sequentially, beginning with the pressure control apparatus. A reservoir supplies pressure to the controllers. The apparatus employs two different pressure controllers to control the flow on the device. A variable pressure controller (MFCS-4C, Fluigent) allows tunable pressure control over a range of 0-1 bar on four independent channels. To avoid exceeding the maximum 1 bar input pressure on the variable controller, a pressure regulator (Omega Engineering PRG700, Shanghai, China) is installed between the reservoir and the controller. The variable controller is used for fluidic lines where precise (±1 mbar) pressure control is required: the sample inlet, the buffer inlet and the cell trap. A second pressure controller is used for fast on/off switching of lines at pressures of more than 1 bar, specifically purposed for controlling microfluidic valves. This custom made device comprises solenoid valves (Pneumadyne, Plymouth, Minnesota) controlled through a computer via a microprocessor (MSP430, Texas Instruments).

Fluids to be used in the microfluidic device are held in reservoirs. A reservoir consists of a 10 mL polypropylene tube (BD Falcon Tubes) capped by a custom lid featuring an inlet for pressurization and an orifice for drawing fluid out of the tube. Pressure is delivered to the reservoir through 1.6mm ID flexible tubing. Fluid is drawn out of the reservoir through 0.02 in ID tubing (Tygon, Cole-Parmer) which is connected to the microfluidic device through a small stainless steel tube (New England Small Tube). Any tubing that delivers fluid to a flow channel is replaced or flushed with a 70% ethanol solution then flushed again with deionized water.

Prior to conducting a cell separation experiment, the microfluidic device must be connected to the apparatus and primed. First, the flow and control inlets on the microfluidic device are connected to the appropriate fluid reservoirs and pressure sources. The device channels are then primed: control channels are filled with deionized water, and flow channels are filled with a solution of PBS + 5% BSA + 0.5% Pluronic. Any air pockets remaining are forced out of the device by applying pressure to the fluid, employing the permeability of PDMS to air. The outlet reservoirs are manually cleared of dust or debris by flushing with PBS. The priming solution is then left to prime for a minimum of 30 minutes before the cell separation experiment begins.

3.2 Microfluidic device fabrication

The microfluidic devices used for cell separation are fabricated using standard multilayer soft lithography [**10**] techniques. A schematic of the fabrication process, detailing photolithography, mold making, and soft lithography, is shown in Figure 3-2 below. Detailed methodologies for these processes are included in Appendix B.

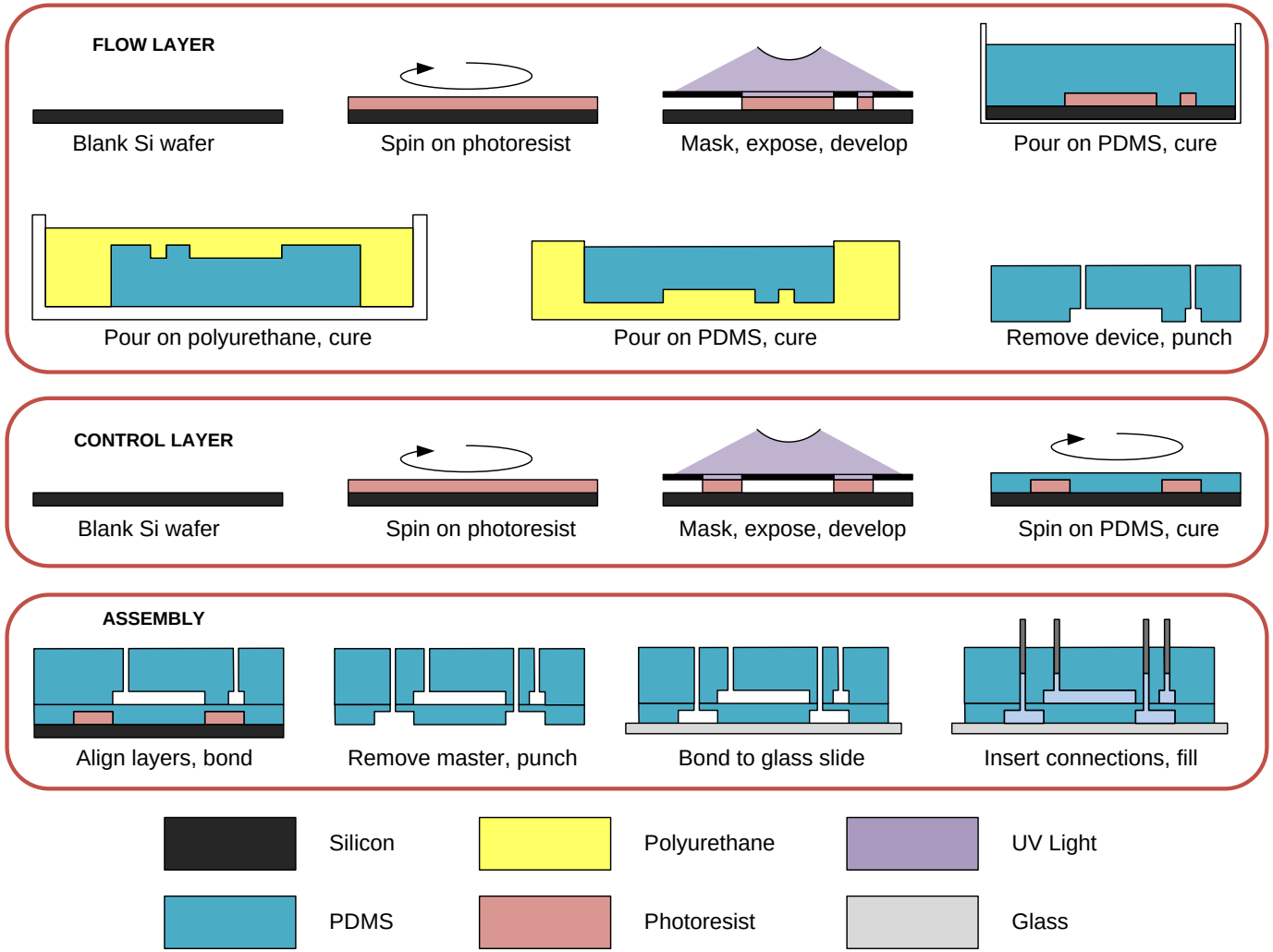

Figure 3-2 Multilayer soft lithography fabrication process. Repeating the photolithography steps is unnecessary to fabricate additional copies of the prototype - flow layers can be cast from the polyurethane mold and control layers spun onto the featured wafer.

3.3 Analyte preparation

The analyte used in cell separation experiments was a heterogeneous mixture of nucleated blood cells (leukocytes) obtained from healthy donors and UM-UC13 bladder cancer cells. Leukocytes were extracted from whole blood, drawn from healthy donors into 6 mL EDTA blood collection tubes, using density gradient centrifugation. In a 15 mL centrifuge tube, 2 mL of whole blood was carefully layered over 2 mL of Histopaque 1119 (Sigma-Aldrich, St. Louis, MO). The tube was centrifuged at 400g for 40 minutes. The leukocyte layer was then transferred into a 15 mL tube containing 10 mL of HBSS without Ca2+ and Mg2+ solution (Invitrogen, Grand Island, NY) and centrifuged at 200g for 10 minutes. The supernatant was removed and the remaining cells washed again with HBSS. UC13 bladder cancer cells were cultured in MEM solution with the addition of 10% (v/v) fetal bovine serum, 1% L-glutamine, 1% MEM Non-Essential Amino Acids, 1% Sodium Pyruvate (Invitrogen), and 1% Penicillin Streptomycin (Fisher Thermo Scientific, Waltham, MA), and incubated at 37^{o}C in a humidified environment with 5% CO2. For separation experiments, the cells were suspended in MEM with 5% bovine serum albumin (BSA) and 0.2% Pluronic (Invitrogen) to mitigate nonspecific adsorption of cells to the channel walls. Cancer cells were stained with calcein AM (Invitrogen) and leukocytes were stained with Hoechst 33342 (Invitrogen).

3.4 Data analysis

To quantify the performance of the cell separation device according to the metrics introduced in Section 1.3.3, we needed a method for counting the number of target and background cells that were collected and rejected in an experiment. To this end, we investigated video analysis, on-chip flow cytometry and post-experiment imaging. Video analysis was appropriate for short experiments, but the need for high frame rate and long videos caused file sizes to quickly exceed the capacity of the computer. On-chip flow cytometry has been implemented in microfluidic devices [**63**] [**64**] but this approach requires embedded optics and was deemed too technically challenging and time consuming. We ultimately chose to count cells through static imaging of the waste and collection outlets, an attractive approach given the availability of software to facilitate the acquisition of high-resolution images through image stitching.

After each cell separation experiment, high resolution images were taken of the waste and collection reservoir under green and blue fluorescent filters to discriminate stained cells from debris and background features. Microscopy software (NIS-Elements BR) combined with an automated stage allowed a large array of images to be taken automatically, spanning the area of the reservoir. Exposure, illumination and focal plane were maintained throughout image acquisition. Individual images from a single outlet were stitched together (NIS-Elements BR or Microsoft Image Composite Editor) to form a high-resolution composite. A complete set of stitched images for a single experiment is shown below in Figure 3-3.

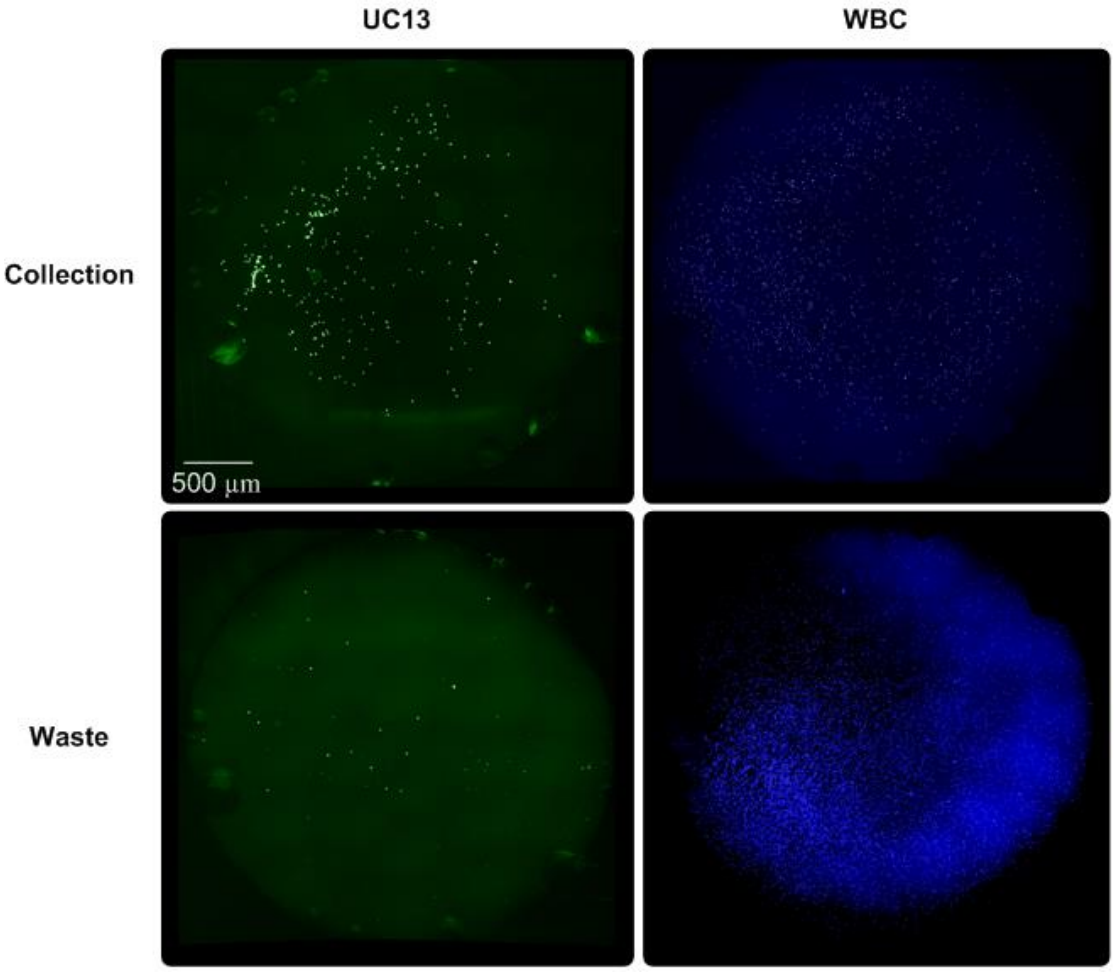

Figure 3-3 Stitched images from a single cell separation experiment. Both the waste and the collection outlet were imaged under fluorescent light and a green and blue filter, illuminating the UC13 and leukocyte populations respectively. Individual cells are distinct in all images except the leukocyte waste where cells are packed too closely for counting.

Cell counting was done manually for reservoirs that held a small number of cells (N<500). To save time and tedium, reservoirs with many cells were counted using an automatic image processing script in ImageJ. In this script, the composite image is manually thresholded, binarized, eroded, dilated, and then watershed. Connected components in the watershed image are counted automatically to determine the total cell count. Comparisons of this automatic process with manual counting yielded values agreeing to within 5%, typically underestimating the manual value as a result of incomplete watershedding of overlapping cells. The image processing sequence is demonstrated on a sample image of UC13 cells in Figure 3-4 below. The ImageJ macro code used for this process is included in Appendix C.

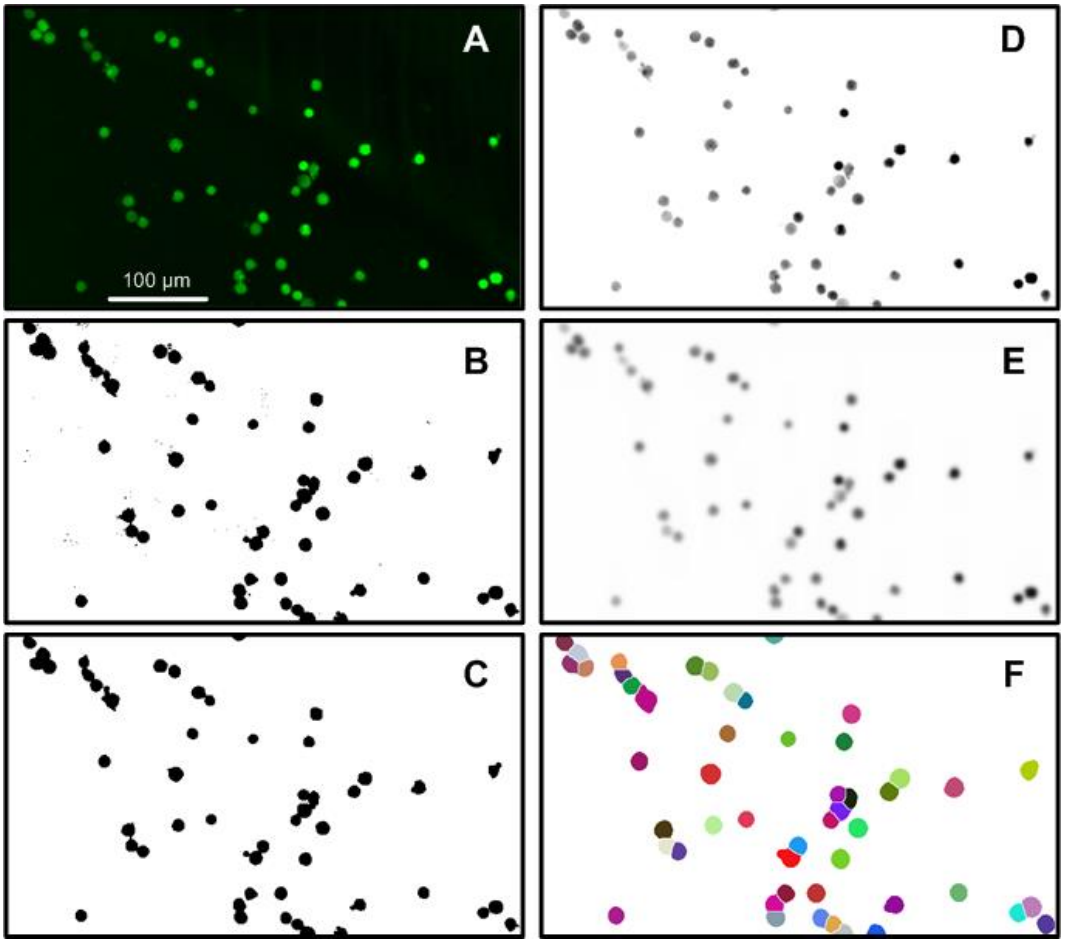

Figure 3-4 Image processing sequence for counting cells. A) Raw image swatch from a collection outlet. Illumination is a combination of bright field and fluorescence lamps. B) Binary image after manual thresholding. Some noise remains as an artifact of thresholding. C) Binary mask after erosion/dilation. Noise from B is removed. D) The 8-bit raw image is masked with C to remove background elements. E) Masked image after Gaussian smoothing of 3 pixel radius. F) Result of grayscale watershedding. Separate connected components are shown in different colors. Computer counting identifies 50 cells. Manual counting identifies 51 cells.

Some of the entities imaged in the outlet wells were excluded from the cell count. Specifically, a small fraction of the cells drawn from UC13 culture appeared as a different phenotype to the majority of the UC13, and were excluded. Approximately 5-10% of entities drawn from culture were small, irregular in shape, and fluoresced weakly or not at all. These entities, whether they are dead cells or cell fragments or perhaps something else, are easily distinguishable from regular UC13. For comparison, example fluorescent and bright-field images of normal and excluded entities are shown in Figure 3-5 below. The regular UC13 cells had the physical properties required to act as a target cell in separation experiments, and the small irregular entities did not. The small entities were therefore not considered in the separation experiments and excluded from counting in both the manual and automatic counting techniques.

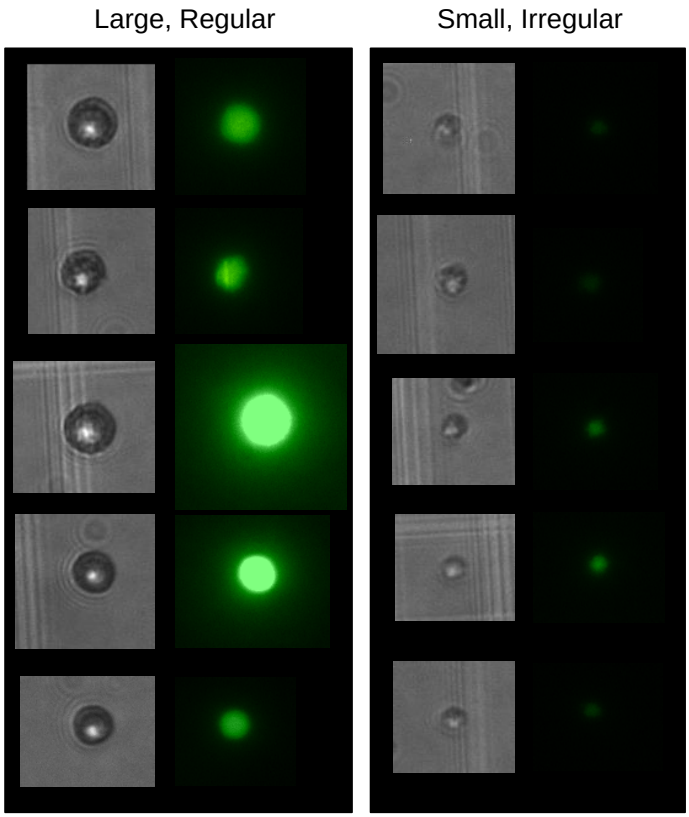

Figure 3-5 Bright-field and fluorescent images UC13 cells. Each image was taken with identical illumination and exposure. Cells in the left hand column are large, spherical in shape and fluoresce brightly. These cells were counted in cell separation experiments. The small and irregular entities in the right hand column were ignored in cell separation experiments.

Chapter 4 – Device Design Details and Characterization

4.1 Introduction

In Chapter 2, we described the key principles of the cell separation mechanism. In this chapter, we describe and characterize supporting design elements. Bulk cell separation could likely be achieved with the separation mechanism and operational cycle alone, but the elements of this chapter improve the efficacy and reliability of the overall device performance. The chapter concludes with a generic approach for tuning the resettable cell trap device to a specific cell separation application.

4.2 Bifurcation network

Cell separation applications where target cells are rare require high throughput separation techniques. The typically small throughput of microfluidic techniques can be increased through a variety of means, the simplest of which is parallelization. The multilayer soft lithography process allows for massive parallelization without a corresponding increase in fabrication complexity, requiring only a bifurcation network to route analyte from the inlet to the parallelized cell traps. The ideal bifurcation network should evenly partition both the fluid and the suspended cells, and do so with a relatively small footprint.

Depending on the application, the designer may desire the even splitting of either particles or fluid volume. When the Stokes number and dimensionless size (particle diameter/channel width) of the particle is small (<0.05) these tasks are essentially one and the same. However, as the dimensionless size approaches unity, even splitting of particles and volume become distinct objectives [**65**] [**66**] [**67**]. The difference arises from the finite size of the particle and physical interactions between the particle and the channel walls.

The lateral position of the center of particles introduced into the bifurcation network form a uniform distribution, except for regions next to the channel walls where particles are excluded because they can move no closer without intersecting the wall. After a single bifurcation the concentration profiles are shifted considerably, as shown below in Figure 4-1.

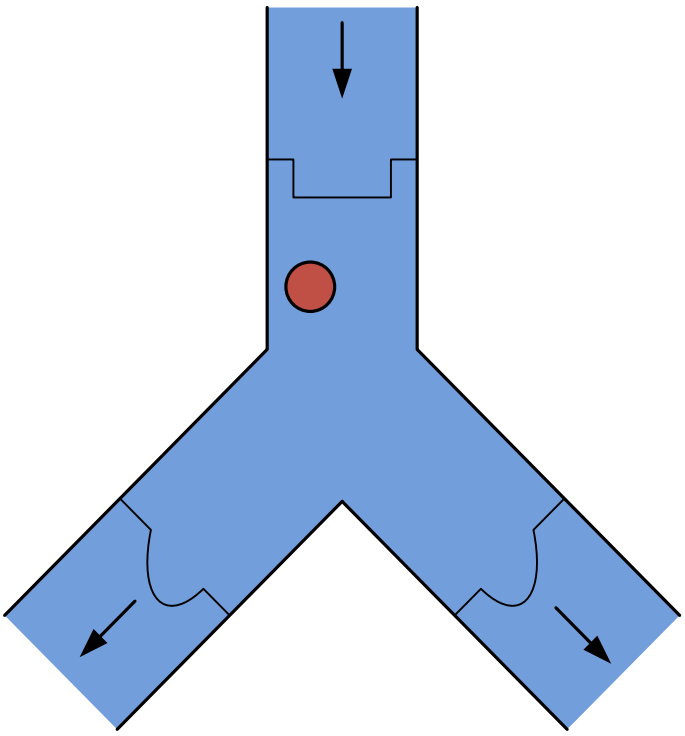

Figure 4-1 Concentration profiles of particle centers entering and exiting a bifurcation. Upstream of the bifurcation the particle has an equal probability of being in any lateral position in the channel except for the excluded area within one particle radius of the channel wall. Downstream of the bifurcation there is an asymmetry in the concentration profile. Figure adapted from [66**].**

The concentration profiles of particles downstream of a bifurcation can be measured experimentally or modeled computationally [**68**]. The computational approach uses an iterative dynamic relaxation technique wherein the flow field around the upstream particle is solved, the forces and moments on the particle computed, and the particle position updated over many small time steps. A simpler, but less accurate model involves finding the free flow solution of the channel and assuming that a particle follows the streamline that passes through its center.

The models and experimental results indicate that flowing particles through a bifurcation will produce an asymmetry in the downstream particle concentration profiles, with more particles located towards the inner wall than the outer wall. This asymmetry stems from the excluded streamlines occupying a greater fraction of the bifurcated channels, so the magnitude of the asymmetry increases with the width of the excluded zone. Over a series of bifurcations, this

asymmetry is compounded and may fully deplete the outermost channels of all particles, as illustrated in Figure 4-2 below.

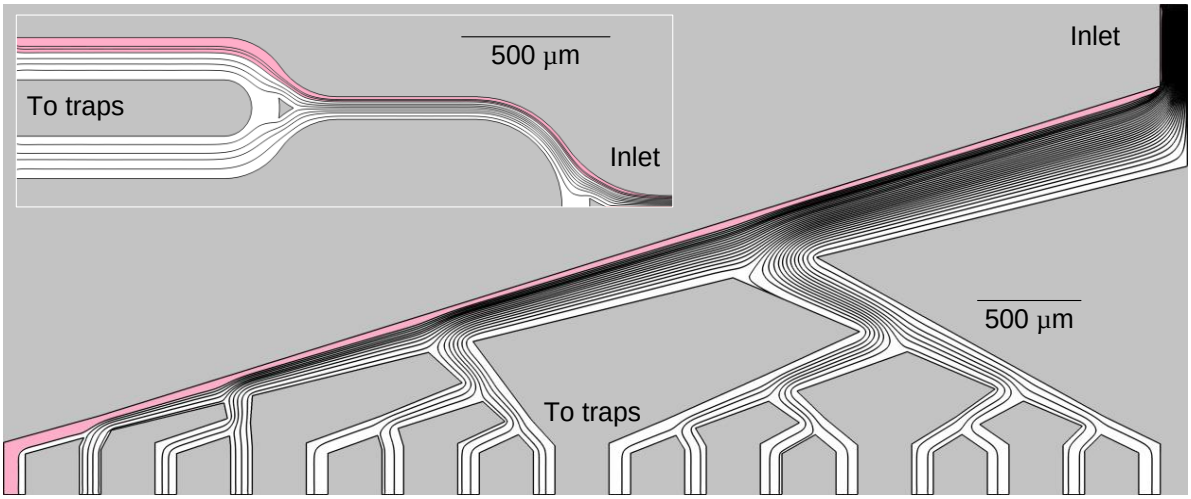

Figure 4-2 The bifurcation skimming effect. Main: Computationally generated streamlines show the fluid path through one half of the 32 channel bifurcation network. The excluded area for a 15 micron particle, highlighted in red, grows larger through the network. The outermost channel would likely be very cell-poor. Inset: The same effect is shown for Gerhardt's prototype device. Since the channels here are of a smaller width, the excluded zone grows large over just two bifurcations.

This phenomenon, called the Zweifach-Fung effect, has been exploited to extract plasma from blood in a process known as plasma skimming [**69**]. We wish to achieve even distribution of cells across the bifurcation network, and must therefore mitigate the effect. Since the effect relies on a high dimensionless particle size, the simplest solution is to increase the width of the bifurcation channels. To this end we are limited by the 10:1 rule [**70**] of microfluidic design which requires all channels have aspect ratio (width:height) of no more than 10:1 in order to avoid channel collapse during fabrication. This aspect ratio is adopted in the prototype bifurcation designs to maximize the width of the bifurcation channels.

To minimize the footprint of the bifurcation network, we adopted a design for a compact, asymmetric network that maintains equal fluidic throughput and hydrodynamic resistance as suggested in the literature [**67**]. Seen in Figure 4-3, the asymmetric network provides a 36% decrease in footprint over a conventional T-junction design.

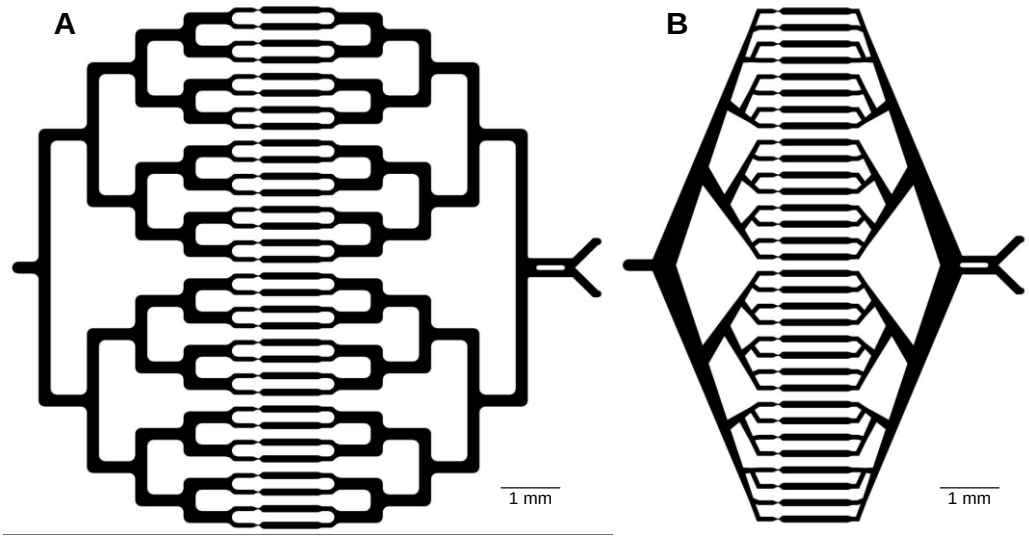

Figure 4-3 Comparison of T and asymmetric bifurcation networks. Two networks connecting a set of 32 parallelized separation channels are shown. A) Typical T-junction bifurcation with base channel width of 250 µm. B) Asymmetric bifurcation network designed from [67**], with base width of 250 µm**

4.3 Flow focusers

The resettable cell trap can capture cells by decreasing its height below some threshold value. However, the constricted trap is not perfectly rectangular in cross-section – the diaphragm is bound at the channel edges, so the constricted channel will always be taller at the edges than in the center. The tall channel edges present a problem, as target cells that would have been trapped at the narrow channel center may leak through at the edges. This failure mode was identified in Gerhardt's work, and addressed with the addition of a protrusion to the channel ceiling on either side. With these protrusions in place, the cross-section of a constricted trap has four openings, as shown in Figure 4-4A. The side protrusions separate the main body of the flow channel, close to rectangular in shape, and the triangular side channel.

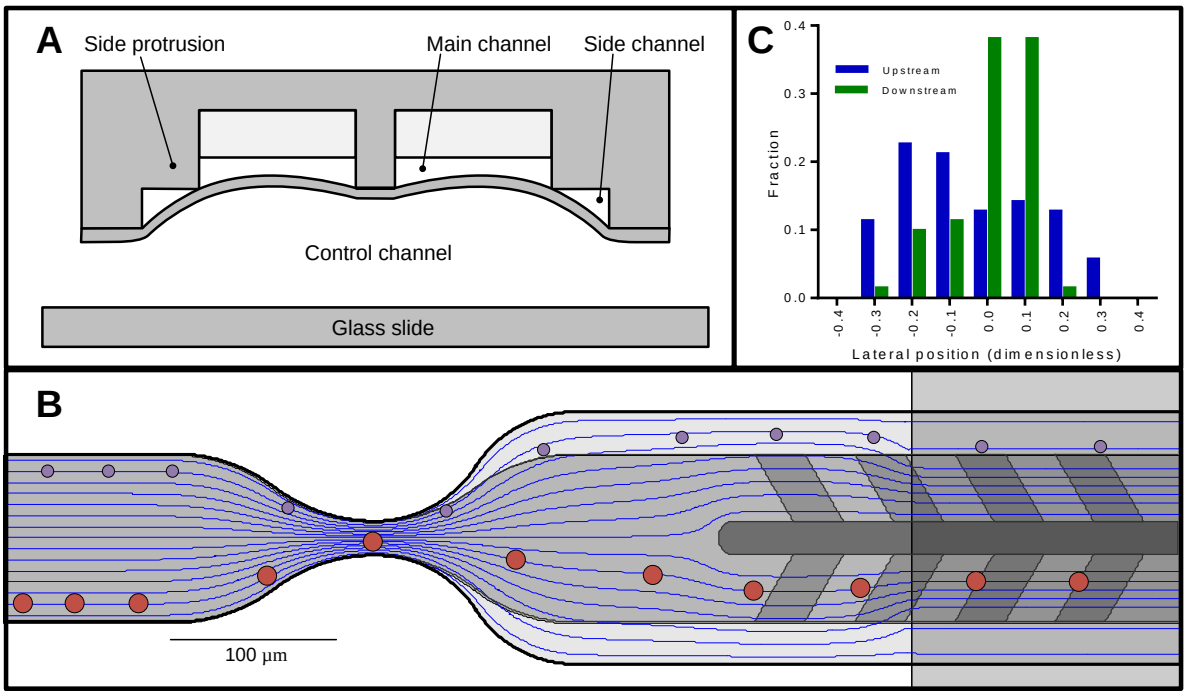

Figure 4-4 The pinched flow cell focuser. A) Axial view down the constricted cell trap. B) Pinched flow cell focusing principle. Cells flowing past a contraction-expansion channel of comparable width to the cells diameter are focused into the channel center. Above, a small cell is not brought into contact with the channel wall and follows its streamline to the channel exit. Below, a large cell is bumped from its streamline at the constriction and leaves the channel in a more centered position than it came in. C) A histogram of dimensionless lateral cell positions upstream and downstream of the focuser illustrates the desired focusing effect.

Unfortunately, early experimental work indicated that the side protrusions were unable to prevent UC13 cells from entering the side channels. The mechanism required modification if it were to achieve acceptable target cell retention. We considered producing a flow channel with rounded sides to match the shape of the inflated diaphragm, but the planar nature of photolithography makes this a challenging and expensive fabrication task. An alternative approach would keep the side channels, but ensure that no target cells entered. To achieve this we centered the incoming flow of cells using pinched flow focusers upstream of the traps.

Pinched flow focusers are passive elements capable of manipulating the trajectories of particles in microfluidic suspensions based on their size. As discussed in Section 1.5.2.1, pinched flow focusers may be used as a size based cell separation mechanism [**40**] [**37**] [**71**]. The focusers are constrictions in a channel that cause streamlines to converge, bringing

flowing particles into contact with the channel walls. Contact with the solid structures breaks the reversibility characteristic of Stokes flow, forcing the particles to move laterally into a more centered streamline as they continue to flow. Using this simple concept, we designed a focuser to center incident target cells. The focuser, shown in Figure 4-4-B, consists simply of a contraction and expansion in the channel width where the width at the constriction (20 μm) is comparable to the diameter of the target cells (15 μm). The constriction causes streamlines to bunch together – cells that were following streamlines close to the wall will be forced towards the center if they are sufficiently large. The focusing effect is illustrated by the mock trajectories of large and small particles following computationally generated streamlines (COMSOL Multiphysics) until they bump against the channel wall at the focuser constriction.

The efficacy of the focuser was experimentally evaluated by flowing UC13 cells past the focuser and towards a constricted cell trap. Video measurement of the lateral position of cells upstream and downstream of the pinched flow focuser, shown in Figure 4-4C, show a strong shift in particle distribution towards the center of the channel as expected. The asymmetry in the downstream position distribution is likely due to a small misalignment of the focuser and cell trap from the photolithographic process. Importantly, 0 of 70 cells in the experiment were observed entering the triangular channel openings in the trapping area. The pinched flow focuser performs the required function.

4.4 High pressure purge

Leukocytes are known to adhere to the PDMS walls of microfluidic channels under certain conditions [**62**]. The non-specific adhesion of cells to the device walls present a possible failure mode of the device, as adhered cells will occlude the channels of the device and increase the probability of capturing subsequent cells. Adhesion is particularly prevalent within the cell traps since cells can be in contact with up to four channel walls simultaneously, presenting a large surface area on which adhesive bonds may form. A single cell adhered within a cell trap occupies a greater fraction of the channel cross section than in larger channels elsewhere in the device, so adhesion within the traps may quickly lead to clogging.

In [**72**], a general framework for modeling the adhesion of cells to other cells and surfaces is presented, suggesting that non-specific bonds are formed per μm^2 of surface contact and that Stokes drag induced by flow past an adhered cell may be sufficient to overcome this bond. In [**73**], the adherent properties of leukocytes to PDMS were studied experimentally. The results give a qualitative description of leukocyte adhesion under different conditions, and suggest in particular that adhesion can be minimized with high shear rates and low cell concentration. These studies suggest a high flow speed during normal separation helps prevent cell adhesion, and that an even higher speed purge phase can assist in removing those cell that did adhere. Accordingly, we added a high pressure purge phase to the operational cycle of the device.

The device layout as shown in Figure 2-4 features three separate inlets on the left hand side of the device: one carrying the sample to be sorted, and two carrying buffer fluid for purging the cell traps. While the extra buffer inlet appears redundant, it is maintained at a much higher pressure than either the flow or low pressure buffer inlets, delivering high speed buffer flow that scrapes the channel walls of cells that may have adhered during the filtration phase. The speed of the purge phase is limited by the closing pressure of the valves (to avoid undesired backflow into other inlets) which is in turn limited by the bonding strength of the device. The plasma and diffusion bonds that join the layers of the device have been observed to rupture when pressurized above 4 bar, so on-chip valves were actuated with a pressure of 3 bar and the high pressure purge inlet was pressurized to 2 bar. For reference, the cell sample is typically pressurized to 200-800 mbar. The purge step is short in duration, experimental observation suggested that adhered cells under a high speed flow will either release immediately or not at all. Figure 4-5 below shows the effect of the high pressure purge on leukocytes adhered within the cell traps.

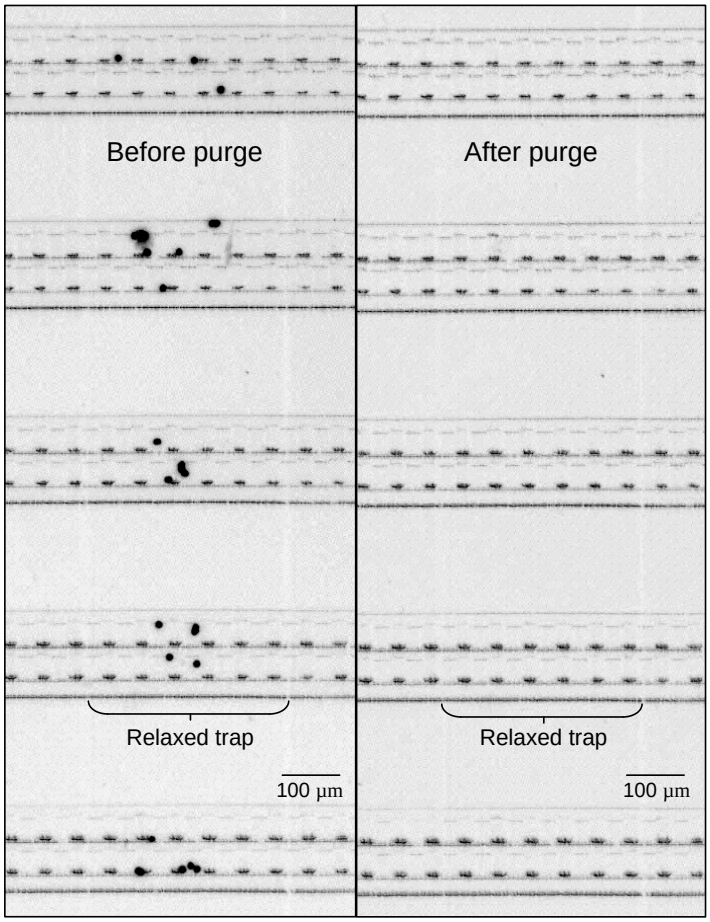

Figure 4-5 Cell traps before and after a high pressure purge. Leukocytes, appearing as dark spots in the left frame, remain adhered to the cell trap walls even after the trap is relaxed and purged in the collection phase. The high pressure purge detaches the adhered leukocytes and empties the trap.

Typically, the high pressure purge removes some of the adhered cells but does not always empty the channel. Interestingly, the total number of adhered cells does not noticeably increase over the course of several separation cycles. We suspect that certain locations in the device offer greater contact area than others, and once those are occupied by adhered cells no more can join.

4.5 Physical properties of model cells

The resettable cell trap operates on the premise that target cells and background cells have distinct physical properties, specifically size and deformability. Before conducting full cell separation experiments, it is important to quantify these properties for the model target and background cells chosen: UC13 and human leukocytes.

To determine the size distribution of leukocytes and UC13, approximately 100 cells of each phenotype were individually imaged under a calibrated 60x objective lens after manually focusing. A watershed operation performed using image processing software (ImageJ) provided a measurement of a cell area from which cell diameter was estimated by approximating the cell perimeter as a circle. The cell diameter distributions are shown below in Figure 4-6A below.

Measurements of cell deformability were performed by other members of our research group (Guan Quo and Lin Wang) using microfluidic micropipette aspiration [**74**]. In this technique, deformability is characterized by the pressure required to push individual cells through a microscale funnel. Differences in cell diameter are accounted for in this method by modeling the cell as a liquid filled sac with some isotropic cortical tension determining deformability. Cortical tension measurements, shown in Figure 4-6B below, are based off the average and standard deviation of 100 individual measurements.

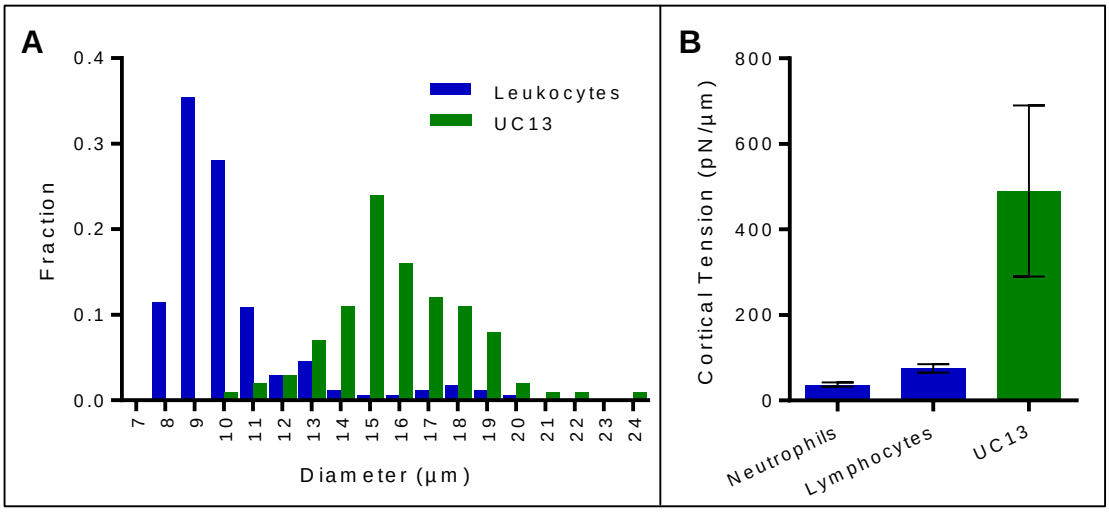

Figure 4-6 Physical properties of model cells. A) Size distribution of UC13 and leukocytes. The distributions overlap in the 10-14 µm range. B) Deformability of neutrophils, lymphocytes, and UC13 as measured by microfluidic micropipette aspiration.

The size distribution of leukocytes and UC13 overlap, but their deformabilities differ considerably. Interestingly, the size overlap would limit the effectiveness of some of the purely size based separation techniques discussed in Section 1.5. Since the resettable cell trap discriminates based off of size and deformability, it may be able to outperform purely

size based methods when dealing with these particular phenotypes. We explore this idea further in Section 7.1.

4.6 Experiment plan

Based on the design and experiment described thus far, we had developed a platform for cell separation that was near ready for bulk cell separation experiments. To review the essential design components, this document has described:

- The resettable cell trap – a mechanism to control the cross-section of a microchannel
- A microfluidic device that features many parallel cell traps and the necessary microfluidic plumbing to facilitate the separation of cells from a bulk heterogeneous sample
- An operational cycle for continuous cell separation
- A method for quantifying the results of cell separation experiments

To use these tools for label-free cell separation, we must first characterize the way the relevant cell phenotypes, specifically UC13 and leukocytes, interact with the trap mechanism. UC13 are, on average, larger and more rigid than leukocytes. It therefore stands to reason that UC13 can be captured at a lower trapping pressure than leukocytes. The next logical task is characterizing the relationship between trapping pressure and capture rate, called the **trapping curve**, for both leukocytes and UC13.

Variability in size and deformability between individual cells in a phenotype will cause the trapping curves for UC13 and leukocytes to be broad, and likely overlapping. The degree of overlap between the trapping curves of target and background phenotypes will determine how effective the resettable cell trap mechanism can be. If there is no overlap between target and background cell trapping curves, we expect the trap mechanism to achieve complete separation. If the trapping curves are identical, the trap mechanism will not be able to differentiate the cells at all. In the more likely scenario that the trapping curves partially overlap, we can construct a receiver-operator-curve and select a trapping pressure to meet the enrichment and retention required for the application. Figure 4-7 shows an example of what these curves might look like.

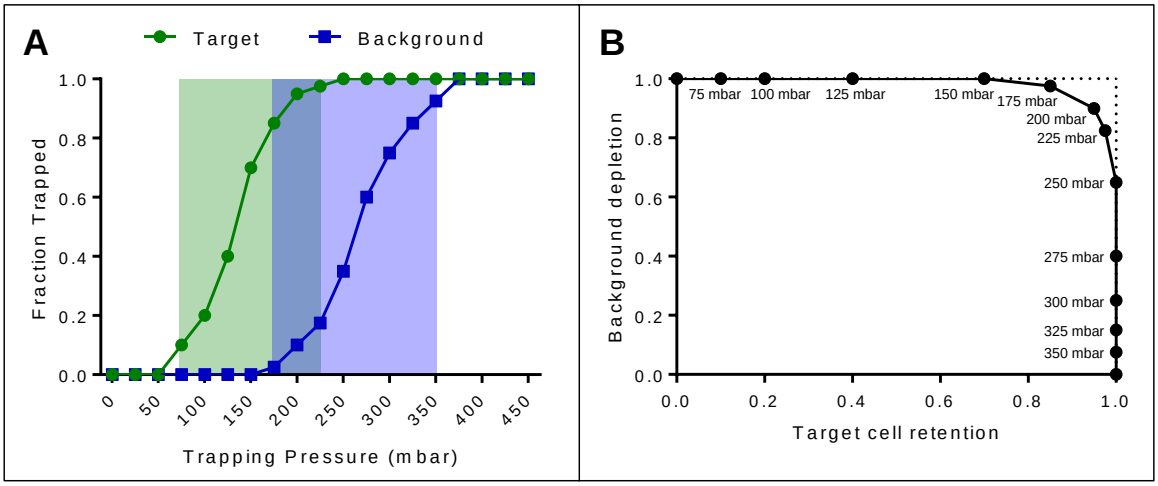

Figure 4-7 Example calibration curves for bulk cell separation. Data shown are not experimental results, and are intended for illustrative purposes only. A) Trapping curves for the two cell phenotypes to be separated. Smaller and more deformable leukocytes are expected to require greater pressure to trap than larger and more rigid UC13 cells. Shaded rectangles show the pressures that trap between 5% and 95% trapping for each phenotype. B) Receiver-operator curve for cell separation based on the calibration curves shown in A. No trapping pressure can produce 100% UC13 retention and 100% leukocyte depletion, so the user must select an appropriate performance point along the curve.

Most microfluidic cell separation devices retain approximately 95% of target cells. If the trapping curves of UC13 and leukocytes were found to overlap, we planned to select a trapping pressure to match this value. This would allow us to compare the enrichment achieved with the resettable cell trap to other separation mechanisms. For clarity in future sections, we will refer to the trapping pressure required to produce 95% retention as the **Critical Trapping Pressure** (CTP).

Unfortunately, three unexpected developments prevented the execution of this simple plan. First, we found that the correlation between trapping pressure and the actual flow channel cross-section varied considerably across devices. Second, we found that adhesion, and not physical constriction, was dominant in determining whether a leukocyte passing through a constricted trap was captured. Finally, we found that processing large volumes of analyte resulted in biofouling of the resettable cell traps. The first discovery made calibration a challenging process; the second had profound implications on the operational cycle and performance of the mechanism; and the third limited the operational lifetime of a device.

Chapter 5 - Three Wrinkles

5.1 Wrinkle 1: Cell trap calibration

The experiment plan laid out in the previous chapter called for the characterization of the trapping curve for UC13. Specifically, we wish to know the required trapping pressure to capture 95% of incident cells, a value called the critical trapping pressure (CTP). This approach is complicated by the single-use nature of microfluidic devices; the calibration must either be valid across many devices or be adjusted to compensate for variations between devices. Unfortunately, early experiments indicated that the CTP varied by up to 100 mbar between devices. This is unsurprising; the CTP depends on the device geometry and material properties of the diaphragm, both of which are difficult to control with precision during fabrication [**75**].

We investigated the consistency of our microfluidic fabrication process in an attempt to identify the source of the variations in the CTP across different devices. We specifically examined the parameters that control the stiffness of the trap diaphragm: the thickness and material properties of the diaphragm. As described in Figure 3-2, the diaphragm is formed by spin coating a mold with liquid PDMS. The spin coating process is inconsistent, producing diaphragms with a batch-to-batch thickness variation of up to 25% (Figure 5-1). These variations are likely caused by changes in the PDMS viscosity caused by partial curing and irregular heating during mixing and degassing. Compounding this problem are variations in the modulus of elasticity of PDMS caused by differences in curing time [**10**]. Regulating the fabrication process to produce consistent devices was deemed too difficult given the available equipment.

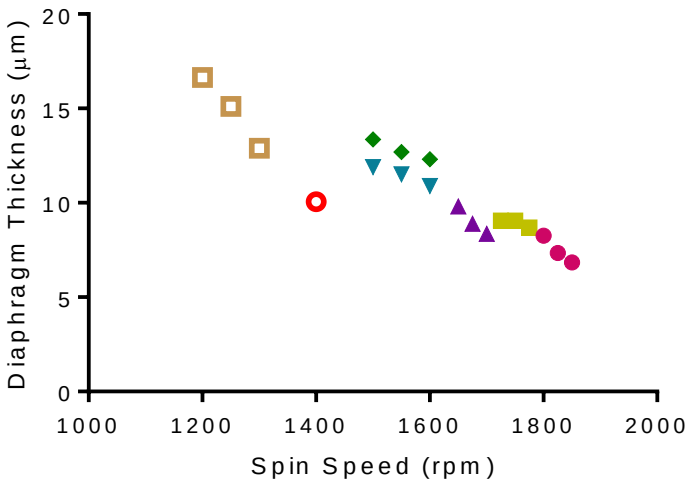

Figure 5-1 Diaphragm thickness as a function of spin speed. Data collected from the same batch of PDMS are shown with common symbols. While thickness decreases monotonically with increasing spin speed within a batch, substantial batch to batch variations are apparent. Thickness was measured using a non-contact optical profilometer.

Given our inability to fabricate devices with consistent geometry and material properties, we were faced with the challenge of determining the appropriate trapping pressure on a device-by-device basis. Rejected approaches for determining the CTP involved using a sensor to measure the channel cross-section for closed loop control or passing the mixed sample through the trap and increasing the trapping pressure until target cell capture is observed. Forming a closed loop system adds cost and complexity to an otherwise simple apparatus. Using the mixed sample to calibrate the trap before each experiment would be wasteful and impractical.

5.1.1 Indirect calibration

We devised an indirect calibration method as an alternative to direct closed loop control. Since the CTP for a given device depends on the stiffness of the diaphragm, any observations that inform the diaphragm stiffness may be useful for calibration. While it is difficult to measure the stiffness of the diaphragm in the cell traps, there are several other diaphragms on the chip used to form valves, all of which were deposited in the same fabrication step. A measurement of the stiffness of a non-trap diaphragm can therefore be used to calibrate the cell trap.

A simple, easy to measure value directly related to the diaphragm stiffness is the pressure required to actuate a valve [**76**]. The microfluidic device features two kinds of valves that may be useful towards this end. Standard valves are used to close rounded channels, and their actuation pressure is difficult to measure since the diaphragm gradually creeps up the rounded walls as it inflates (Figure 5-2). A more distinct transition occurs when inflating a sieve valve (Figure 5-3). The pressure required to inflate a sieve valve into the channel ceiling, called the sieve valve critical pressure (SVCP), can typically be made with ±5 mbar uncertainty by incrementally increasing the pressure until contact is observed. By measuring the SVCP, we gain a quantified measurement of the diaphragm stiffness for that individual device. The remaining challenge is using this measurement of stiffness to determine the critical trapping pressure for that device.

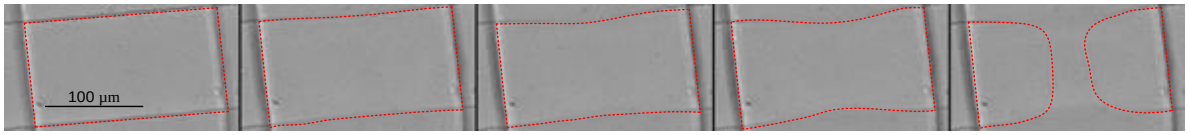

Figure 5-2 A push up valve closing a rounded channel. The image sequence shows valves at 0 mbar, 200 mbar, 260 mbar, 280 mbar, and 300 mbar differential pressures. The horizontal diaphragm edges, highlighted with a dotted line for clarity, creep inwards before meeting in the final frame to complete the seal.

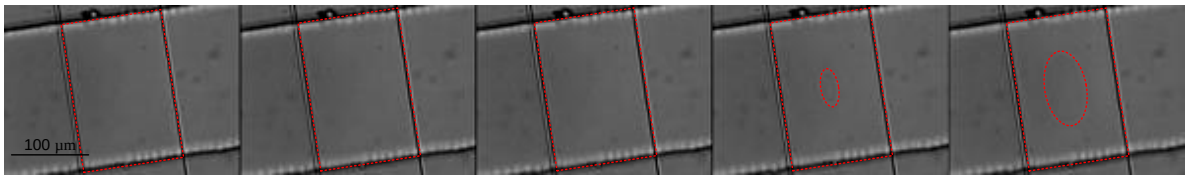

Figure 5-3 A push up valve closing a rectangular channel. The image sequence shows valves at 0 mbar, 60 mbar, 75 mbar, 80 mbar, and 150 mbar differential pressures. The diaphragm is in contact with the channel ceiling in the 80 mbar and 150 mbar frames, forming a visible ring, highlighted with a dotted line for clarity. This particular device has SVCP of 80 ± 5 mbar.

Using this technique to measure the diaphragm stiffness, we can determine the relationship between the SVCP and the trapping pressure required to capture cells. To quantify this relationship, we performed a series of calibration experiments on microfluidic devices with different SVCPs. In these experiments, we determined the UC13 trapping curve for that device by flowing UC13 through the cell trap at various trapping pressures and recorded the probability of capture for each trapping pressure (Figure 5-4A). We then measured the

SVCP for that particular device, and plotted it against the critical trapping pressure, producing a calibration curve (Figure 5-4B).

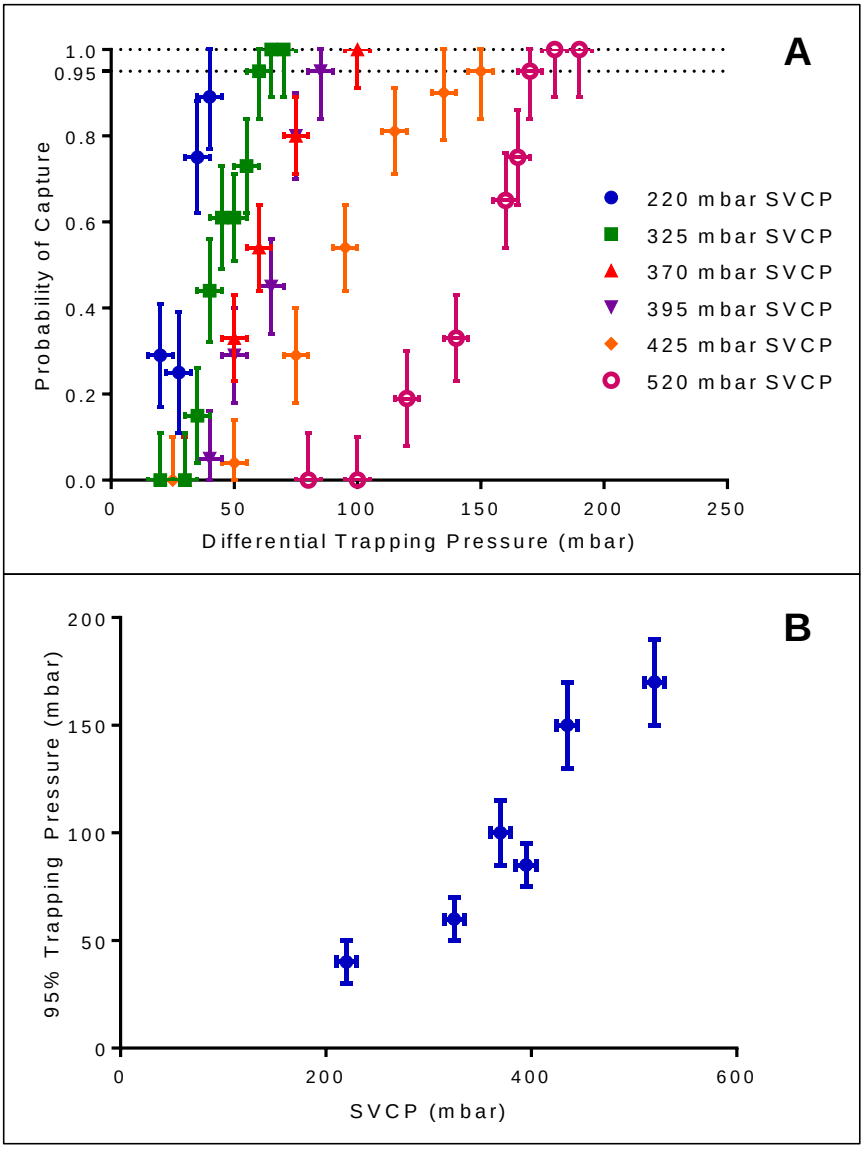

Figure 5-4 Calibration curves for the cell trap mechanism. A) Experimental results of UC13 trapping as a function of differential trapping pressure and the SVCP. Devices with lower SVCP have softer diaphragms and therefore require less pressure to capture UC13. B) A calibration curve shows the pressure required to trap 95% of UC13 as a function of the device SVCP based off the data in A.

The slope of the calibration curve in Figure 5-4B is positive as expected – the pressures required for both inflating the cell trap and inflating a sieve valve are related to the material properties of the PDMS diaphragm deposited in the spin coating step. To determine the appropriate trapping pressure for the cell separation experiments described in Chapter 6, a

microfluidic device was fabricated, its SVCP was measured, then CTP was determined by interpolating the curve of Figure 5-4B. While this approach to calibration is indirect and somewhat crude, the results presented in Chapter 6 will show that UC13 retention is consistently 85-95% as desired.

Interestingly, the transition between 0% and 100% trapping shown in Figure 5-4A occurs over a smaller pressure range when the SVCP is small than when it is large. Although a sharp transition is desirable, thin diaphragms have structural problems such as sticking and tearing that make them unreliable. As such, devices used in cell separation experiments were produced with thicker diaphragms in the 400-500 mbar SVCP range.

5.1.2 The effect of deformability on cell capture

Flowing cells may pass through constrictions smaller than the cells themselves if they are sufficiently able to deform. Deformation may be induced by any combination of normal forces from the channel walls, shear stresses from the surrounding fluid or normal (pressure) forces from the same. Hydrodynamic pressure forces on the cell play a minimal role in this device as a single trapped cell does not significantly occlude the channel, and normal forces from channel walls are determined by the cell size and channel cross-section, discussed previously. The impact of shear stress induced deformations is determined by the deformability of the cell and the magnitude of the shear.

Deformability is an intrinsic biomarker we hope to use to differentiate cell types, but the magnitude of the shear stress is a possible confounding variable. In the low Reynolds number flow regime, shear stress is linearly proportional to the fluid velocity (and therefore too, the volumetric flow rate) [**77**]. The practical implication of this scaling is illustrated in Figure 5-5 below.

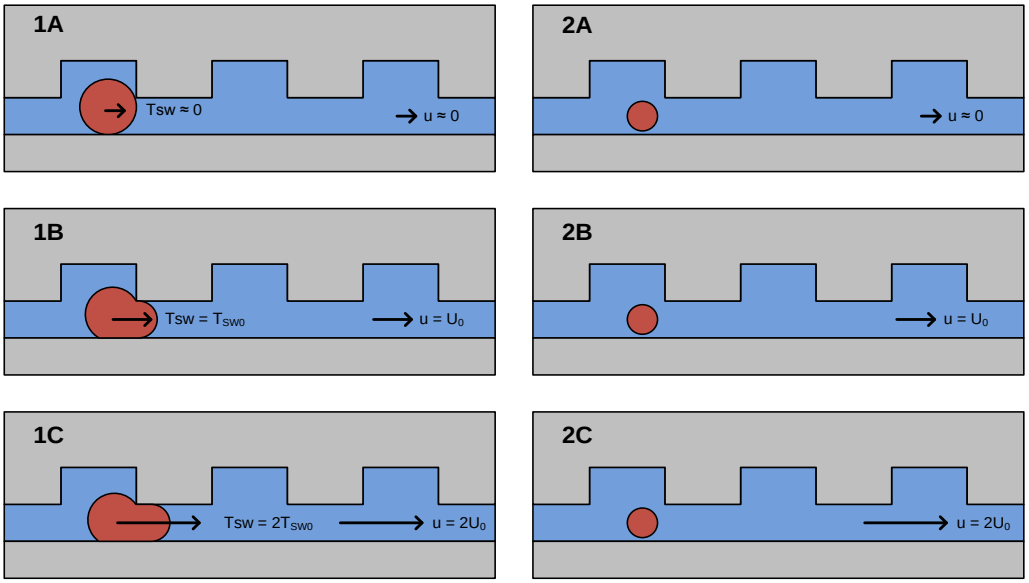

Figure 5-5 Size and deformability effects in cell trapping. Section views of large and small cells traveling down the constricted channel driven by fluid at various speeds. Large cells (1A-1C) are geometrically constrained by the cell trap be can be compressed through the constriction as the wall shear stresses increase with fluid speed. Sufficiently small cells (2A-2C) pass through the constriction independent of deformability or wall shear stresses. Labels indicate the linear relationship between fluid speed and wall shear stress.

In the limiting case of the fluid speed approaching zero, cells do not deform when trapped and the mechanism discriminates based on size alone. As flow speed, and therefore shear stress, increases, deformability plays a larger role in the fate of the cell. If we wish to test the device at different flow speeds, we must determine if deformability based effects are relevant over this domain and account for them if they are.

We conducted an experiment in which UC13 cells in dilute suspension were flowed into the trap at varying speeds. The trap geometry across these experiments was fixed by adjusting the control pressure to maintain a constant differential trapping pressure. A differential trapping pressure of 100 mbar was selected as this was found to be the minimum pressure required to capture 100% of UC-13 at slow speed in a previous experiment on the same device. Cells flowing through the trap were observed under a microscope and the fraction of cells captured at each flow speed was recorded. If cell deformability were a major parameter in the trapping outcome we would expect a decrease in trapping rate with increasing fluid speed as more cells squeeze through the constrictions. As shown in Figure 5-6, no decrease in trapping rate within experimental error was observed. This result confirms that, at least over the range of flow speeds examined, this device functions primarily as a size based sorter

for UC-13 cells. Trapping rate is a weak function of elasticity and a strong function of size over the normal operational parameters of the device.

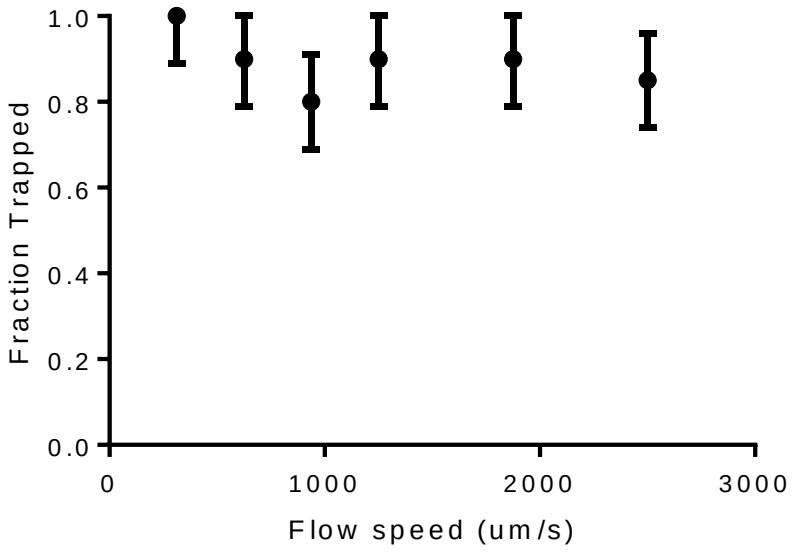

Figure 5-6 UC13 trapping rate at varying flow speeds. Cells flowed past a trap at different speeds while the channels cross-sectional shape was kept constant. Variation in trapping rate was within experimental error. N>20 for all data points.

5.2 Wrinkle 2: Leukocytes and the resettable cell trap

In Section 5.1, we characterized the way that UC13 interact with the resettable cell trap. The next step in the experiment plan was to characterize the way leukocytes interact with the trap, much in the same way. However, during attempts to characterize the relationship between trapping pressure and fraction of leukocytes trapped, it became apparent that leukocytes and UC13 interacted with the trap in different ways.

Unlike the physical constraints that determined the fate of UC13, the fate of leukocytes was primarily determined by the availability of open contact area with the trap walls. Evidence for this striking difference in behavior is shown in Figure 5-7 below. This composite image, taken during a cell separation experiment, shows the results of a mixture of leukocytes and UC13 flowing towards a constricted cell trap. UC13, too large and rigid to pass through the trap, are captured at the head of the cell trap. In contrast, leukocytes deposit throughout the length of the cell trap. The behavior of leukocytes cannot be explained by mechanical constraints alone. Since the cross-section of the constricted trap is largely uniform across its

length, it does not follow that a leukocyte would be able to successfully pass through the first ten recesses and then be captured in the eleventh due to mechanical effects alone. We must conclude that factors beyond mechanical effects determine the fate of a leukocyte passing through the trap.

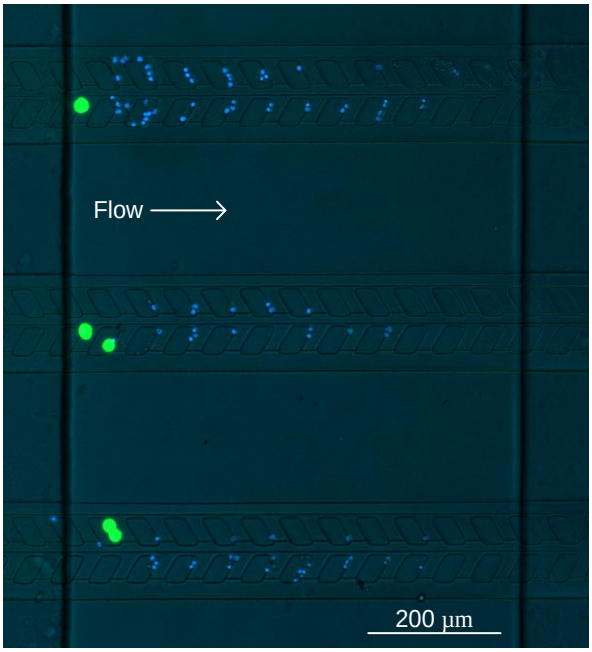

Figure 5-7 The trapping positions of leukocytes and UC13 in a constricted cell trap. UC13 are shown stained green, leukocytes are shown stained blue. UC13 are captured primarily due to physical constriction effects, and cannot flow past the beginning of the trap. Leukocytes are captured due to a combination of physical and non-specific adhesive effects, and therefore accumulate across the length of the trap wherever a large contact surface area is available.

The most plausible explanation for this behavior is non-specific adhesion of leukocytes to the channel walls. Non-specific adhesion to PDMS surfaces in microfluidic devices is a well-documented phenomenon [**62**] [**78**]. As leukocytes flow through the microchannels of the device, any adhesive forces must compete with the shear stress imparted by the flow to the cell surface. Since the number of potential binding sites is proportional to the contact area between the cell and PDMS walls, we expect cells to adhere most readily in areas with a large contact area available and a low flow rate. These conditions are present inside a constricted trap. The highly parallel nature of the traps causes the slowest flow speeds in the entire device, and cells passing through the trap can contact the PDMS walls on up to four surfaces simultaneously (front of recess, top of recess, side of recess, diaphragm). Consequently, we observe cells adhering in the constricted traps but not elsewhere in the

device. That many trapped leukocytes do not rejoin the flow even after the trap is relaxed is further evidence for adhesion based capture.

Interestingly, leukocytes were not found to clump to each other within the device, suggesting that the strength of leukocyte-PDMS adhesion is greater than that of leukocyte-leukocyte adhesion. As a result, once a suitable position in the cell trap became occupied by a captured leukocyte, subsequent leukocytes would simply flow past. When a suspension of leukocytes was flowed through a clean, constricted trap, the trap recesses would quickly capture leukocytes through adhesion. After these recesses became occupied, the capture rate of leukocytes dropped to near zero.

This model for how leukocytes interact with the cell trap confounded the calibration plan set out in Section 4.6. We could not measure the trapping rate of leukocytes as a function of trapping pressure, because absent a trapping pressure sufficient to nearly seal the trap completely, the fate of a leukocyte was determined almost entirely by whether or not a location for adhesion was available.

This wrinkle was not entirely unwelcome. It was encouraging to see that leukocytes will not be captured due to mechanical effects under trapping pressures to capture UC13. Further, the lack adhesion between leukocytes in the trap suggests that clogging due to an accumulation of background cells is not likely to be a failure mode in bulk cell separation. While some adhered leukocytes do rejoin the flow when the trap is relaxed, thereby contaminating the output and decreasing enrichment, these observations suggest that a small, fixed number of leukocytes will be released each cycle. These factors suggest that resettable cell trap may perform very well in applications where target cells are rare, as fewer total cycles will be required to process the entire sample.

5.3 Wrinkle 3: Fouling

The resettable cell trap was designed to separate target cells from a heterogeneous suspension of cells. In practice, however, it is difficult or impossible to produce a sample for analysis that consists solely of whole cells and fluid. Other substances may be present in the sample, such as proteins, non-biological debris, and lysate. Such is the case for the analyte prepared for the experiments of Chapter 6. While these noncellular components are almost

exclusively smaller than the cells themselves, their presence caused fouling (clogging due to the accumulation of unwanted material) in the resettable cell traps during relatively long experiments. Fouling, an example of which is shown in Figure 5-8 below, was the third wrinkle in the development of this device.

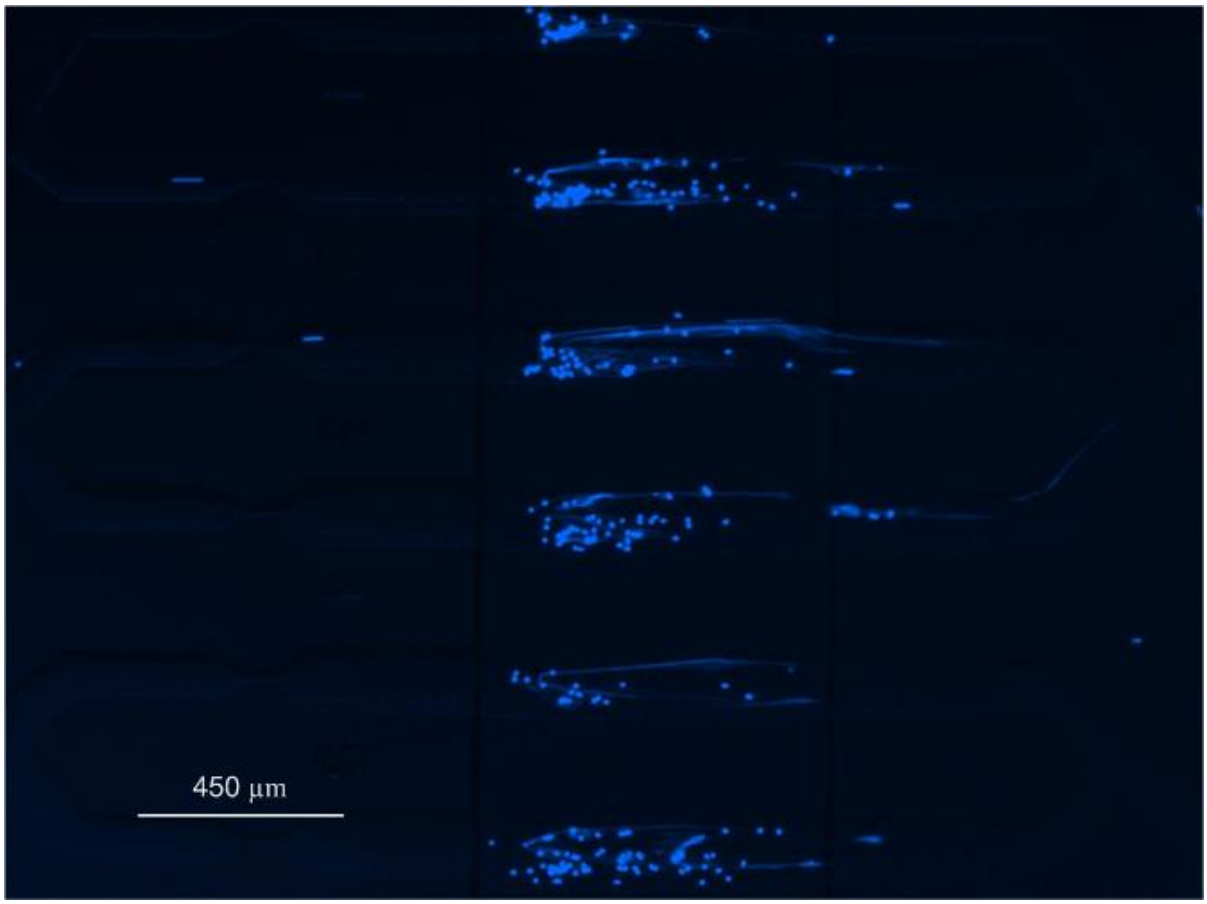

Figure 5-8 Fouling. This fluorescence image shows stained leukocytes (bright circles) in several cell traps with long strings of noncellular material attached. This image was taken while flow was ongoing. The shear stress on the fouling material induced by the flow caused it to stretch out.

The noncellular material fouled the cell traps not because it was large, but because it was adhesive. When large quantities of analyte were flowed through the cell trap, the noncellular material would slowly build up within the trap over time. Eventually, the accumulation would grow large enough to ensnare passing by cells, at which point the trap became irreparably fouled and the experiment could not continue. The high pressure purge did not eliminate the fouling material.

Definitively identifying the noncellular components that caused fouling proved to be a challenging task. To narrow the possibilities we conducted a series of controlled cell separation experiments to characterize the fouling material and process. Below is a list of those characteristics:

- Fouling occurs if leukocytes are the only cell type in the analyte
- Fouling does not occur if UC13 are the only cell type in the analyte
- Fouling occurs even when using sterile fluidics
- Accumulation of fouling material is approximately proportional to the number of leukocytes processed
- The fouling material is elastic, deforming under flow and recoiling when the flow is removed (Figure 5-8)
- The fouling material fluoresces weakly when stained with Hoechst
- The fouling material can be seen in the bulk analyte, that is, before the sample is loaded into the microfluidic device
- Fouling occurs faster if the analyte is left for over 1 hour at room temperature before processing
- Fouling is unmitigated by the addition of 5mM edetic acid (EDTA), an anticoagulant, to the analyte prior to cell separation

This issue remains without a satisfactory solution. To circumvent fouling problems, the cell separation experiments described in the following chapter involved processing no more than 500,000 cells. Several attempted experiments failed due to fouling, and are not included in the experimental results.

Chapter 6 – Results

6.1 Introduction

We conducted a series of cell separation experiments to quantify the performance of the cell separation device according to the metrics introduced in Section 1.3.3. Specifically, we conducted experiments to measure the resettable cell traps ability to resolve polystyrene microspheres of different sizes; experiments to optimize the device for the separation of UC13 and leukocytes, and experiments to characterize the enrichment and retention of the device under those optimal conditions. This chapter details the results of these experiments.

6.2 Separation Resolution

The ability of a particle to transit through the cell trap is determined by the cross-sectional opening between the diaphragm and the channel ceiling. The size of this opening can be adjusted changing the trapping pressure, allowing the selectively capture of particles greater than a certain diameter. To characterize the smallest difference in particle size that the resettable cell trap can resolve, we measured the probability of capture for monodisperse microparticles as a function of the trapping pressure. The tested microparticles (Bangs Labs, Fishers, IN) included diameters of 6.4 ± 0.3 μm, 7.3 ± 0.4 μm, 9.5 ± 0.3 μm, and 10.1 ± 0.4 μm, selected to mimic the cross-sectional width of deformed cells. The results of these experiments are shown in Figure 6-1. For each particle size, the transition between no trapping and complete trapping occurs over 25-50 mbar of pressure (shown as shaded regions). More importantly, there is little to no overlap in the transition regions between different particle diameters, which indicate the resettable cell trap mechanism is capable of resolving particles with <1 μm resolution.

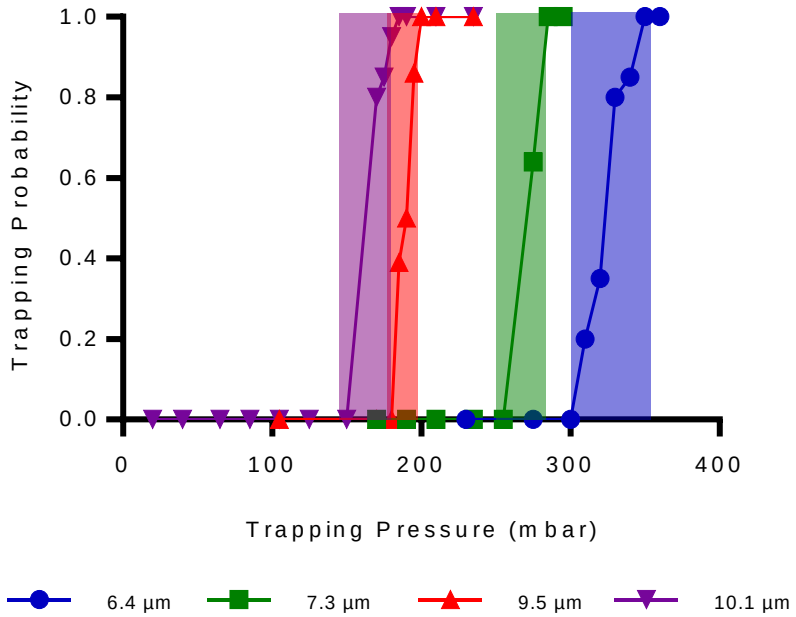

Figure 6-1 Measuring the resolution of the resettable cell trap. The probability of capture for microparticles of varying size is shown as a function of trapping pressure. Larger particles require a greater pressure to be trapped. Shaded rectangles show the pressures that trap between 5% and 95% trapping for each microparticle size.

6.3 Performance under varying parameters

We conducted a number of experiments to investigate the efficacy of the cell separation device under various conditions. Specifically, we aimed to investigate the effects of flow speed, concentration and doping ratio on the device performance. Flow speed and concentration are important parameters because they determine the device throughput. Doping ratio is relevant to CTC separation because different pre-processing steps are required to achieve different doping ratios, and it is desirable to eliminate as many pre-processing steps as possible in the name of time, expense, and CTC retention. The considerable time requirements for each experiment made a full exploration of the 3D parameter space infeasible. As an alternative, we selected a base flow speed, doping ratio, and concentration, then each variable was changed independently from that base set. The base experiment takes a sample of 100 leukocytes/UC13, a concentration of 10^6 cells/mL, and a base flow speed of 500 µm/s through the trap. Each experiment was terminated after no fewer than 100 UC13 had been processed, except the two experiments conducted at

doping ratios of 2500:1 and 5000:1, which were terminated after no fewer than 50 UC13. The results of the parametric sweep are shown in Figure 6-2 below.

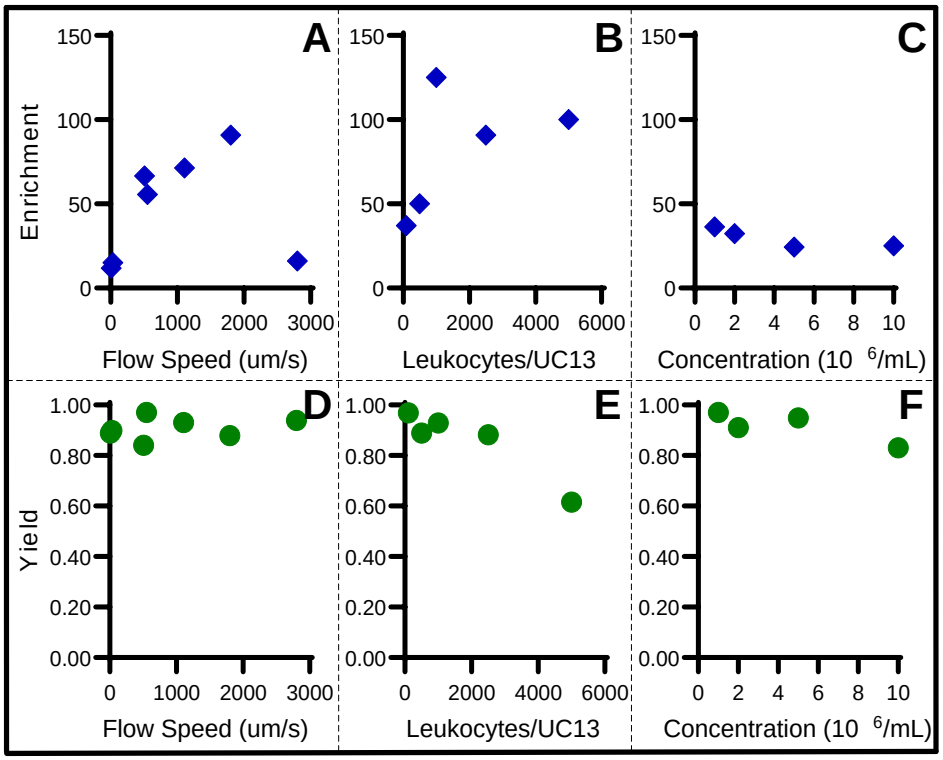

Figure 6-2 Results of cell separation experiments. Each data point represents an individual experiment in which 50,000 to 250,000 cells were processed. A-F) Results of independently varying concentration, relative cell concentration, and flow speed from a base parameter set of 500 µm/s, 100 leukocytes/UC13, and 10^6 cells/mL.

The cell separation device was able to obtain retention of 85-95% with an enrichment of 50-150x over most experiments. Figure 6-2A shows a strong correlation between flow speed and enrichment, likely due to the decreased incidence of adhesion of leukocytes to the trap wall at higher speed. However, beyond a speed of approximately 2000 µm/s, we observed a dramatic increase in the rate of leukocyte adhesion, likely attributable to shear induced leukocyte activation. Figure 6-2B shows another strong correlation between enrichment and doping ratio. The suspected origin of this relationship is given by the adhesive behavior of leukocytes in the cell trap described in Section 5.2. We observed that an approximately fixed number of leukocytes would release from the trap walls during each collection phase, regardless of the length of the filtration phase previous. Since collections are only required when target cells threaten to clog the trap, performance should improve when target cells,

and therefore collection phases, are more rare. Figure 6-2C shows little correlation between performance and analyte concentration over the range of concentrations tested. Finally, Figure 6-2(D-F) indicates that the resettable cell trap's ability to capture cancer cells is not strongly dependent on variations in flow speed, doping ratio, and concentration.

6.4 Repeatability experiments

Based on the parametric study of the previous section, we selected a set of operating conditions expected to optimize performance: a flow speed of 2000 µm/s, a relative concentration of 1000 leukocytes per UC13, and a total concentration of $2 \cdot 10^6$ cells/mL. To investigate the repeatability of the device performance, we conducted four cell separation experiments at these conditions.

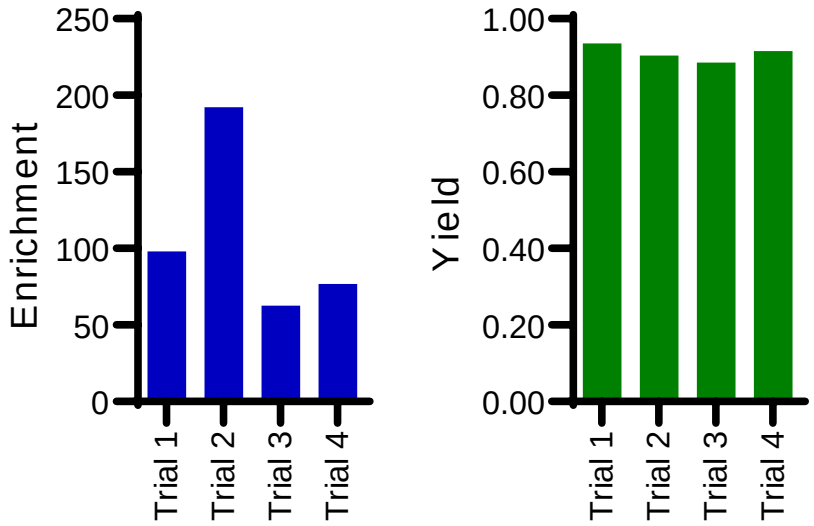

Figure 6-3 Performance of the cell separation device over repeated experiments. The cell sample was prepared at a concentration of $2 \cdot 10^6$ cells/mL and a relative cell concentration of 1000 leukocytes/UC13. The centerline flow speed through the traps was approximately 2000 µm/s.

The repeated experiments show consistent performance, with an average enrichment of 108x and retention of 92%. The throughput across these experiments was approximately 225 µL/hour, or 450,000 cells/hour.

6.5 Serial Enrichment

One of the key results of our initial cell separation experiments is the realization that while cancer cells are caught in the cell trap because of mechanical constraint, leukocytes are

captured primarily because of non-specific adhesion. This result suggests that repeatedly filtering the sample through multiple traps could improve enrichment, since adhesion is a more stochastic process than physical filtration. To test this hypothesis, we processed a sample with an initial concentration of $2 \cdot 10^6$ leukocytes/mL and UC13 cells doped in at a ratio of 1:1000. After each pass through the cell separation device, we imaged the waste and collection outlets to quantify the yield and enrichment for that individual step. We then pipetted the contents of the collection outlet back into the inlet, emptied the waste reservoir, and filtered the sample with the resettable cell trap once more. This process was repeated three times in total. The results of each individual filtration step and the combined results are shown in Figure 6-4 below.

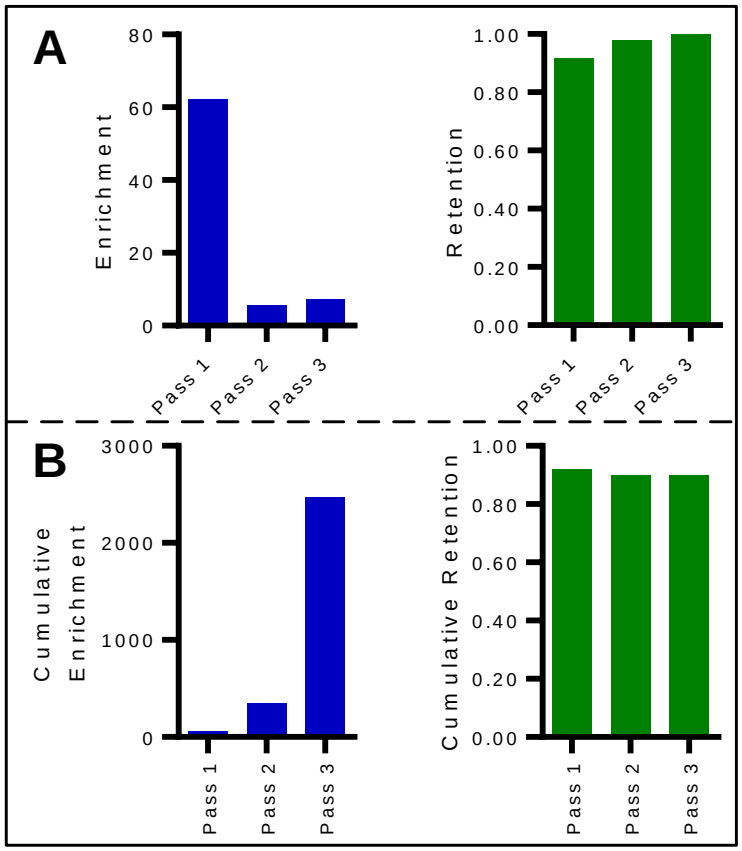

Figure 6-4 Results of a 3-step cell separation experiment. Enrichment and retention are shown for individual steps (A) and as a cumulative effect (B)

As shown in Figure 6-4A, while the first filtration pass provides the greatest enrichment of the individual passes, the second and third pass provide substantial additional enrichment.

The compounded effect of all three steps (Figure 6-4B), is a 2470x enrichment, over twenty times greater than what was achieved in a single step in the previous section. Importantly, loss of target cells occurred almost exclusively in the first pass, which that the total retention was still approximately 90%. These results validate the idea that leukocytes are captured in the resettable cell trap because of non-specific adhesion rather than mechanical constraint, and suggest that the level of enrichment could be improved even further with additional filtration passes. This capability is being integrated in future versions of this device.

6.6 Viability

We measured the viability of captured cells using a live/dead viability assay kit that tests cell membrane integrity. Briefly, we incubated UC13 cells in a 2 µM solution of calcein AM (Invitrogen) and a 1 µM solution of ethidium homodimer-1 (Invitrogen) for 30 minutes. We then passed the UC13 suspension through the cell separation device and collected them in an outlet reservoir, where they were counted under the microscope with appropriate fluorescent filters. Passing UC13 through the cell separation device resulted in a decrease in viability of less than 0.5%.

Chapter 7 – Discussion and Conclusion

7.1 Size versus deformability based separation

Cell separation techniques that discriminate based on size alone are attractive because of their operational simplicity and their high throughput. This approach, however, can be ineffective in applications where target and background cells are of similar size. As a filtration based mechanism, the resettable cell trap discriminates based on a combination of size and deformability and is likely to offer superior performance in these applications. We chose to test the resettable cell trap on a mixture of UC13 and leukocytes specifically because they have overlapping size distributions (Figure 7-1A) but widely varying deformability (Figure 7-1B). Due to this overlap, it is not possible to completely separate a mixture of the two phenotypes based off size alone. Selecting all the cells in the mixture greater than 20 μm in diameter would eliminate all leukocytes, but would also eliminate the vast majority of UC13. Selecting all cells greater than 10 μm would ensure all UC13 were retained, but a significant fraction of leukocytes would contaminate the output. Figure 7-1 C shows the limits in specificity possible for a purely size based separation using a range of threshold cell sizes – the performance of any purely size based approach must lie on or within the blue curve. The resettable cell trap mechanism discriminates based on both size and rigidity, and its performance exceeds what is possible through size only discrimination.

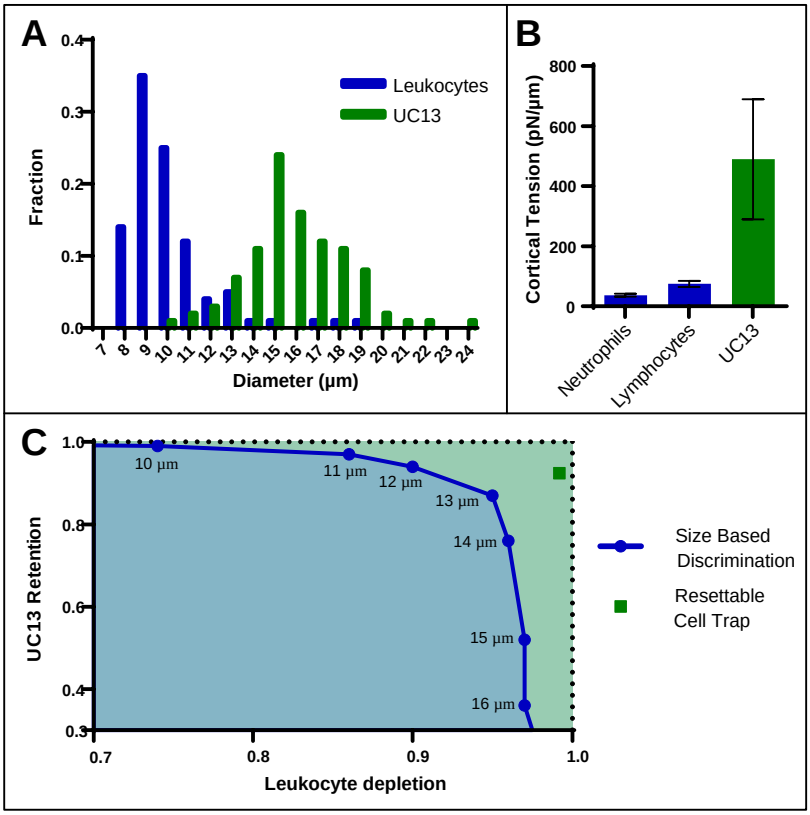

Figure 7-1: Physical properties of leukocytes and UC13. A) Size distribution of UC13 and leukocytes. N=100 for each population. There is substantial size overlap between the two phenotypes in the 11-15 µm range. B) Deformability of neutrophils, lymphocytes and UC13 as measured by microfluidic micropipette aspiration. C) A receiver-operator-curve for a purely size based separation device shows target cell retention and background cell depletion for different threshold diameters. The performance of any separation mechanism based exclusively off cell size is restricted to the blue shaded area due to the overlapping size distributions of UC13 and leukocytes. The performance of our mechanism lies outside the RO, indicating that the mechanism discriminates based off more than size alone.

7.2 Anti-clogging features

Many label-free cell separation devices employ deformability as a secondary discriminating property, typically employing a micro-scale filter as the separation mechanism. The main limitation of filtration based techniques is that over time the filters will partially or fully clog. This problem can be circumvented by simply using a new filter; however parallelization quickly consumes the available footprint of the device and leads to low total throughput. Our mechanism avoids clogging problems altogether because it can be purged and reset, allowing sustained and reliable operation. These merits are best illustrated by example. Figure 7-2 below shows the accumulation of cells in two traps: one is kept in the constricted state and never emptied, while the other is periodically purged and reset.

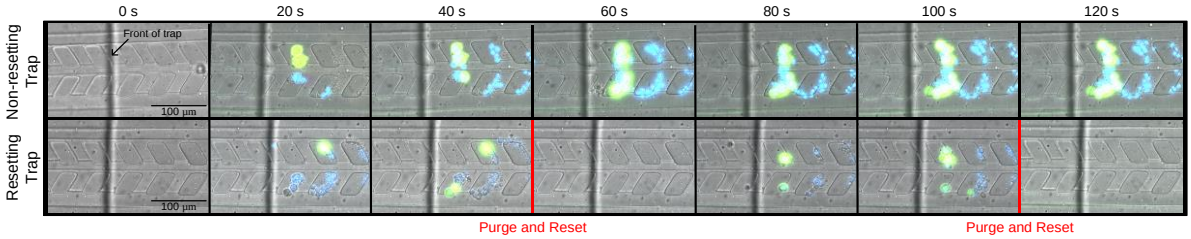

Figure 7-2: Comparison of resetting and non-resetting trap mechanisms. Each frame is a composite of bright field, blue fluorescence and green fluorescence images. Target UC13 cells fluoresce green, background leukocytes fluoresce blue. The non-resetting trap functions properly through the first minute, after which enough cells have accumulated in the cavities to clog the channel. The resetting trap is purged every 60 seconds and remains clean through several cycles. Images were taken in greyscale and given false color to reflect their original fluorescence.

In this example the non-resettable filter is fouled after just two minutes of operation. Trapped cells effectively become part of the filter geometry and obstruct the channel - Figure 7-2 shows leukocytes accumulating at the trap head only after a number of UC13 enter the trap and decrease the available channel cross section. Our mechanism can quickly be purged and reset, allowing continuous operation without a decrease in the selectivity of the trap. Additionally, the ability to release captured cells allows for their analysis and collection downstream. Other micropore filtration techniques do not accommodate the release of captured cells [**25**] [**55**], requiring any post processing to be done on-chip.

7.3 Performance comparison

This thesis concludes with a brief, quantitative comparison between the resettable cell trap and competing label-free cell separation techniques. This comparison is not meant to be exhaustive. In most cases, differences in methodology between publications limit the validity of direct comparisons. Specifically, the different target and background cell lines used in proof-of-concept tests confounds a direct comparison. Consequentially, we mean only to provide an order-of-magnitude sense of the enrichment, yield, and throughput for each family of label-free cell separation mechanisms. The enrichment and retention of label-free techniques are compared in Table 7-1 below.

Table 7-1 Comparing the enrichment and yield of label-free cell separation techniques. Many of these values are inferences based off data in the original publications.

Technique	Paper	Enrichment	Retention	Target Cell
3D microfilter	Zheng [**25**]	1000	86 %	LNCaP, MCF-7
2D microfilter	Zheng [**55**]	N/A	88%	LNCaP
DLD	Liu [**42**]	40	99%	MCF7
Filter	Mohamed [**23**]	N/A	N/A	Neuro-blastoma
Inertial	Di Carlo [**24**]	5-6	10-20%	MCF-7, HeLa
Ratchet	McFaul [**26**]	Unknown	98%	MLC
Cell trap		108 (1 pass) 2470 (3 passes)	92% (1 pass) 90% (3 passes)	UC13

With respect to enrichment and retention, the resettable cell trap fares better than the DLD and inertial techniques, and comparably to other filtration techniques.

Comparing the throughput of different devices is slightly more involved than comparing enrichment and yield. The ease of parallelization of microfluidic mechanisms confounds throughput measurements – 100 slow mechanisms in parallel may produce a similar total throughput to a single fast mechanism. Since the limits of parallelization are set by the footprint available for fabrication, a fair metric for speed of operation is not cells per hour, but cells per hour per unit area. Our prototype cell separation device contains 32 parallel channels that together process approximately 450,000 cells/hour. The footprint for the 32 channel device is 4.5 cm^2 with only 0.7 cm^2 devoted to the cell traps and bifurcation network, equating to an area normalized throughput of approximately $6.0 \cdot 10^5$ cells/$cm^2 \cdot$hour. This throughput is compared to other techniques in Table 7-2 below.

Table 7-2 Comparing the throughput of label-free cell separation techniques. Footprint data is largely unreported in publications and was approximated using photographs of the microfluidic devices.

Technique	Paper	Footprint (cm^2)	Throughput (nucleated cells/hr)	Throughput (nucleated cells/cm^2hr)
3D microfilter	Zheng [**25**]	1	$6.0*10^7$	$6.0*10^7$
2D microfilter	Zheng [**55**]	N/A	N/A	$1.0*10^6$
DLD	Liu [**42**]	N/A	2 mL whole blood/hr	N/A
Filter	Mohamed [**23**]	24	0.1 mL whole blood/hr	$4.2*10^4$
Inertial	Di Carlo [**24**]	N/A	$2.7*10^7$	N/A
Ratchet	McFaul [**26**]	1	$9*10^3$	$9.3*10^3$
Cell trap		4.5	$4.5*10^5$	$6.0*10^5$

The throughput of the resettable cell trap compares favorably to other label-free cell separation techniques, exceeding the throughput of previous micropore filtration techniques by a factor of approximately 10. Ultra-fast cell separation methods with throughputs exceeding 10^7 cells/cm^2·hour have been achieved using inertial microfluidics, however these methods typically provide considerably lower enrichment than filtration based techniques.

7.4 Future Work

In this thesis we have presented proof-of-concept for the resettable cell trap, representing a foundation for a variety of exciting future work. We would like to build on this success, addressing the shortcomings of the device and moving towards applying the resettable cell trap for biological and medical purposes. To this end, changes to several design elements of the device should be explored. We would like to implement the multistage filtration described in Section 6.5 using strictly microfluidic elements, eliminating the need for manual pipetting and the associated potential for cell loss. We would further like to produce a heavily parallelized prototype device to maximize device throughput. Experimentally, the most pressing task is resolving the biofouling problem, either through a sample preparation technique that prevents its production, or through a mechanism to remove or destroy any fouling material that accumulates in the device. Once the fouling issue is resolved, we look forward to real-world applications, testing the resettable cell trap's ability to separate circulating tumor cells from patient blood in clinical trials.

7.5 Conclusion

In this thesis, we discussed the implementation of the resettable cell trap mechanism in a microfluidic device capable of separating bulk analyte. We designed an operational cycle for continuous cell separation, implemented and characterized supporting fluidic elements to improve performance, and characterized the behavior of leukocytes and a model cancer cell line within the resettable cell trap. We optimized the operating conditions of the device and measured its performance at these optimized conditions. The device offers highly specific separation without compromised throughput, and allows for the easy collection of target cells. We hope this device will be employed for the separation of rare circulating tumor cells from peripheral blood in the future.

Works Cited

[1] Giovanna Vona et al., "Isolation by size of epithelial tumor cells: A new method for the immunomorphological and molecular characterization of circulating tumor cells," *American Journal of Pathology*, vol. 156, no. 1, pp. 56-63, 2000.

[2] S. H. Seal, "A sieve for the isolation of cancer cells and other large cells from the blood," *Cancer*, vol. 17, no. 5, pp. 637-642, 1964.

[3] C. G. Rao et al., "Expression of epithelial cell adhesion molecule in carcinoma cells present in blood and primary metastatic tumors," *International Journal of Oncology*, vol. 27, no. 1, pp. 49-57, 2005.

[4] Bernardina van der Gun et al., "EpCAM in carcinogenesis: the good, the bad or the ugly," *Carcinogenesis*, vol. 31, no. 11, pp. 1913-1921, 2010.

[5] Ann Chambers, Alan Groom, and Ian MacDonald, "Metastasis: Dissemination and growth of cancer cells in metastatic sites," *Nature Reviews Cancer*, vol. 2, pp. 563-572, 2002.

[6] Peter Gravesen, Jens Branebjerg, and Ole Sondergard Jensen, "Microfluidics - a review," *J. Micromechanics and Microengineering*, vol. 3, no. 4, pp. 168-182, 1993.

[7] E. Bassous, H. H. Taub, and L. Kuhn, "Ink jet printing nozzle arrays etched in silicon," *Applied Physics Letters*, vol. 31, no. 2, pp. 135-137, 1977.

[8] Younan Xia and George M. Whitesides, "Soft Lithography," *Annual reviews of materials science*, vol. 28, pp. 153-184, 1998.

[9] E Berthier, E W Young, and D Beebe, "Engineers are from PDMS-land, biologists are from polystyrenia," *Lab on a Chip*, vol. 12, no. 7, pp. 1224-1237, April 2012.

[10] Marc A Unger, Hou-Pu Chou, Todd Thorsen, Axel Scherer, and Stephen R Quake, "Monolithic microfabricated valves and pumps by multilayer soft lithography," *Science*, vol. 288, pp. 113-116, 2000.

[11] Todd Thorsen, Sebastian Maerkl, and Stephen Quake, "Microfluidic Large-Scale Integration," *Science*, vol. 298, pp. 580-584, October 2002.

[12] F. Balagadde, L. You, C. Hansen, F. Arnold, and S. Quake, "Long-term monitoring of bacteria undergoing programmed population control in a microchemostat," *Science*, vol. 309, pp. 137-140, July 2005.

[13] Massimo Cristofanilli et al., "Circulating tumor cells, disease progression, and survival in metastatic breast cancer," *The New England journal of Medicine*, vol. 351, pp. 781-791, August 2004.

[14] Daniel C. Danila, Glenn Heller, and Gretchen A. Gignac, "Circulating tumor cell number and prognosis in progressive castration-resistant prostate cancer," *Clinical Cancer Research*, vol. 13, no. 23, pp. 7053-7058, December 2007.

[15] Sunitha Nagrath et al., "Isolation of rare circulating tumor cells in cancer patients by microchip technology," *Nature*, vol. 450, pp. 1235-1239, 2007.

[16] Min Yu, Shannon Stott, Mehmet Toner, Shyamala Maheswaran, and Daniel A. Haber, "Circulating tumor cells: approaches to isolation and characterization," *Journal of Cell Biology*, vol. 192, no. 3, pp. 373-382, February 2011.

[17] F. A.W. Coumans, C. J.M. Doggen, G. Attard, J. S. de Bono, and L. W.M.M. Terstappen, "All circulating EpCAM+CK+CD45- objects predict overall survival in castration-resistant prostate cancer," *Annals of Oncology*, vol. 21, no. 9, pp. 1851-1857,

February 2010.

[18] Giovanna Vona et al., "Enrichment, immunomorphological and genetic characterization of fetal cells circulating in maternal blood," *American Journal of Pathology*, vol. 160, no. 1, pp. 51-58, January 2002.

[19] Mehmet Toner and Daniel Irimia, "Blood-on-a-chip," *Annu. Rev. Biomed. Eng.*, vol. 7, pp. 77-103, 2005.

[20] S. Kern, H. Eichler, J. Stoeve, H. Klueter, and K. Bieback, "Comparative analysis of mesenchymal stem cells from bone marrow, umbilical cord blood or adipose tissue," *Stem Cells*, vol. 24, no. 5, pp. 1294-1301, May 2006.

[21] Oscar K Lee et al., "Isolation of multipotent mesenchymal stem cells from umbilical cord blood," *Blood*, vol. 103, no. 5, pp. 1669-1675, March 2004.

[22] Daniel R Gossett et al., "Label-free cell separation and sorting in microfluidic systems," *Anal. Bioanal. Chem.*, vol. 397, no. 8, pp. 3249-3267, 2010.

[23] Hisham Mohamed, Megan Murray, James N. Turner, and Michele Caggana, "Isolation of tumor cells using size and deformation," *Journal of Chromatography A*, vol. 1216, pp. 8289-8295, 2009.

[24] Soojung Claire Hur, Albert J. Mach, and Dino Di Carlo, "High-throughput size-based rare cell enrichment using microscale vortices," *Biomicrofluidics*, vol. 5, pp. 0222061-10, 2011.

[25] Siyang Zheng et al., "3D microfilter device for viable circulating tumor cell (CTC) enrichment from blood," *Biomedical Microdevices*, vol. 13, pp. 203-213, 2011.

[26] Sarah M. McFaul, Bill K. Lin, and Hongshen Ma, "Cell separation based on size and

deformability using microfluidic funnel ratchets," *Lab on a Chip*, vol. 12, pp. 2369-2376, 2012.

[27] Ralf Gertler et al., "Detection of circulating tumor cells in blood using an optimized density gradient centrifugation," *Molecular Staging of Cancer*, vol. 162, pp. 149-155, 2003.

[28] Howard M. Shapiro, *Practical Flow Cytometry*, 4th ed. Hoboken, USA: John Wiley & Sons, 2003.

[29] Alison L. Allan et al., "Detection and quantification of circulating tumor cells in mouse models of human breast cancer using immunomagnetic enrichment and multiparameter flow cytometry," *Cytometry A*, vol. 65A, pp. 4-14, April 2005.

[30] Oscar Lara, Tong Xiaodong, Maciej Zborowski, and Jeffrey J. Chalmers, "Enrichment of rare cancer cells through depletion of normal cells using density and flow-through, immunomagnetic cell separation," *Experimental Hematology*, vol. 32, pp. 891-904, 2004.

[31] Sabine Riethdorf et al., "Detection of Circulating Tumor Cells in Peripheral Blood of Patients with Metastatic Breast Cancer: A Validation Study of the CellSearch System," *Clin Cancer Res*, vol. 13, pp. 920-928, 2007.

[32] S. J. Cohen et al., "Relationship of Circulating Tumor Cells to Tumor Response, Progression-Free Survival, and Overall Survival in Patients With Metastatic Colorectal Cancer," *Journal of Clinical Oncology*, vol. 26, no. 19, pp. 3213-3221, July 2008.

[33] J. S. de Bono et al., "Circulating tumor cells predict survival benefit from treatment in metastatic castration-resistant prostate cancer," *Clinical cancer research*, vol. 14, no. 19,

pp. 6302-6309, October 2008.

[34] Ali Asgar S. Bhagat et al., "Microfluidics for cell separation," *Medical and biological engineering and computing*, vol. 48, pp. 999-1014, October 2010.

[35] Wenli Zhou, Qian Wu, Huanan Jiang, and Ming Zhu, "Design of micropillar array for cell capture," in *Nano/Micro Engineered and Molecular Systems*, Kaohsiung, 2011, pp. 1028-1031.

[36] Jason Gleghorn et al., "Capture of circulating tumor cells from whole blood of prostate cancer patients using geometrically enhanced differential immunocapture (GEDI) and a prostate-specific antibody," *Lab on a Chip*, vol. 10, pp. 27-29, November 2009.

[37] Masumi Yamada, Megumi Nakashima, and Minoru Seki, "Pinched flow fractionation: continuous size separation ofparticles utilizing a laminar flow profile in a pinched microchannel," *Anal. Chem*, vol. 76, pp. 5464-5471, August 2004.

[38] JA Davis et al., "Deterministic hydrodynamics: taking blood apart," *Proc. Natl. Acad. Sci.*, vol. 103, pp. 14779-14784, 2006.

[39] D W Inglis, J A Davis, R H Austin, and J C Sturm, "Critical particle size for fractionation by deterministic lateral displacement," *Lab on a Chip*, vol. 6, pp. 655-658, May 2006.

[40] Lotien Richard Huang, Edward C. Cox, Robert H. Austin, and James C. Sturm, "Continuous particle separation through deterministic lateral displacement," *Science*, vol. 304, pp. 987-990, May 2004.

[41] R Huang et al., "A microfluidics approach for the isolation of nucleated red blood cells (NRBCs) from the peripheral blood of pregnant women," *Prenatal Diagnostics*, vol. 28,

no. 10, pp. 892-899, October 2008.

[42] Zongbin Liu et al., "Rapid isolation of cancer cells using microfluidic deterministic lateral displacement structure," *Biomircofluidics*, vol. 7, p. 011801, 2013.

[43] Dino Di Carlo, "Inertial Microfluidics," *Lab on a Chip*, vol. 9, pp. 3038-3046, September 2009.

[44] Sathyakumar S. Kuntaegowdanahalli, Ali Asgar S. Bhagat, Girish Kumar, and Ian Papautsky, "Inertial microfluidics for continuous particle separation in spiral microchannels," *Lab on a Chip*, vol. 9, pp. 2973-2980, 2009.

[45] Ali Asgar S. Bhagat, Sathyakumar S. Kuntaegowdanahalli, and Ian Papautsky, "Continuous particle separation in spiral microchannels using dean flows and differential migration," *Lab on a Chip*, vol. 8, no. 11, pp. 1906-1914, September 2008.

[46] H. W. Hou et al., "Isolation and retrieval of circulating tumor cells using centrifugal forces," *Scientific Reports*, vol. 3, p. 1259, February 2013.

[47] Evgeny S. Asmolov, "The inertial lift on a spherical particle in a plane Poiseuille flow at large channel Reynolds number," *J. Fluid Mech*, vol. 381, pp. 63-87, 1999.

[48] W. R. Dean and J. M. Hurst, "Note on the motion of fluid in a curved pipe," *Mathematika*, vol. 6, no. 1, pp. 77-85, June 1959.

[49] Jae-Sung Park and Hyo-Il Jung, "Multiorifice flow fractionation: Continuous size-based separation of microspheres using a series of contraction/expansion microchannels," *Analytical Chemistry*, vol. 81, pp. 8280-8288, 2009.

[50] Albert J Mach, Jae Hyun Kim, Armin Arshi, Soojung Claire Hur, and Dino Di Carlo, "Automated cellular sample preparation using a Centrifuge-on-a-Chip," *Lab on a Chip*,

vol. 11, no. 17, pp. 2827-2834, 2011.

[51] Dino Di Carlo, Daniel Irimia, Ronald G. Tompkins, and Mehmet Toner, "Continuous inertial focusing, ordering, and separation of particles in microchannels," *Proceedings of the National Academy of Sciences*, vol. 104, no. 48, pp. 18892-18897, November 2007.

[52] J. Calvin Giddings, "A system based on split-flow lateral-transport thin (SPLITT) separation cells for rapid and continuous particle fractionation," *Separation Science and Technology*, vol. 20, no. 9-10, pp. 749-768, 1985.

[53] Filip Petersson, Lena Aberg, Ann-Margret Sward-Nilsson, and Thomas Laurell, "Free flow acoustophoresis: microfluidic-based mode of particle and cell separation," *Anal. Chem.*, vol. 79, pp. 5117-5123, 2007.

[54] P. Augustsson, C. Magnusson, C. Grenvall, H. Lilja, and T. Laurell, "Extraction of circulating tumor cells from blood using acoustophoresis," in *Proceedings of Micro Total Analysis Systems*, Groningen, 2010, pp. 1592-1594.

[55] Siyang Zheng et al., "Membrane microfilterdevice for selective capture, electrolysis and genomic analysis of human circulating tumor cells," *Journal of Chromatography A*, vol. 1162, no. 2, pp. 154-161, 2007.

[56] Quan Guo, Sarah M McFaul, and Hongshen Ma, "Deterministic microfluidic ratchet based on the deformation of individual cells," *Physical Review E*, vol. 83, p. 051910, 2011.

[57] Swee Jin Tan, Levent Yobas, Gabriel Yew Hoe Lee, Choon Nam Ong, and Chwee Teck Lim, "Microdevice for the isolation and enumeration of cancer cells from blood," *Biomedical Microdevices*, vol. 11, pp. 883-892, April 2009.

[58] Xing Chen, Da Fu Cui, Chang Chun Liu, and Hui Li, "Microfluidic chip for blood cell separation and collection based on crossflow filtration," *Sensors and Actuators B*, vol. 130, pp. 216-221, 2008.

[59] Yu Xiang and David A. LaVan, "Analysis of soft cantilevers as force transducers," *Applied Physics Letters*, vol. 90, no. 13, p. 133901, 2007.

[60] Thomas Gerhardt, "Chromatographic cell separation based on size and rigidity using dynamic microstructures," University of British Columbia, Vancouver, Masters Thesis 2010.

[61] Thomas Gerhardt, Sangpil Woo, and Hongshen Ma, "Chromatographic behaviour of single cells in a microchannel with dynamic geometry," *Lab on a Chip*, vol. 11, pp. 231-2737, 2011.

[62] Abhishek Jain and Lance L Munn, "Determinants of leukocyte margination in rectangular microchannels," *PLOS One*, vol. 4, no. 9, p. e7104, 2009.

[63] H. Hoefemann et al., "Bubble-jet actuated cell sorting," in *Miniaturized Systems for Chemistry and Life Sciences*, Seattle, 2011, pp. 2040-2042.

[64] Guofeng Guan et al., "Size-independent deformability cytometry with active feedback control of microfluidic channels," in *Miniaturized Systems for Chemistry and Life Sciences*, Seattle, 2011, pp. 1053-1055.

[65] D. M. Audet and W. L. Olbricht, "The motion of model cells at capillary bifurcations," *Microvascular Research*, vol. 33, pp. 377-396, 1987.

[66] B. Roberts and W. L. Olbricht, "The distribution of freely suspended particles at microfluidic bifurcations," *AIChE*, vol. 52, no. 1, pp. 199-206, January 2006.

[67] Laure Saias, Julien Autebert, Laurent Malaquin, and Jean-Louis Viovy, "Design, modeling and characterization of microfluidic architectures for high flow rate, small footprint microfluidic systems," *Lab on a Chip*, vol. 11, pp. 822-832, January 2011.

[68] Brian W. Roberts and W. L. Olbricht, "The Distribution of Freely Suspended Particles at Microfluidic Bifurcations," *AIChE Journal*, vol. 52, pp. 199-206, September 2005.

[69] Sung Yang, Akif Uendar, and Jeffrey D. Zahn, "A microfluidic device for continuous, real time blood plasma separation," *Lab on a Chip*, vol. 6, pp. 871-880, 2006.

[70] "Design Rules for Microfluidic Soft Lithography at Caltech's Foundry," KNI/Beckman Institute Microfluidic Foundry, Pasadena, 2004.

[71] Sung Yang, Akif Uendar, and Jeffrey D. Zahn, "A microfluidic device for continuous, real time blood plasma separation," *Lab on a Chip*, vol. 6, pp. 871-880, April 2006.

[72] George I. Bell, "Models for the specific adhesion of cells to cells," *Science*, vol. 12, pp. 618-627, May 1978.

[73] Abhishek Jain and Lance L. Munn, "Determinants of Leukocyte Margination in Rectangular Microchannels," *PLoS One*, vol. 4, no. 9, p. e7104, September 2009.

[74] Quan Guo, Sunyoung Park, and Hongshen Ma, "Microfluidic micropipette aspiration for measuring the deformability of single cells," *Lab on a Chip*, vol. 12, no. 15, pp. 2687-2695, 2012.

[75] J. C. Loetters, W. Olthuis, P. H. Veltink, and P. Bergveld, "The mechanical properties of the rubber elaqstic polymer polydimethylsiloxane for sensor applications," *J. Micromech. Microeng.*, vol. 7, pp. 145-147, 1997.

[76] Vincent Studer et al., "Scaling properties of a low-actuation pressure microfluidic

valve," *Journal of Applied Physics,* vol. 95, no. 1, pp. 393-398, January 2004.

[77] Todd M. Squires and Stephen R. Quake, "Microfluidics: Fluid physics at the nanoliter scale," *Reviews of Modern Physics,* vol. 77, pp. 977-1026, July 2005.

[78] Vivienne N Luk, Gary CH Mo, and Aaron R Wheeler, "Pluronic additives: a solution to sticky problems in digital microfludics," *Langmuir*, vol. 24, no. 12, pp. 6382-6389, 2008.

[79] Niels Asger Mortensen, Fridolin Okkels, and Henrik Bruus, "Reexamination of hagen-poiseuille flow: shape dependence of the hydraulic resistance in microchannels," *Physical Review E,* vol. 71, p. 057301, 2005.

[80] Brian Kirby, *Micro- and Nanoscale fluid mechanics*, 1st ed. New York, USA: Cambridge University Press, 2010.

[81] E M Purcell, "Life at Low Reynolds Number," *American Journal of Physics*, vol. 45, pp. 3-11, 1977.

[82] Yonghao Zhang, Robert W. Barber, and David R. Emerson, "Particle separation in microfluidic devices: SPLITT fractionation and microfluidics," *Current analytical chemistry,* vol. 1, no. 3, pp. 345-354, 2005.

[83] C D Han and B Barnett, "Measurement of the rheological properties of biological fluids," in *Rheology of Biological Systems*, L G Henry and L Mitchel, Eds. USA: Charles C. Thomas Publishers, 1973, pp. 195-217.

[84] A Ott, M Magnasco, A Simon, and A Libchaber, "Measurement of the persistence length of polymerized actin using fluorescence microscopy," *Physical Review E,* vol. 48, no. 3, pp. 1642-1647, September 1993.

[85] C T Lim, E H Zhou, and S T Quek, "Mechanical models for living cells - a review," *Journal of Biomechanics*, vol. 39, no. 2, pp. 195-216, 2006.

[86] Robert M Hochmuth, "Micropipette aspiration of living cells," *Journal of Biomechanics*, vol. 33, no. 1, pp. 15-22, 2000.

Appendix A: Introduction to Microfluidics

Navier-Stokes, Stokes flow, and the Reynolds Number

The Navier-Stokes equations are a set of partial differential equations used to model the motion of fluids. They take the following form for flow the flow of an incompressible Newtonian fluid in the absence of body forces.

$$\rho\left(\frac{\partial \boldsymbol{u}}{\partial t} + \boldsymbol{u}\cdot\nabla\boldsymbol{u}\right) = -\nabla p + \mu\nabla^2\boldsymbol{u} \tag{A.1}$$

$$\nabla\cdot\boldsymbol{u} = \boldsymbol{0} \tag{A.2}$$

Where ρ is the fluid density

u is the vector velocity of the fluid

p is the scalar pressure of the fluid

μ is the viscosity of the fluid

t is time

Equation 1.1 describes the conservation of momentum, while Equation 1.2 describes the continuity of flow. Non-dimensionalizing the momentum equation reveals an interesting scaling from which the peculiarities of microfluidics spawn. Replacing the dimensional variables **u**, p and x with dimensionless equivalents yields the following.

$$\boldsymbol{u}^* \equiv \frac{\boldsymbol{u}}{U}, \boldsymbol{x}^* \equiv \frac{\boldsymbol{x}}{L}, t^* \equiv t\frac{U}{L}, p^* \equiv \frac{Lp}{\mu U} \tag{A.3}$$

Where U is an appropriate velocity scale

x is a position vector

L is an appropriate length scale

Substituting these variables into the Navier-Stokes momentum equation yields the non-dimensional momentum equation.

$$\frac{\rho UL}{\mu}\left(\frac{\partial \boldsymbol{u}^*}{\partial t^*} + \boldsymbol{u}^*\cdot\nabla\boldsymbol{u}^*\right) = -\nabla p^* + \nabla^2\boldsymbol{u}^* \tag{A.4}$$

The dimensionless prefactor appearing on the left hand side of the equation, $\frac{\rho UL}{\mu}$, is commonly referred to as the Reynolds number: Re. An intuitive understanding of the Reynolds number can be developed by expressing it as the ratio of two competing elements. For example the Reynolds number can be expressed as the ratio of timescales for diffusion of momentum and advection of momentum as below.

$$Re = \frac{\rho UL}{\mu} = \frac{L^2\rho}{\mu} \Big/ \frac{L}{U} = \frac{t_d}{t_a} \tag{A.5}$$

Where t_d is a timescale for the diffusion of momentum

t_a is a timescale for the advection of momentum

Alternatively the Reynolds number can be expressed as the ratio of inertial stresses to viscous stresses as below.

$$Re = \frac{\rho UL}{\mu} = \rho U^2 \Big/ \frac{\mu U}{L} = \frac{\tau_i}{\tau_v} \tag{A.6}$$

Where τ_i is a scale for inertial stress

τ_v is a scale for viscous stress

The relative magnitude of terms on the left hand and right side of the momentum balance equation are determined by the magnitude of the Reynolds number, since all the dimensionless variables in the equation are of order unity. When the Re >> 1 the right hand terms can be neglected and the flow is said to be inviscid. When the Re << 1 the left hand terms can be neglected and the flow is said to be creeping.

Microfluidic devices are almost always low Reynolds number systems. Typical length scales for microfluidic channels are 10-100 μm, typical velocity scales are 10-1000 μm/s, and water has $\rho = 10^3$ kg/m^3, $\mu = 10^{-3}$ Pa·s. This produces Reynolds numbers from 10^{-4} to 10^{-2}, sufficiently small to justify ignoring the left hand side terms in Equation 1.1. In this limit the Navier-Stokes equations collapse into a form known as the Stokes momentum and continuity equations, shown below.

$$\nabla p = \mu \nabla^2 \boldsymbol{u}, \qquad \nabla \cdot \boldsymbol{u} = 0 \tag{A.7}$$

Most microfluidic devices operate using pressure driven unidirectional Stokes flows through static channels. These flows are collectively referred to as Hagen-Poiseuille flows. A Hagen-Poiseuille flow in the z direction through a cylindrical channel of radius R has an exact analytical solution:

$$u_z = \frac{1}{4\mu}\frac{\partial p}{\partial z}(R^2 - r^2) \tag{A.8}$$

Ignoring entrance and exit effects, the total flux Q through a channel of length L is given by integrating u_z across the pipe cross-section:

$$Q = \frac{\pi R^4}{8\mu}\frac{\Delta P}{L} \tag{A.9}$$

This interesting result shows that the flow rate through a microfluidic pipe is proportional to the pressure drop along its length. The constant of proportionality, referred to as the hydraulic resistance, depends on the channel geometry and the fluid viscosity: $R_h \equiv \frac{\pi R^4}{8\mu L}$. This result is derived for a cylindrical tube, but the proportionality of pressure drop and flow rate holds for unidirectional flows through channels with arbitrary cross-section [**79**]. For Hagen-Poiseuille flow through rectangular channels, ubiquitous in microfluidic devices, there exists no closed form solution. A simple first order approximation for the resistance of a rectangular channel with height *h* < width *w* is given below.

$$R_h = \frac{12\mu L}{h^3 w} \tag{A.10}$$

This coarse approximation can be improved with the addition of another term.

$$R_h = \frac{12\mu L}{h^3 w\left(1 - 0.63\frac{h}{w}\right)} \tag{A.11}$$

The first approximation has a worst case inaccuracy of 60% (for a square microchannel), and the second approximation has a worst case inaccuracy of less than 15% (Figure A-1).

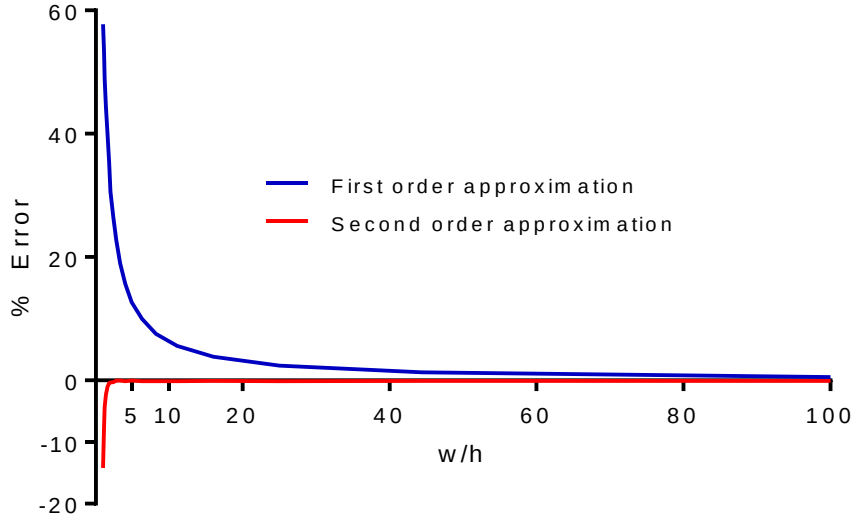

Figure A-1 Accuracy of hydraulic resistance approximations for rectangular channels. First and second order approximations are compared to the exact series solution for varying channel aspect ratios. [**80**].

An active field of study is dedicated to fluid physics at the nanoliter scale [**77**], studying phenomena beyond simple unidirectional flow in pipes. While interesting behaviors abound there are four properties of Stokes flow worth mentioning in particular as they will play a role in the development of the cell separation device.

1. *Kinematic reversibility:* If some solution **u** satisfies the Stokes equations with boundary conditions $\mathbf{u}=\mathbf{u}_b$, then the flow **-u** also satisfies the Stokes equations with boundary conditions $\mathbf{u}=-\mathbf{u}_b$ and a reversed pressure gradient.
2. *Instantaneousness:* As we can see in Equation 1.7, time is not a variable in the Stokes equations. In the absence of a driving force there can be no motion - a creature swimming at 30 μm/s with $Re=3*10^{-5}$ would come to a stop within 0.1 Angstrom and 0.3 microseconds if it attempted to glide [**81**].
3. *Superposition:* If $\mathbf{u_1}$, p_1 and $\mathbf{u_2}$, p_2 are solutions of the Stokes equations, then any linear combination $\lambda\mathbf{u_1} + \delta\mathbf{u_2}$, $\lambda p_1 + \delta p_2$ is also a solution. This is true of all linear systems.

Microfluidics and electrical circuits

The flow rate through microfluidic channels is linearly proportional to the drop in pressure across the channel length, as shown in the previous section.

$$\Delta p = Q \cdot R_h \tag{A.12}$$

This linear proportionality, in combination with the required conservation of volume of incompressible flows, allows us to analyze flows through microfluidic networks using standard methods of linear electrical circuit analysis. Indeed, microfluidics and circuits are analogous systems: both Ohm's Law and Equation 1.12 describe a linear proportionality between a flow rate and a scalar potential, and the flowing objects in both systems are conserved. These similarities, summarized in Table A-1, are all that are required to justify analyzing microfluidic circuits as one analyzes electrical circuits.

Table A-1 Analogous entities in microfluidic and electrical circuits.

Microfluidics	**Electrical Circuits**
Pressure	Voltage
Volumetric flow rate	Current
Hydrodynamic resistance	Resistance
$\Delta p = Q \cdot R_h$	$\Delta V = I \cdot R$
Conservation of volume	Conservation of electrons (Kirchhoff's First Law)
Pressure as a state function	Voltage as a state function (Kirchhoff's Second Law)
Channels in series $R_{eq} = \sum_{i=1}^{N} R_h$	Resistors in series $R_{eq} = \sum_{i=1}^{N} R$
Channels in parallel $\frac{1}{R_{eq}} = \sum_{i=1}^{N} \frac{1}{R_h}$	Resistors in parallel $\frac{1}{R_{eq}} = \sum_{i=1}^{N} \frac{1}{R}$

We can combine analyze the hydraulic resistance of microfluidic networks using the same series and parallel addition laws of electrical circuits, expecting a reasonable approximation provided the channels are sufficiently long compared to the junction areas to satisfy unidirectionality. We can therefore estimate flow rates within the device using knowledge of the resistance of various elements and measurements of hydrostatic pressure at the nodes between them.

Suspensions in microfluidic channels

The path of cells suspended in a microfluidic flow may differ from that of the fluid. Specifically, for non-zero Reynolds number flows, suspended particles will not necessarily respond instantaneously to changes in the flow, meaning that the particles may stray from the path of the fluid. A measure of the fidelity with which a suspended particle will follow a flow is given by a dimensionless number called the Stokes number Stk: the characteristic response time of the particle divided by the characteristic response time of the fluid.

$$Stk = \frac{\tau U_o}{L} \tag{A.13}$$

Where τ is the characteristic relaxation time of the particle due to drag

U_o is the characteristic velocity of the fluid flow

L is the characteristic length of the fluid flow

For a particle of diameter D and density ρ in a Stokes flow, the characteristic relaxation time is [**82**]:

$$\tau = \frac{\rho D^2}{18\mu} \tag{A.14}$$

This expression gives a Stokes number of:

$$Stk = \frac{\rho D^2 U_o}{18\mu L} \tag{A.15}$$

When the Stokes number is very small (<<1), the particle reacts almost instantaneously to any changes in the flow, and follows the path of the fluid. Such a particle is called a Lagrangian flow tracer. When the Stokes number is larger, one cannot assume that a particles trajectory will be the same as the fluid flow. For a microfluidic cell separation device, we might consider a cell of 15 μm diameter, neutrally buoyant (ρ=1000 kg/m^3) flowing through a 50 μm tall channel in water (μ= 10^{-3} Pa·s) at a rate of 100 μm/s. Such a cell would have a particle Stokes number of $2.5 \cdot 10^{-5}$ and, barring collisions with channel walls, its trajectory could be reasonably approximated by the fluid streamline that passes through the center of the cell.

It is worth briefly noting that flowing suspensions of high concentration typically lead to non-Newtonian effects. For example cells in whole blood occupy approximately 45% of the

total fluid volume and blood is a shear thinning fluid [**83**]. The suspensions used in this work do not approach the concentrations needed to produce non-Newtonian behavior so the relevant theory will not be discussed.

Finite size effects

Unlike the ideal fluidic elements used to derive the Navier-Stokes equations, solid particles suspended in a flow have finite size. The finite size of suspended particles can influence the flow around them, and may cause particles to follow different streamlines than an ideal fluid element would have. The particles trajectory can be influenced in one of two ways: through changes in the flow field induced by the presence of the particle, or through physical interactions between the particles and other solid structures. The presence of the particle can alter the flow as its surface represents another boundary condition that did not previously exist - these effects always exist but are most influential when the size of the particle is comparable to the relevant dimension so the flow geometry [**80**]. A single cell will do little to alter the flow in a pipe of 1m diameter but it may drastically change the flow in a capillary. Particles will also traverse streamlines in the case of physical collisions with other solid objects. A suspended particle cannot follow a streamline that would force it collide with another particle or a channel wall. If the flow brings a solid particle into contact with another solid, the particle will be bumped into an adjacent streamline. This phenomenon is exploited in the literature and in this work to achieve various effects and will be explained in greater detail in 1.5.2.1.

Settling

If the density of the suspended particles and surrounding fluid is unequal, gravity will cause the suspended particles to settle or float. As particles settle they experience a Stokes drag force, opposite to the direction of their motion and proportional to their speed [**81**]. The steady state speed of settling is determined by the balance of these competing forces. At steady state, a spherical particle settling under gravity is described by the following force balance:

$$F_d = F_g \tag{A.16}$$

$$6\pi UD\mu = \frac{1}{6}\pi D^3(\rho_p - \rho_w)g \tag{A.17}$$

$$U = \frac{D^2(\rho_p - \rho_w)g}{36\mu} \tag{A.18}$$

Where U is the steady state speed of settling

D is the particle diameter

g is acceleration due to gravity

ρ_w, ρ_p are the densities of water and the particle, respectively

The speed of particulate settling is seen to increase with particle size, density, and magnitude of acceleration, and is inversely proportional to the viscosity of the suspending fluid.

It may often be desirable to maintain an even concentration of suspended particles over a long time span, requiring countermeasures to prevent settling. The effects of settling can be combated either through adjusting the density of the fluid to match that of the suspended particles or by continuously resuspending the medium. Density matching in particle suspensions can be achieved by mixing Ficoll, a high-density non-reactive polymer into the fluid at a known concentration. Continual resuspension can be achieved via pipetting or stirring.

Non-rigid particles in flows

Cells are non-rigid bodies that can be deformed by external forces. Deformability is biologically critical for blood cells, ensuring that they can pass though small diameter capillaries in the circulatory system. The spherical shape and deformability of most cells in suspension is provided by tension in the cortical actin layer. Actin filaments have elasticity on the length scale of the cell, with persistence length of approximately 15 μm [**84**]. Surprisingly the plasma membrane plays only a small role in cell deformations, as it is too rigid to deform (lysis typically occurs after 4% deformation) but has sufficient extra surface area from wrinkles and folds to allow the cell to change shape. Mechanical models for the deformation of single cells are based on this notion of deformability originating from the cortical layer [**85**]. We will not employ these models in analyzing our cell separation mechanism, largely due to the high geometric complexity of the mechanism. For the purposes of this thesis, it is sufficient to observe that different cell phenotypes have different

deformabilities, and that these deformabilities can be quantified by measuring their cortical tension.

Appendix B: Fabrication

B.1 Photolithographic fabrication of device masters

Master molds for the microfluidic devices were fabricated on campus, using the photolithography apparatus in the AMPEL Nanofabrication Facility. In this class 1000 cleanroom facility, we used high resolution photomasks (CAD/Art Services, Bandon, Oregon) to produce patterns in photoresist on a silicon substrate. The photolithographic process allows the formation of 3D structures by the sequential deposition of 2D layers. The flow layer master wafer is composed of four layers. The first three layers are made of SU-8 negative photoresist (Microchem, Newton, Massachusetts), a resist used to form features of rectangular cross-section. The final layer is made of SPR positive photoresist (DOW Canada, Calgary, Alberta), a resist used to form the rounded features required to make microfluidic valves. The standard fabrication procedures for negative and positive photolithography differ, and are described individually below.

<u>Negative photoresist</u>

1. In the cleanroom facility, the wafer is first cleaned by rinsing with acetone, methanol, and then isopropanol.
2. The wafer is dried with a nitrogen gun, and then baked at 200^{o}C for 5 minutes to dehydrate the wafer surface for improved photoresist adhesion.
3. A layer of liquid photoresist is deposited on the wafer surface on a spinner. The spin speed and resist type is determined by the desired thickness of the layer, using manufacturer recommendations and trial and error.
4. The wafer is then baked at 95^{o}C for 2-5 minutes, depending on the thickness of the spun photoresist.
5. The wafer is loaded into an aligning apparatus (Canon PLA-501F, Mississauga, Ontario) that contains the photomask to be imaged. The wafer may be moved to align the photomask with features on the wafer from previous depositions, if necessary.
6. The wafer is then exposed to UV light through the photomask for 30-90 seconds, activating a crosslinking reaction within the exposed photoresist.
7. The wafer is ejected from the mask aligner and baked at 65^{o}C, 95^{o}C, and 65^{o}C for 1, 5, and 1 minute(s) respectively.

8. The wafer was then developed in SU-8 developer (Microchem), washing away any non-crosslinked resist.
9. Finally, the wafer was cleaned in isopropanol and dried with nitrogen.

Positive photoresist

1. Clean the wafer with acetone, methanol, and then isopropanol
2. Dry with nitrogen.
3. Spin a thin layer of HMDS (Sigma-Aldrich) onto the wafer at 4000 rpm for 40 seconds, and then allow it to evaporate.
4. Spin SPR onto the wafer at a speed determined by the desired layer thickness
5. Remove the edge bead of photoresist manually
6. Bake at 65^{o}C, 95^{o}C, 65^{o}C, for 1, 3, and 1 minute(s) respectively
7. Leave to sit at room temperature overnight
8. Load into mask aligner, align, and expose for four 30 second bursts, with a 30 second interval between each burst
9. Leave to sit at room temperature overnight
10. Develop the wafer in MF 24A photoresist developer (DOW)
11. Rinse with DI water, then dry with nitrogen
12. Bake the wafer at 65^{o}C, 95^{o}C, 65^{o}C, for 1, 3, and 1 minute(s) respectively, reflowing the photoresist and rounding the features

Table B-1 below shows the exact parameters used to fabricate the SU-8 layers of the control and flow master wafers. Table B-2 shows the fabrication parameters for the SPR layer.

Table B-1 Photolithography fabrication parameters for SU-8 layers

Layer	Dehydration bake time (min)	Dehydration bake temperature (^{o}C)	Photoresist	Spin time (s)	Spin speed (rpm)	Softbake time (min)	Softbake temp (^{o}C)	Exposure time (s)	Post-exposure bake time (min)	Post-exposure bake temp (^{o}C)	Measured thickness (µm)
Flow 1	5	200	SU-8 3010	30	2250	1,5,1	65,95,65	90	1,5,1	65,95,65	13.2
Flow 2	1,5,1	65,95,65	SU-8 3005	30	3000	1,3,1	65,95,65	60	1,3,1	65,95,65	19.6
Flow 3	1,5,1	65,95,65	SU-8 3025	30	4000	1,5,1	65,95,65	90	1,5,1	65,95,65	23.5
Control	5	200	SU-8 3025	30	3000	2,5,2	65,95,65	100	2,7	65,95	19.5

Table B-2 Photolithography fabrication parameters for the SPR layer

Layer	HMDS spin time (s)	HMDS spin speed (rpm)	Photoresist	Spin time (s)	Spin speed (rpm)	Softbake time (min)	Softbake temp (°C)	Wait time (hrs)	Exposure time (s)	Wait time	Reflow bake time (min)	Reflow bake temp (°C)	Measured thickness (µm)
Flow 4	50	200	SPR 220-7	50	625	1,3,1	65,95,65	24	5x 30	24	1,5,1	65,95,65	32

B.2 Multilayer Soft Lithography

Once the master silicon wafers are fabricated, they can be used to produce microfluidic devices outside of a cleanroom environment. Typically, we fabricated polyurethane replicas of the master silicon wafers and cast PDMS microfluidic device out of the polyurethane molds. The benefit of this approach lies in minimizing the handling of master silicon wafers, as they are easy to break and expensive to produce.

Fabrication of polyurethane molds

1. Prepare a 100g 10:1 base to hardener ratio solution of RTV 615 PDMS (Momentive Performance Materials)
2. Place the silicon master wafer on a tinfoil sheet and form the foil into 2 cm high dish around the wafer
3. Pour the mixed PDMS onto the master silicon wafer
4. Place the wafer and PDMS into a desiccator and apply vacuum until air bubbles are brought to the surface of the PDMS
5. Bake for 1 hour at 65°C to cure the PDMS
6. Cut the silicon master wafer away from the cured PDMS and trim the edges of the cured PDMS negative
7. Tape the PDMS negative, feature side up, to a rubber dish
8. Place the rubber dish and PDMS negative into a desiccator and apply vacuum for 10 minutes
9. Prepare 100g of polyurethane (Smooth-Cast ONYX, Fiber-Tek, Burnaby, BC) according to the manufacturer's instructions
10. Pour the polyurethane over the PDMS negative and wait 3 hours to allow the polyurethane to cure

11. Separate the polyurethane mold, PDMS negative, and rubber dish

Fabrication of PDMS devices from polyurethane molds

1. Prepare 50g of RTV 615 at a 5:1 base to hardener ratio
2. Prepare 10g of RTV 615 at a 20:1 base to hardener ratio
3. Pour the 5:1 RTV mixture over the polyurethane replica of the flow layer
4. Desiccate the 5:1 mixture until all the bubbles are pulled to the surface of the PDMS
5. Bake the 5:1 mixture at 65 ^{o}C for 1 hour
6. Spin the 20:1 mixture over a control layer wafer or replica at 1350 rpm for 60 seconds
7. Bake the 20:1 mixture at 65 ^{0}C for 1 hour
8. Remove the cured RTV flow layer from the polyurethane replica
9. Trim the cured flow layer and punch the necessary holes using a 0.5 mm punch (Technical Innovations)
10. Clean the featured side of the flow layer and the top side of the cured control layer with Scotch tape ®
11. Manually align the flow layer over the control layer and gently bring them into contact
12. Bake the combined device overnight at 65^{o}C, forming a diffusion bond between the control layer and flow layer PDMS
13. Delicately peel the bonded PDMS device away from the control layer mold
14. Trim the bonded devices edges
15. Punch the necessary holes to the control layer with a 0.5 mm punch
16. Clean a 75x50x1 mm glass slide and the underside of the bonded PDMS device with Scotch tape ®
17. Place the slide and PDMS device in the plasma cleaner (Harrick Plasma, Ithica, NY) feature side up
18. Plasma clean the slide and device for 60 seconds
19. Delicately place the device on the glass slide, feature side down, to form a plasma bond between the control layer and slide
20. Bake at 65^{o}C for 1 hour

Appendix C: Image Processing

The following macro code was used as the image processing pipeline for cell counting. The software used was ImageJ 1.45s, available for free at http://imagej.nih.gov/ij. The pipeline employs the grayscale watershed plugin, authored by Daniel Sage, available at bigwww.epfl.ch/sage/soft/watershed/

```
// Cell counting macro
//
// Will Beattie
// July 19th 2012
//
// This macro takes an image from fluorescent microscopy and counts the number of cells //therein
rename("Source");
run("8-bit");
run("Duplicate...", "title=Mask");
setAutoThreshold("Default dark");
//run("Threshold...");
thresh=getNumber("Enter threshold value",15);
setThreshold(thresh,255);
run("Convert to Mask");
run("Erode");
run("Dilate");
run("Invert");
imageCalculator("Subtract create", "Source","Mask");
selectWindow("Result of Source");
run("Gaussian Blur...", "sigma=2");
//run("Enhance Contrast", "saturated=0.35");
selectWindow("Result of Source");
getStatistics(area,mean,min,max);
run("Watershed ", "blurring='0' watershed='1 1 0 "+(max-1)+" 0 1' display='0' ");
waitForUser;
run("Invert");
run("Analyze Particles...", "size=10-800 circularity=0.00-1.00 show=Nothing display clear");
```